Advanced monitoring, fault diagnostics, and maintenance of cryogenic systems

Candidate:

Eng. Mario Girone

University Supervisor:

Prof. Pasquale Arpaia

CERN Supervisor:

Dr. Marco Pezzetti

Department of Engineering,
University of Sannio, Benevento

Alla mia famiglia,
che mi ha sempre sostenuto ed ha sempre creduto in me.

Resume

In this Thesis, advanced methods and techniques of monitoring, fault diagnostics, and predictive maintenance for cryogenic processes and systems are described. In particular, in **Chapter 1**, mainstreams in research on measurement systems for cryogenic processes are reviewed with the aim of defining key current trends and possible future evolutions. Then, in **Chapter 2**, several innovative methods are proposed. A transducer based on a virtual flow meter is presented for monitoring helium distribution and consumption in cryogenic systems for particle accelerators [1]. Furthermore, a comprehensive metrological analysis of the proposed transducer for verifying the metrological performance and pointing out most critical uncertainty sources is described [2]. A model-based method for fault detection and early-stage isolation, able to work with few records of Frequency Response Function (FRF) on an unfaulty compressor, is then proposed [3]. To enrich the proposal, a distributed diagnostic procedure, based on a micro-genetic algorithm for transducer networks monitoring complex physics systems, is shown [4]. Finally, a GEO algorithm for predictive maintenance scheduling problems, already proposed in our Research Group [5] and compared to GA with encouraging but only preliminary results, is extended to complex plants such as large experimental cryogenic systems. In **Chapter 3**, the numerical characterization of the proposed methods is reported. Finally, in **Chapter 4** the experimental validation for the presented techniques is illustrated.

List of publications

Journals

[1] P. Arpaia, P. Cimmino, M. Girone, G. La Commara, D. Maisto, C. Manna, M. Pezzetti (2014) "Decentralized diagnostics based on a distributed micro-genetic algorithm for transducer networks monitoring large experimental systems", *AIP Review of Scientific Instruments*, 85.9: 095103.

[2] P. Arpaia, E. Blanco, M. Girone, V. Inglese, M. Pezzetti, F. Piccinelli, and L. Serio (2015) "Proof-of-principle demonstration of a virtual flow meter-based transducer for gaseous helium monitoring in particle accelerators cryogenics", *AIP Review of Scientific Instruments*, 86.7: 075004.

[3] P. Arpaia, M. Girone, A. Liccardo, M. Pezzetti, and F. Piccinelli (2015) "Metrological analysis of a virtual flowmeter-based transducer for cryogenic helium", *AIP Review of Scientific Instruments*, 86.12: 125001.

[4] P. Arpaia, L. De Vito, M. Girone, M. Pezzetti (2015) "Early-stage fault isolation based on frequency response fitted by small-size samples for cryogenic cold compressors with Active Magnetic Bearings", *AIP Review of Scientific Instruments*, submitted.

Conferences

[1] P. Arpaia, M. Girone, D. Maisto, C. Manna, M. Pezzetti (2014) "A generalized extremal optimization-inspired algorithm for predictive maintenance scheduling with economic dependence on Helium storage systems for particle accelerators", *IMEKO TC-4 2014*, (Benevento).

[2] P. Arpaia, L. De Vito, M. Girone, M. Pezzetti (2015) "Fault detection based on noise power estimation for cryogenic cold compressors with active magnetic bearings", *IMEKO XXI World Congress 2015*, (Prague).

[3] P. Arpaia, M. Girone, A.Liccardo, M. Pezzetti, F. Piccinelli (2015) "Surface response-based performance assessment of a virtual-flowmeter based transducer for helium monitoring", *IMEKO XXI World Congress 2015*, (Prague).

[4] P. Arpaia, M. Girone, M. Hubatka, M. Pezzetti (2015) "Active magnetic bearings system upgrade for LHC cryogenic cold compressor, radiations mitigation project (R2E)", 15^{th} *International Conference on Accelerator and Large Experimental Physics Control Systems (ICALEPCS)*, (Melbourne).

Acknowledgments

The work presented in this Thesis was carried out at CERN in the framework of a collaboration with the University of Sannio (Benevento) and the control and elecrical support section of the CERN cryogenic group.

I would like to thank all the people who, in different ways, contributed to the success of this research. In particular I thank my university supervisor, Prof. Pasquale Arpaia, for this great opportunity that he gave me and for the continuous motivation to complete my work even in "dark" periods. His guidance and patience were really important for achieving the final result. I want to thank Marco Pezzetti, my CERN supervisor, for his technical guidance and for his suggestions. His passion for presentations gave me the opportunity to enhance my professional and my communication skills.

Heartfelt thanks to Vitaliano Inglese for his guidance and support during my period at CERN even if for him I will always be "il napoletano triste".

A special thanks to Prof. Luigi Glielmo, Antonella Polvere, Massimo Manna, Luca de Vito, Annalisa Liccardo, Jean-Laurent Tavian, Luigi Serio and all the papers co-authors for their collaboration and their guidance. I gratefully acknowledge to the entire TE-CRG-CE section at CERN for their support, for their willingness every single time I had a technical problem. In particular my office colleague Franck Morant for his technical support during the measurements campaign, Fabio Piccinelli for his help during the Virtual flowmeter test campaign and last but not least Andrea Calore for his help.

A special thank to the group of Italian colleagues with whom I shared this experience at CERN: Giancarlo Golluccio, Lucio Fiscarelli, Carlo Petrone and Giuseppe Montenero and in particular I enjoyed the friendship of all the Italians with whom I shared not only the work experience at CERN but also the "wild" nights in Geneva: Domenico Caiazza, Mario Kazazi, Ernesto De Matteis, Giordana Severino, Carlo Baccigalupi, Alessandro Parrella and Donato De Paola. Annalisa deserves a big "grazie"

for her love, for her support and for helping me to overcome the my famous "dark" period at CERN. Without her this experience would not be the same.

Of course I cannot forget all my friends in Italy. Even if there is a big physical distance, they always support me in all the occasions and in particular Peppe and Saba with whom I grew up together and they always were there for me.

Finally, I want to thank my family and in-particular my parents and my sister for their unconditional love.

Contents

Introduction

Temperature affects material properties and industrial processes more than any other variable, such as pressure, magnetic field or electric field [6]. Several studies in this field were conducted, and in particular, since the 19^{th} century, scientists have exploited extremely low temperature to enhance mechanical and physical properties of materials [7]. The science of very low temperature is called *cryogenics*, and even if it is not specifically defined in literature, in general, all temperatures below 120 K are considered cryogenic [8]. The typical cryogens used to reach these low temperatures are: liquid nitrogen, oxygen, helium, methane, ethane, and argon. The treatment at cryogenic temperature of a wide variety of materials, such as metals, alloys, and polymers, aimed at enhancing their structural properties, is defined as a *cryogenic process*. These processes are more and more exploited in several application fields, from scientific research to medicine. As an example, in large scale experimental physics facilities such as the Large Hadron Collider (LHC) at CERN, cryogenics enables the superconducting operation of accelerating or beam-positioning devices [9]. In particular, superconductor's performance is boosted owing to heat transfer properties offered by superfluid helium through a cryogenic cooling system down to 1.9 K.

In all these application fields, a prominent role is played by the measurement systems necessary for qualifying, monitoring or controlling the cryogenic processes. Despite their importance, a comprehensive state of the art of the most common techniques and technologies used in the various cryogenic systems is still missing. In the first part of this Thesis, mainstreams in research on measurement systems for cryogenic processes are reviewed with the aim of defining key current trends and possible future evolutions.

Monitoring systems for cryogenic facilities are more and more important. Even if complex and suitable techniques are used commonly in industrial monitoring, owing to technical and economical reasons, not always sensors can be installed in all

the required measurement points of a plant. To face this problem, virtual sensors are penetrating many research fields in recent years, including nature and building monitoring [10, 11], vehicles [12, 13], people health care [14, 15] and process control [16, 17, 18, 19, 20]. *Virtual sensors* are a subclass of *virtual instruments*, i.e. software programs used in measurement automation for interfacing actual instrumentation. In a virtual sensor, the user interface is minimal or not existing at all [21]. Furthermore, differently from physical sensors, a non easily measurable quantity is assessed indirectly by combining data sensed by a group of heterogeneous sensors.

One of the most challenging and productive application fields of virtual sensors is flow measurement, owing to the complexity and the cost of the physical flow meters, as well as the difficulty of placing them in the plant. This problem in complex systems such as the helium cryogenic system implemented for the LHC at CERN is even more evident. In cryogenic applications, virtual sensors have already been implemented. As an example, a preliminary virtual flow meter application, only for liquid helium, was developed at CERN to estimate the mass flow through some Large Hadron Collider (LHC) cryogenic control valves [22]. Two methods, typically used in cryogenics, proposed by the valve companies Samson AG [23] and Sereg-Schlumberger Inc. [24] were applied [22] for helium liquid phase only. However, for this virtual flow meter, a comprehensive test campaign together with a metrological assessment in both gaseous and liquid state phases of helium is missing. In this Thesis, a transducer based on a virtual flow meter is proposed for monitoring helium distribution and consumption in cryogenic systems for particle accelerators. Furthermore,a comprehensive metrological analysis of the proposed transducer is also proposed by defining an uncertainty behavioral model, as well as a sensitivity analysis based on statistical experiment design and analysis of variance[25],[26]. The characterization aims at verifying the metrological performance and pointing out most critical uncertainty sources.

Nowadays, diagnostic functions (fault detection, fault isolation and fault diagnosis) in sensitive or complex facilities are an outstanding requirement. In particular, embedded early-stage fault isolation, capable to detect and identify multiple faults promptly, becomes more and more important [4]. At CERN, owing to the dimensions of the Large Hadron Collider, an effective refrigeration in the range of kW is achieved through combined cycles, making use of sub-atmospheric cryogenic compressors and heat exchangers included in eight refrigeration units [27]. These 1.9 K refrigeration units showed up as the most sensitive to process instabilities or transient phases. In particular, the cold compressors equipped with active magnetic bearings (AMB) were

detected as their most critical components. In literature, rotating machinery diagnostics is an important and well-documented field of study. Frequency-domain analysis of vibration data, in particular, wavelet transforms [28, 29, 30, 31, 32, 33, 34, 35], and support vector machines [36, 37, 38], are common approaches.

The active magnetic bearings' design allows the measurement of several quantities in time or frequency domain, without additional sensors. Moreover, the contact-free rotor support makes vibrations and sound levels measurements, essentials for the aforementioned techniques, not as important as for the rotating machinery equipped with different bearing technologies. Several techniques for fault detection for systems with active magnetic bearing have been proposed. For example, in Ref. [39], a multi purpose real-time system for early-stage fault isolation and error correction is described, but historical fault data were needed.

Few compressors based on AMB are available, thus testing and running maintenance on such machines is an expensive task, owing to inactivity cost and long preparation times. One of the main issue for their maintenance is the availability of several measurement records to perform a deep characterization of the nominal condition. In this Thesis, a model-based method for fault detection and early-stage isolation, able to work with few records of Frequency Response Function (FRF) on an unfaulty compressor, is proposed.

In monitoring large experimental systems, such as particle accelerators, gravitational wave detectors, optical and radio telescopes, or nuclear fusion facilities, a large number of distributed sensing and processing nodes is employed [40, 41]. An effective real-time system, capable of handling massive data, detecting anomalous deviations from nominal behavior, and diagnosing the corresponding causes promptly, is required. Resource distribution, communications limitations, poor scaling to configuration changes, and possible node/link faults create several design challenges to centralized diagnostic paradigms [42]. Alternative approaches can be classified in decentralized or distributed, according to the corresponding level of information sharing among the processors [43, 44]. In decentralized solutions, significant knowledge about the system to be diagnosed is shared among the processors. In distributed solutions, processors host well-separated processes, by fitting better the requirements of complex systems [40, 41, 42]. In literature, some distributed solutions aim at increasing the computational efficiency, [43, 45, 46] while others are mainly focused on working locally,[43, 44, 47] by involving other subsystems only when additionally information or hardware resources are needed. However, all these approaches introduce ad hoc di-

agnostic architectures, devoted to specific problems. Thus, a generic and application-independent approach, as the Multiple Faults Diagnostic (MFD) problem in Ref. [48], seems to be still missing for a distributed system. MFD has been approached successfully as a combinatorial optimization problem, whose solution is a set of faults best explaining the detected anomalies. Nevertheless, for interconnected large experimental systems, fault identification is a non-polynomial-complexity combinatorial problem. Natureinspired meta-heuristic algorithms (e.g., Genetic Algorithms, Particle Swarm Computation, Ant Colony Optimization, and so on) [49, 50] proved to have capabilities of both overcoming local optima through parallel exploration of the solution space and driving the search towards the most promising solutions. However, their need for powerful computing resources severely restricts their applications in distributed transducers networks. By considering these assumptions, proper metaheuristic algorithms with very-low computational load and satisfying optimization performance are Micro-Genetic Algorithms (MGA), [51] a variant of Genetic Algorithms for small population sizes. They substantially reduce the number of total evaluations for achieving the optimal solution and prevent working memory from overloads. Applications in experimental physics are not rare, especially in nonlinear optics.[52, 53] In particular, in Ref. [52], a MGA allows the optimum frequency, maximizing atomic effect stabilization by high-intensity laser fields, to be found. The fitness is computed by solving a time-dependent Schrodinger equation at different laser field intensities, on parallel processors communicating through Message Passing Interface (MPI), a widely used standard protocol [54]. In this Thesis, a distributed diagnostic procedure based on a micro-genetic algorithm for transducer networks monitoring complex physics systems is proposed. The well-settled evolutionary approach of centralized multiple-faults diagnostics is extended to distributed transducer networks monitoring large experimental systems.

In the framework of large experimental systems [55], e.g. nuclear power plants, or transmission networks, another crucial problem is the predictive maintenance scheduling problem. In such a context, the large number of components, often without simple interconnections, makes the problem analytically intractable. The maintenance optimization in multi-component systems is extensively studied in literature and components' interactions have been classified [56, 57]: structural, stochastic, and economic. Combining two or more models makes them too complicated to be analysed and for this reason, only the economic dependency is to be considered. As previously said, meta-heuristic techniques were extensively used for optimization problems and

in particular the nature-inspired methods: Simulated Annealing (SA) [58], Genetic Algorithms (GA) [59], Particle Swarm Optimization (PSO) [60], and Ant Colony Optimization (ACO) [61]. A different meta-heuristic technique called Generalized Extremal Optimization (GEO) has also been applied for this class of problems. This method was developed by De Sousa and Ramos in 2002 [62] as a variation of the Extremal Optimization (EO) proposed by Boettcher adn Percus in 2001 [63], and since than has been applied to some complex optimization problems: e.g. De Sousa et al. applied GEO for an optimal heat pipe design [64] first, and later to an inverse radiative transfer problem [65]. Recently, in an effective multiprocessor scheduling [66], the above mentioned method was solved by Switalski and Seredynski. In all these works, GEO algorithm demonstrated satisfying results compared to the most popular algorithms.

Other versions of GEO's algorithm were also developed and applied for optimization problems, Guo et al. proposed a modified GEO (MGEO) for a quay crane scheduling problem [67]. The modification was introduced because of the various interference constraints imposed by this kind of problem. Also an hybrid GEO (HGEO) was proposed by D. Xie et al. that combines genetic and GEO algorithm [68]. They first developed a population-based GEO (PGEO) in order to accelerate convergence speed and than they integrated this new solution in HGEO showing better performances than classical GAs on an optimal power consumption for semi-track air-cushion vehicle. In this Thesis, a standard GEO algorithm already proposed for predictive maintenance scheduling problems by the Authors [5] and compared to GA with encouraging preliminary results is extended to complex plants such as large experimental systems.

Therefore in this Thesis, in **Chapter 1**, the current trends and possible future developments of the measurement systems for cryogenic processes are presented. In **Chapter 2**, the proposal for an advanced monitoring, fault diagnostics, and maintenance of cryogenic systems is described. Consequently, in **Chapter 3** the numerical characterization of the proposed methods is showed. Finally in **Chapter 4** the experimental validation for the presented innovative techniques is illustrated.

Chapter 1

Cryogenics monitoring: state of the art

In this chapter, mainstreams in research on measurement systems for cryogenic processes are reviewed with the aim of defining key current trends and possible future evolutions. In particular, in Section 1.1, main advanced measurement systems for cryogenics are classified according to the measurand. Section 1.2 deals with a brief description of systems for liquid level measurements. A review of current flow meter technologies is reported in Section 1.3. Section 1.4 describes research methods used for pressure measurements in processes at cryogenic temperatures. A classification of research temperature measurement systems is reported in Section 1.5. Section 1.6 describes other measurement systems for cryogenics processes. A last section of synthesis discussion about current research trends and possible future evolutions concludes the paper.

1.1 Measurements for cryogenics

Nowadays, cryogenics is exploited in several application fields [69] (see Fig. **??**): (i) chemical reactions, in order to produce active ingredients for popular drugs (medical applications), (ii) cooling systems for chemical reactors, (iii) freezing of foods and biotechnology products (vaccines), (iv) cryogenic fuels, oxygen and hydrogen, used for spacecraft, and (v) several physics experiments, such as gravitational wave detectors and superconducting particle accelerators and colliders. In the industry, cryogenics is used for: (i) freezing food, (ii) pressurization of plastic bottles and aluminum cans containing drinks, (iii) maintenance of pipelines by freezing the liquid on both side of the leak, (iv) ground freezing, to allow tunneling operation in wet unstable soils, (v) heat treatment of metals, (vi) freezing of explosives to make them temporarily harmless, and (vii) cryo-cleaning.

In biological and medical fields, cryogenics is used to enable biological material to be frozen and stored, especially for semen, thin tissues and blood. Furthermore, the use of superconducting magnets allows detecting abnormalities of various tissues of the body, using magnetic resonance imaging techniques. Liquid hydrogen is used together with liquid oxygen as fuel for space vehicles.

All the processes performed in these application fields need for measurements: (i) for monitoring the physical properties of materials during the cryogenic process, or (ii) as feedback in the control systems of that processes. These measurements are performed by systems that work: (i) at cryogenic temperatures, if they are applied directly inside the cryostat, (ii) at environmental temperature, when they measure physical quantities related to the cryogenic process out of the cryostat, or (iii) at both environmental and cryogenic temperatures, when they are used for measurements in a wide range of temperatures, e. g., during the cryostat freezing. In this paper, a review of the research state of the art in these measurement system typologies is reported.

At this aim, these measurements systems have been classified according to the physical quantities to be measured (Fig. 1.1): (i) liquid level measurement systems, (ii) flow meters, (iii) pressure measurement systems, (iv) thermometers, (v) current measurement systems, (vi) mechanical loss measurement systems, and so on.

In the followings sections, a brief review of measurement systems, for each of these quantities, is reported and described.

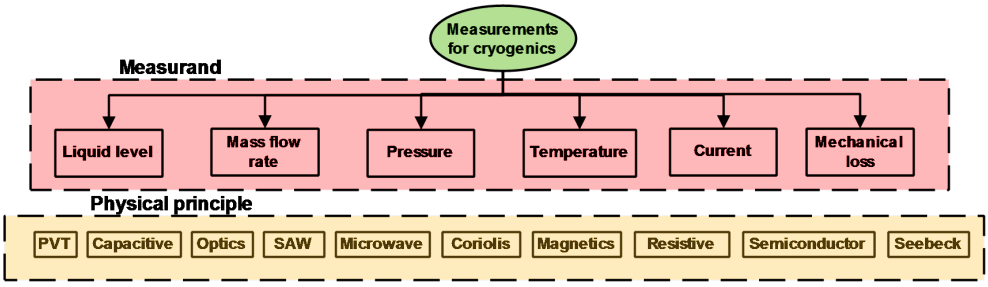

Figure 1.1: Classification of measurements for cryogenics based on measurand.

1.2 Measurement of liquid level at cryogenic temperature

Liquid level measurements are required for cryogenic propellant tanks in space applications. For these applications, several extreme conditions should be analyzed: (i) the extreme cold, which makes many sensors inoperable due to the reduction of the carriers conductivity, (ii) mechanical stress, and (iii) undesirable device heat generation. For these reasons, in scientific literature, several sensor technologies based on different physical principles have been analyzed with the purpose of designing liquid level sensors operating at cryogenic temperature.

In this section, a level sensor classification, based on the different physical principles, is reported: (i) Pressure-Volume-Temperature (PVT) sensors, (ii) capacitive sensors, (iii) optical fibers, and (iv) Surface Acoustic Wave (SAW) sensors.

1.2.1 PVT liquid level sensors

Cryogenic liquid propellant engines are mostly used for modern rocket propulsion systems [70]. In this case, an accurate prediction of the fuel that will be used for the flight is very difficult [70]. For this reason, level measurements of the remaining propellant in the tank are necessary. During the rocket launch there is a time period where the tank containing the fuel is under low gravity condition. In this case, it is difficult to measure the level of the remaining cryogenic liquid in the tank. One of the most important method used in this environmental condition is the Pressure-Volume-Temperature (PVT) method. In this case temperature sensors, pressure sensor and the flow-meter should operate at cryogenic temperatures. In Ref. [70], the authors investigate the use of PVT method for liquid level measurements of a helium tank at

cryogenic temperatures. The PVT is an indirect method. It is possible to measure the cryogenic liquid level measuring the temperature and pressure of both a supply bottle and a propellant tank, in order to evaluate the amount of propellant remaining in the tank (see Fig. 1.2).

The authors have analyzed the system in a 1.8 m diameter and 3.0 m high vacuum chamber. The test tank is 0.5 m in diameter and 0.9 m in overall length and is suspended from the vacuum chamber lid. For the tests, the helium was supplied at approximately constant pressure and ambient temperature from the supply bottle. Fluid temperatures are measured by a vertical array of 10 silicon diode sensors with a reported accuracy of 0.25 K. A second group of silicon diode sensors was placed in three clusters separated by 0.64 cm vertical spacing at nominal fill level location of 20 %, 50 % and 80 % fill. This second group of sensors detects the presence of liquid of vapor at the given level. These liquid level point sensors had very repeatable and reliable behavior, but the switch point of each sensor had to be individually determined and was found to vary with temperature. These sensors have been used as reference system of the PVT measurements.

Other temperature sensors have been placed on the top, side and bottom of the tank to monitor tank wall heating and cooling during helium inflow and pump operation. Two pressure gauges are placed into the vent line for measuring tank pressure. One gauge is limited to 0.7 MPa, the second one has a full scale of 2.1 MPa and their accuracy are 0.11 % and 0.073 % of full scale, respectively. Helium flow rates have been measured by two thermal flow meters. The authors have performed two tests. The first one consists in reducing the fill level from 80 % to 50 %, the second one from 50 % to 20 %. The authors provide measurement uncertainty values of the PVT method of 1 % at 20 % of liquid level, 1.5 % at 50 % and 2 % at 80 %.

Another analysis of PVT method for liquid volume estimation is presented in Ref. [71]. The authors obtained an accuracy of 4.6 % for high liquid-fill [72, 80] % and of 3.4 % for low fill levels [27, 30] %.

1.2.2 Capacitive sensors for liquid level measurements

In Ref. [72], the authors propose a level meter based on capacitive transducer for cryogenic liquids. The measurement principle of the level meter operation is based on phase-locked loop (PLL) technique.

The physical principle of level measurements using capacitive transducers is based on the difference in the value of the dielectric constant for gas and liquid state [73, 74]. The capacitive transducer is usually designed in the form of two coaxial tubes isolated

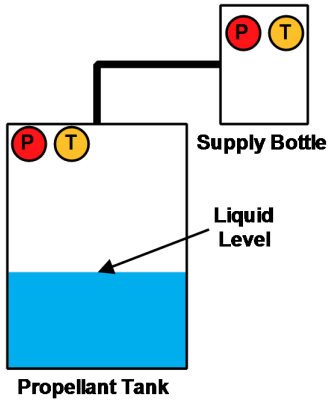

Figure 1.2: General architecture of a PVT measurement system [70].

from each other. The capacity of such transducer is given by the following equation:

$$C = \frac{2\pi\epsilon_0\epsilon_r}{ln(\frac{D}{d})}H \tag{1.1}$$

where ϵ_0 is the dielectric constant of vacuum, ϵ_r is the dielectric constant of the material between the electrodes, D and d are diameters of outer and inner electrodes, respectively, and H is the height of the transducer.

If the transducer is filled up to height hs by the cryogenic liquid, the capacity variation is given by:

$$\Delta C = \frac{2\pi\epsilon_0(\epsilon_{rl} - \epsilon_{rg})}{ln(\frac{D}{d})}h \tag{1.2}$$

where ϵ_{rl} and ϵ_{rg} are the dielectric constants of the liquid and gas, respectively. The accuracy and precision of level measurements depend on the transducers and the used electronics for capacitive measurements [75].

Due to the low temperatures, the displacement of the liquid surface generates low changes in the capacitance value. Thus, the large stray capacitance combined with the capacitance of the lead wires can cover the transducer variations. For this reason, normally a third tube, which surrounds the other and forming a three terminal capacitor, is used to remove the lead wires capacitance effects [75].

In order to increase the transducer sensitivity, the radii of the concentric plates must decrease (1.2). In Ref. [73], another solution to increase the transducer sensitivity is presented. In this work, multi-parallel plates consisting of eight capacitor plates separated with polyacetal spacers is proposed.

Several methods and techniques can be used for capacity measurement, such as ac bridges, pulse methods, etc. The PLL method for capacity measurement has been explored in Ref. [72]. The standard scheme of a PLL-detector consists of a phase comparator, a low-pass filter and a Voltage-Controlled Oscillator (VCO). In the locked condition, the frequency of VCO follows the frequency changes of the input signal because feedback loop hold zero–phase difference between the frequency of VCO and the input signal frequency. In this way, the VCO voltage is proportional to the frequency change of the input signal.

In order to measure the capacitance, the authors have modified the PLL scheme. A waveform generator issues a sinusoidal wave at a reference frequency on the input of PLL. Furthermore, the capacitive transducer is connected to the VCO circuit. The VCO frequency depends on both the controlled voltage and the capacity of the transducer. In order to hold zero–phase difference between the reference frequency and VCO frequency, the VCO changes linearly with the capacity value. The authors have evaluated that the sensitivity of the proposed level meter is 171 mV/pF and that the stability of the output voltage is 1 mV.

1.2.3 Distributed liquid level sensors using optical fibers

In Ref. [76], the authors designed a liquid level sensing system for cryogenic fluids with millimeter spatial resolution. This liquid level measurement system is based on fiber optic.

Fiber optic based sensors offer several advantages over electrical sensors because they are: (i) immune to electromagnetic interference, (ii) spark-free, (iii) and chemically inert. Furthermore, a large number of sensors can be placed on a single fiber. So, it is possible to reduce the cost and implementation efforts for distributed sensing.

Liquid level sensors can be classified into two categories: (i) discrete level sensors, and (ii) continuous level sensors. Discrete level sensors detect the liquid level at a single location and provide binary information related to whatever the liquid is present at that level. Several discrete level sensors can be placed along an optical fiber. The spatial density of sensors on the fiber limits the level resolution [77]. On the other hand, continuous level sensors provide level measurements in the sensing range.

Continuous fiber level sensors are based mainly on the theoretical discrimination between refractive index (RI) of liquid and gas states. Due to the RI contrast between liquid and gas, the optical proprieties of sensing light , such as transmission loss, Bragg wavelength, and spectral interference, change. The continuous fiber level sensors are able to provide sub-millimeter spatial resolution with very fast response time. The

sensing distance is fundamentally limited by the evanescent field ([100, 200] mm). The other limitation is that for cryogenic fluids, such as liquid hydrogen and liquid helium, the RI values are very close to their gaseous forms. This makes the RI discrimination impossible.

In Ref. [76], the authors propose a continuous liquid level sensor based on self-heated fibers as sensing devices (see Fig. 1.3). It is based on Optical Frequency Domain Reflectometry (OFDR) measurement of in-fiber Rayleigh scattering. The OFDR measurement system consists of a coherent tunable light source, a fiber interferometer, and a photo-detector. Light from the laser is linearly swept and coupled into the fiber interferometer. The fiber interferometer splits the light into measurement and reference arms. The measurement arm of the interferometer is connected to the heated fiber placed in the tank using a fiber recirculator. The probe light is reflected back to the OFDR system through the fiber recirculator and combined with the reference arm light onto the photo detectors. The time delay between reference arm path and measurement arm is proportional to the liquid level.

The authors have tested the measurement system for temperature lower than 4 K and for cryogenic liquids. The system exhibits a sensing range up to 70 m with a sub millimeter spatial sensing resolution.

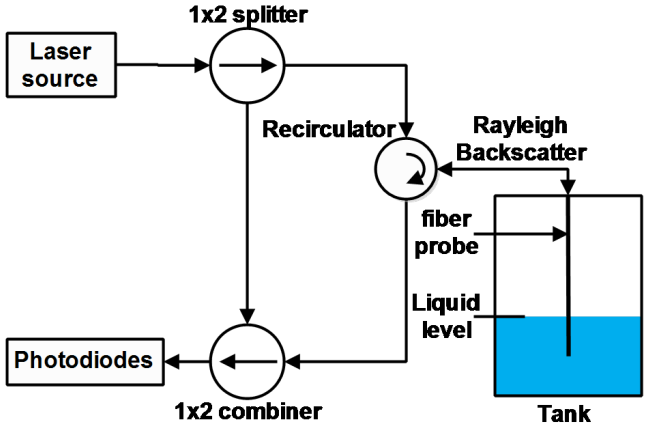

Figure 1.3: General architecture of a in-Rayleigh scattering method based on optical frequency domain reflectometry [76].

1.2.4 SAW liquid level sensors

Acoustic devices can successfully operate at extremely low temperatures, without performance degradation. In Ref. [78], the authors analyze the use of surface acoustic wave (SAW) devices to cryogenic liquid level sensing. The SAW device works as switch; when a liquid is immersed in the tank, the wave energy is damped by the liquid. The tested SAW devices are commercial SAW lithium niobate and quartz filters with the lids removed. The authors have tested the SAW device at cryogenic temperatures and demonstrate how this sensor can operate under those thermal circumstances for both quartz and lithium niobate materials.

1.3 Flow meters for cryogenic systems

The study of fluid in cryogenic systems is an important issue in several applications because it allows to know how the fluid is distributed in the cryostat, and if the flow is laminar or turbulent. For example, slush hydrogen is a cryogenic fluid consisting of solid hydrogen particles in liquid hydrogen. This liquid is used in several applications, such as fuel for reusable space shuttles, coolant for cold neutron generation and transport and storage of hydrogen as a clean energy source. As a matter of fact, the accuracy of flow measurements affects directly the failure detection of these industrial systems. In case of cryogenic turbo-machinery, an abrupt change in fluid quality can lead to over-speed, causing catastrophic failure.

For this reason, flow measurements are a standard task for any application involving fluid. Several methods have been explored for the measurement of fluid flow in pipes: differential pressure, vortex, ultrasonic, Coriolis and thermal flow measurements. In this section, the followings methods are reported: (i) capacitive, (ii) microwave, (iii) thermal, (iv) Coriolis,, (v) optical based and (vi) virtual flow-meters.

1.3.1 Capacitive flow meters

In Ref. [79], the authors present a capacitive mass flow rate measurement system based on density measurements applied to slush hydrogen. For density measurements, several techniques can be used: (i) measurement of the attenuation of beta or gamma ray, (ii) measurement of the propagation speed of ultrasonic waves, (iii) measurement of phase shift of microwaves, and (iv) capacitive measurements.

The beta/gamma ray method cannot be used in presence of radioactive substances, while the ultrasonic wave method is affected by solid particles in fluid. On the other

hand, capacitive densimeters allow high-precision density measurements.

The structure of capacitive densimeter consists of a double cylinder or parallel plates. By considering the variation of dielectric constant according to the slush hydrogen state (liquid or solid), it is possible to measure the hydrogen density. The substance under test can easily leak into the gap between the capacitor electrodes. By expanding the area of electrodes and reducing the distance between them, it is possible to improve the measurement accuracy. Considering the specific properties of slush hydrogen, the authors have adopted a cylinder structure with a flat plate. This structure reaches high accuracy values and solves the problem of entry of solid particles between the electrodes. For the capacitive densimeter, the measurement accuracy is of about 0.5 %. The authors have implemented a mass flow rate measurement system using two of these capacitive densimeter placed at two locations along the piped flow. The flow velocity is evaluated from the densimeter distance and the delay time when the cross correlation function of the two density signals has the maximum. For the capacitance flowmeter, the difference between the flow velocities measured by the flowmeter and that calculated from the liquid-level change in the tank is of about 10 %.

In Ref. [80], the authors propose a capacitive-based measurement approach, which consists of eleven ring-shaped electrodes mounted on the outer surface of a pipe, for measuring the flow velocity and the mean density of liquid hydrogen flows. A disadvantage of these capacitive based flow meters is the time-dependent drift of the dielectric constant.

1.3.2 Microwave flowmeters

In Ref. [79], the authors presented a microwave mass flow rate measurement system based on density measurements applied to slush hydrogen. Microwave densimeter exploits the phase shift of a microwave due to variation of the dielectric constant of a fluid. The measurement system consists of microwave transmitter and receiver and a network analyzer. The dielectric constant of the slush hydrogen changes with the average density of fluid. By using the network analyzer, it is possible to evaluate the phase shift between the transmitted and the received microwaves and so the fluid density. As described above, the flow velocity is evaluated through cross-correlation method. The authors provide an error of about 5 % obtained with the microwave flowmeter.

1.3.3 Thermal flow measurement

Thermal flow measurement systems are based on two electrically heated elements placed consecutively along the flow direction. An element generally consists of a platinum wire, to which an electrical current is applied for heating and where the voltage drop is evaluated for temperature measurement. If both the elements are heated with the same electrical current and the fluid stands still, then the temperature difference between the elements should be zero. In case of fluid flow, the temperature profile is shifted in flow direction and the mass flow rate can be measured being proportional to the temperature difference (see Fig. 1.4).

In such thermal systems, the correlation between temperature difference and the mass flow rate depends on several parameters: distance between elements, tube size, materials and shape of heat exchangers.

A large number of calibration procedures that aim to minimize the error effects have been developed. Otherwise, in case of cryogenic applications, no flow meter can be found as serial product on the market, mainly because a manufacturer calibration at low-temperature helium or hydrogen are unfeasible in terms of cost and effort. In Ref. [81], the authors propose a method for flow measurement with the ability for intrinsic calibration that can be executed during operation of a cryogenic installation. The intrinsic calibration is based on the evaluation of two independent analytic expressions for the flow rate from the same measurement readings (input parameters). If the input parameters are error-free, the two expressions provide identical results. This can be formalized with a goal function in a minimization routine that compensates these systematic errors. The calibration procedure needs that the flow is stationary for some seconds during calibration. Furthermore, after the calibration, the authors have obtained a measurement uncertainty of 1 %.

Another analysis of thermal flow measurement system is presented in Ref. [82]. In this paper, the authors analyze the physical characteristic of a hot film probe at cryogenic temperature. The transducer consists of a 10 µm × 10 µm hot film probe used in a 6 cm helium gas wind tunnel. A ring of bronze with two stainless steel wires supports the sensor. Furthermore, two wires are placed and electrically isolated from the bronze ring. A 10 µm quartz fiber is epoxied across the wires and the sensor is located at the center of the fiber. The device is made by depositing a thin film Au-Ge on the central portion of the fiber. The material shows a nearly power law dependence of resistivity on temperature over a wide range. Furthermore, the cryogenic hot film probe has a fast response time.

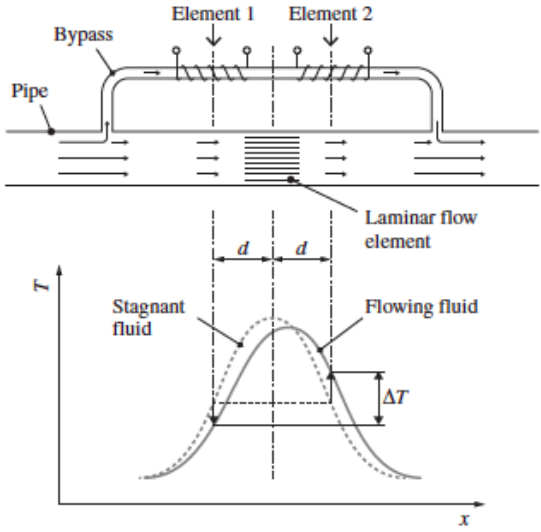

Figure 1.4: General measurement principle overview of thermal flow meter [81].

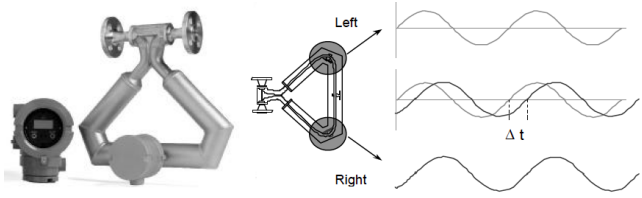

Figure 1.5: Architecture of a Coriolis flow meter [83].

1.3.4 Mass flow meters based on the Coriolis acceleration

Cryogenic systems are used for accelerator and fusion superconducting devices (cavities, magnets, power lines and current leads). For these systems, it is important to monitor accurately thermal performance and the distribution of cooling power. Coriolis mass flow meters have been successfully used to measure flow of fluid and gases at ambient temperatures with a good accuracy and long-term reproducibility.

The advantages of Coriolis meters are: (i) they do not suffer from time-dependent drift (capacitance flow meter), (ii) they are manufactured of stainless steel, and (iii) they respond directly to mass flow, eliminating the need for density compensation.

Coriolis meter consists of: an in-line sensing element and two electromagnetic transducers. The sensing element consists of a collector (manifold) that splits the

flow into two parallel tubes. The tubes are vibrated at a resonant frequency. The fluid momentum coupled with the oscillatory motion, created by the vibration, induces a Coriolis force along the length of the tubes. Two electromagnetic transducers are located on opposite legs of the flow tubes; the vibration of the tubes generates sinusoidal signals that are shifted in phase due to the Coriolis force. By measuring the phase shift, it is possible to calculate the mass flow rate.

For temperature below ambient, the Young modulus increases and so does the stiffness of the tube. For this reason, a Pt 100 (RTD) is placed on the tubes for compensating the temperature effects.

In Ref. [83], the authors have tested a Coriolis meter at cryogenic temperature (see Fig. 1.5). As described above, a typical Coriolis meter needs to temperature measurements, for compensating the vibration characteristics of the sensing element. Those vibrations are related to the changing of the elasticity modulus, which is well characterized at different temperatures. The elasticity modulus is constant with a value of 207.5 GPa below 20 K; so the authors have evaluated the correction factor with respect to the ambient temperature of 20 °C.

The authors have tested the Coriolis flowmeter and found that it achieves a measurement accuracy of 0.5 % in liquid, superfluid and supercritical helium, between 1.7 K and 20 K.

1.3.5 Optical techniques for mass flow rate measurements

A cryogenic flow sensor (CFS) for determining mass flow of cryogenic fluids has been developed in Ref. [84]. The proposed CFS exploits optical properties of the fluid under test with two techniques, optical absorption/scatter and acoustic-optic signal processing, for determining quality of the fluid and the mass flow rate (see Fig. 1.6).

In order to quantify the quality of the fluid, the CFS measures the light attenuation due to a change in reflectance in a liquid flow environment and the absorption coefficient. A laser diode generates a Plane-Of-Light (POL) in the propellant plumbing where the fluid crosses. The POL intensity is continuously monitored, thus a changing of light transmittance due to non-uniformity of the flow can be detected. The light source is capable of generating light at different wavelengths; furthermore, the light is uniformly distributed in the propellant plumbing through optical equipment. The sensing part consists of two photo-detectors, one for measuring light attenuation and one for measuring the reflected light. The authors have tested the system with different known particulates in the flow under test (e.g. vapor bubble).

For measuring the mass flow rate, the authors developed a system based on

acousto-optic principles. The system consists of an acoustic transducer for inducing a pressure along the flow direction to change the refractive index grating. The apparent frequency of the acoustic wave changes according to the flow rate. This change is detected using a collimated laser beam and position sensitive detector to measure the degree of Bragg diffraction from the grating. In particular, the angular position of the laser beam passing trough the grating will diffract the laser beam into an angular position, which is linearly proportional to the acoustic frequency.

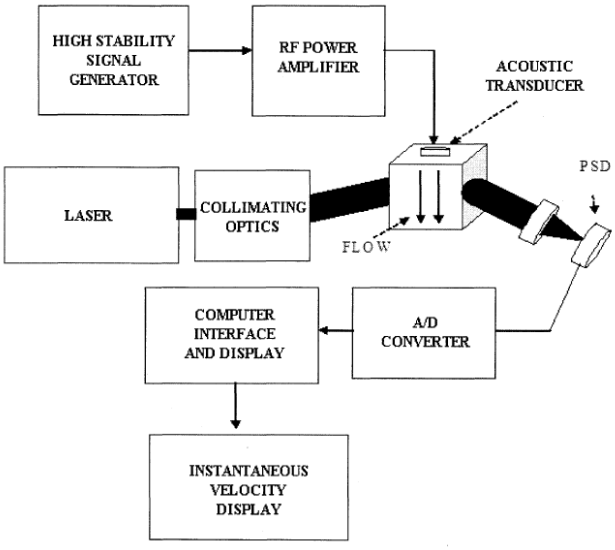

Figure 1.6: The acoustic-optic flow measurement system proposed in Ref. [84].

1.3.6 Virtual flowmeters

A virtual sensor consists of a model that allows the indirect measurement of a quantity by combining data sensed by a group of heterogeneous sensors [1]. These sensors are used for large-scale physics experiments, such as a particle accelerator, to monitor and to control cryogenics superconducting operations. In Ref. [1], the authors present a helium virtual flow meter based on the measurements of the pressure and the temperature at the input and the output of the LHC cryogenic control valve. The authors have analyzed two different models, Samson and Sereg-Schlumberger, for virtual helium flow meter implementation. For both the models the RMSE values have been estimated: 7.50 % for Samson and 7.00 % for Sereg-Schlumberger.

1.4 Pressure sensors for cryogenic systems

Another important parameter to monitor in cryogenic applications is the pressure of the fluid in a tank. In this section, the following methods for pressure measurements are reported: (i) capacitive differential pressure sensors, and (ii) inductive gauge pressure sensors.

1.4.1 Capacitive differential pressure sensors

A capacitive differential pressure sensor based on the measurement of deflection on a membrane is presented in Ref. [82]. The small deflection of membrane changes the distance between two electrodes of a capacitor, as depicted in Fig. 1.7. The capacitance is measured through an ac capacitance bridge. The minimum resolution of the proposed sensor is around $2 \times 10^{-6}\,\mathrm{pF/Hz^{1/2}}$, which corresponds to $0.02\,\mathrm{Pa/Hz^{1/2}}$ and depends on the frequency used for the generator in the ac bridge. Furthermore, the sensor operates over a broad range of temperatures with changing of less than 10 % from 300 K to 4.2 K. The largest measurement effect is the temperature dependence of the elastic modulus, E. Since E depends nearly linearly on temperature, the calibration in terms of temperature has been done at room temperature and 4 K. Another transducer lack is due to the extreme sensitivity of the device. Even microscopic strains can cover pressure variations. For this reason, the capacitor is made almost entirely out of a single material, copper beryllium, to minimize thermal stresses. Another problem is the capacitance dielectric constant drift. To overcome this limit, as a further improvement, the authors propose a device based on two capacitors in intimate contact. The former capacitor senses the differential pressure, while the latter

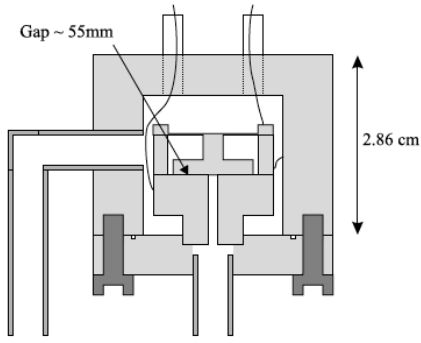

Figure 1.7: Architecture of the proposed pressure sensor [82].

one does not. The second capacitor will be used as a reference capacitor in one leg of the ac bridge. In this case, if the dielectric constant drifts, it would drift identically in both capacitors so that the ratio of the capacities would not be affected by drift. Another high precision capacitance for low pressure gauge at cryogenic temperature is presented in Ref. [85]. The authors have tested the measurement system in the temperature range of [77, 370] K for the pressure range of [0, 50] bar. The measurement system has an accuracy of 1 %.

1.4.2 Inductive gauge pressure sensor

In Ref. [86], the authors have developed a high resolution superconducting pressure gauge and controller system to stabilize pressure within 1×10^{-8} bar in the range of [0, 30] bar at temperatures below 6 K. The transducer is based on inductive sensing of the position of a diaphragm using superconducting techniques [87]. A rod attached to the center of diaphragm supports a superconducting plate, which is in close proximity to a spiral-superconducting coil. The coil is supplied by a 1 A current and coupled to a dc magnetometer. A magnetometer measures the magnetic field changing due to pressure variations. The authors achieve an uncertainty value of 1×10^{-8} in a pressure range of [1, 25] bar. The lack of this system is the low immunity to external magnetic fields.

1.5 Temperature measurements for cryogenics

Cryogenic temperature measurements are needed in several applications: (i) deep-space exploration, (ii) particle physics accelerators, (iii) material characterization, (iv) laser cooling and trapping, (v) medical systems, and (vi) superconductors system. Thermometry at low temperature is a hard task due to low thermal conductance and low thermal capacity of materials. For this reasons, over the years, several researches have been focused to design cryogenic temperature measurement systems. In this section, a brief survey of temperature measurement systems for cryogenics is reported and all the methods are classified on the basis of the physical principle as follows: (i) metallic resistance thermometers and thermocouples, (ii) optic thermometers, (iii) semiconductor thermometers, and (iv) magnetic thermometers. In Tab. 1.1, a comparison of these temperature sensors based on measurement range, measurement features, electric and magnetic field immunity and response time, is reported.

Table 1.1: Comparison of temperature sensors for cryogenic applications.

Technology	Name	Range	Features	Immunity	Response time
RTD	Pt 100	>20 K	Sensitivity: 3.9 Ω/K; Uncertainty: 0.061 K at 30 K	Low	Long
	Pt 500	>20 K	Uncertainty: 0.087 K at 30 K	Low	Long
	CrN	>1 K	Resolution: 1 mK	High	Long
	Ge-on-GaAs	TTR-D: [0.003, 300] K		High	Long
		TTR-G: [0.3, 300] K			
		TTR-M: [4.2, 400] K			
Thermocouple	Type-T	[73, 205] K	Tolerance: 1.5 %	Low	Fast
	Type-E	[73, 105] K	1 %		
Optic	Bragg grating	[8, 40] K	Sensitivity: 1.4×10^{-4} nm/K at 40 K	High	Medium
	Zn-coated	[0.002, 40] K	6×10^{-3} nm/K at 40 K		[2, 3] s
	Copper	[6, 40] K	4.5×10^{-3} nm/K at 40 K		1 s
Semiconductor		[1.8, 300] K		High	[3, 5] ms
Magnetic	Fe/Cr	[0.1, 300] K	Accuracy: 0.1 % at 2 K	Low	Long

1.5.1 Metallic resistance thermometer and thermocouple

Superconductors achieve their unique properties at very low temperatures, less than 20 K. For these applications, temperature measurements must be fast both to control the operations and to detect emergency situations.

Temperature measurements in cryogenic conditions can be made by contact method, i.e. the sensor is directly connected to the Device Under Test (DUT). In this case the main uncertainty sources are due to: (i) the temperature distribution around the point of contact of the sensors with the DUT, (ii) the thermal resistance of the connection between the sensor and the DUT, and (iii) the feedthrough that causes a heat leak to the cooled space.

Resistive temperature detector (RTD), thermocouples and semiconductor diodes are the most common cryogenic sensors used in the temperature range of [1, 100] K. Resistive sensors with a positive temperature coefficient (PTC) are made of pure metals (such as platinum and copper) or pure metals with small impurities (platinum-cobalt). Negative temperature coefficient (NTC) sensors are made of germanium, carbon glass, zirconium oxynitride, etc. Platinum sensors are the most commonly used RTDs due to high measurement accuracy for a wide temperature range of [15, 725] K.

Unfortunately, these sensors are large and show a long response time. For this reasons, they are made with thin film resistors deposited on a ceramic or glass for cryogenics applications. In this way, they show a lower stability, a smaller temperature range, a significant hysteresis, a fast response time and a lower immunity to external magnetic and electric fields.

In Ref. [88], the authors analyze the use of Pt 1000 for measurements at cryogenic temperature. Thin film platinum resistance consists of depositing the resistance structure on a ceramic substrate. The authors have tested 21 samples of Pt 1000 sensors for several temperature ranges. The sensitivity is constant and equal to 3.9 Ω/K until 60 K. Below 60 K it decreases quickly. Furthermore, it is possible to discriminate temperature variation until 20 K. The authors have provided a 6-th order polynomial, which fits the results between the reference temperature values and the measured values.

The measurement uncertainty at 30 K is of 0.061 K and at 78 K is of 0.018 K. The authors have evaluated the sensors stability performing several calibration procedures. The sensors stability is within the range of measurement uncertainty of the calibration cryostat. As last test, the authors have evaluated the effect of magnetic field on the temperature measurements. From this test, they have carried out a 3-rd order curve to compensate magnetic field effects.

Another temperature measurement system based on RTD is proposed in Ref. [89]. The measurement system consists of a Pt 500 RTD. The authors have obtained a measurement uncertainty of 0.087 K at 30 K, and compensated the effect of magnetic field with in-situ calibration procedures. From the reported works, the main problem of RTD sensors is the magnetic and electric field immunity.

CrN (Chromium nitride) has received considerable interest due to its high potential for applications in hard, wear and corrosion resistant coatings and for its small magnetoresistance. In Ref. [90], the authors investigate the use of CrN thin film for temperature sensors in cryogenic applications. The sensor exhibits a negative temperature coefficient resistance below 300 K, a resolution of 1 mK, a good thermal stability and the sensor is insensitive to the magnetic field. The temperature shift due to magnetoresistance in a magnetic field of 9 T is less than 5 mK at 4 K and 2 K. For this reason, the authors demonstrate that CrN can be an excellent material for cryogenic temperature sensors under high magnitude magnetic field conditions.

Furthermore, for space applications, another parameter to take into account is the effect of radiation of several particles. In Ref. [91], the authors developed a single and dual element resistance thermometer based on Ge-on-GaAs films. Ge-onGaAs film resistance thermometers are based on the deposition of a Ge film onto a semi-isolating GaAs substrate. By controlling the Ge film growth, it is possible to produce thermometers having different sensitivity characteristics over the cryogenic temperature range. In Fig. 1.8, it is possible to see the resistance vs. temperature characteristics for the following Ge-on-GaAs thermometer models: TTR-D [0.03, 300] K; TTR-G [0.3, 300] K and TTR-M [4.2, 400] K. The authors have investigated the effect of neutrons, gamma-rays, electrons and bremsstrahlung photons on Ge films. The results show a high radiation tolerance up to integral doses of 1 MGy.

Another temperature sensor that can work at cryogenic temperature is the thermocouple. The most important advantages of thermocouples are: small dimensions of the junction, small heat capacity, short response time, repeatable temperature characteristics and negligible self-heating effect. Unfortunately, thermocouples require the use of complicated conditioning circuits. Thermocouples of type E (chromel-constantan), type T (copper-constantan) and type K (chromel-alumel) are the most popular in cryogenic applications.

In Ref. [92], the authors present the results obtained from dynamic tests of the most popular sensors used at low temperatures, Pt 100 and thermocouples E and T. The reference object used for dynamic test is a heat exchanger in the form of a copper disk cooled by a helium cryocooler ARS DE-210AF. The temperature controller

Lakeshore 331 controls the temperature of the heat exchanger. For the thermocouples, the authors have obtained good dynamic properties and good accuracy. On the other hand, the thin layer Pt 100 exhibits a low repeatability of characteristics below 100 K, which excludes its use in cryogenic systems.

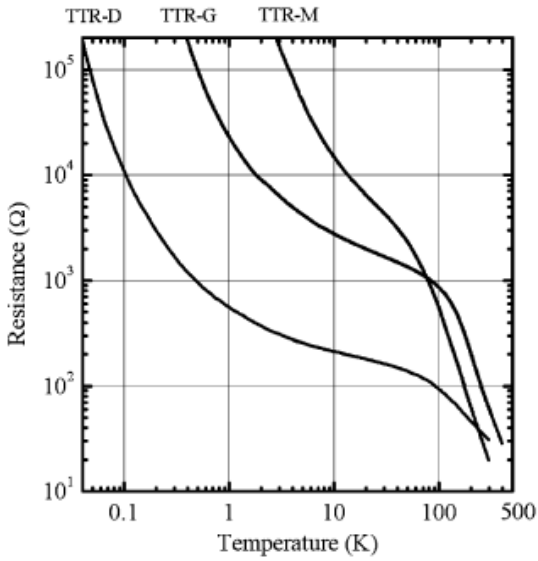

Figure 1.8: Resistance vs temperature curves for different models of Ge-film thermometer [91].

1.5.2 Optic thermometers

Thermal sensors based on fiber optics have the following advantages: (i) fast response time, (ii) high accuracy, and (iii) high electric and magnetic field immunity. On the other hand, the use of these sensors at cryogenic temperature less than 77 K is very hard because, at these temperatures, the fiber thermal expansion coefficient decreases.

In Ref. [93], the authors investigate the use of fiber optic thermal sensors in the very low temperature region of [4.2, 30] K. The thermal sensor consists of a fiber optic with hot-imprinted Bragg grating. By illuminating the fiber with a broadband light source, a wave at the Bragg wavelength is reflected by the imprinting grating. The wavelength value depends on the environmental temperature. Furthermore, by imprinting along the fiber several grating at different positions, a quasi-distributed temperature measurement system can be realized [94]. In Ref. [93], three different

sensors have been tested: (i) bare sensor, which consists of an uncoated fiber with imprinted a Bragg grating, (ii) zinc-coated sensor, and (iii) copper electroplated sensor. In the temperature range of [6, 270] K, the coated sensors exhibit higher sensitivity values than the bar one. The Zn-coated sensor shows the highest sensitivity along the whole temperature range. On the other hand, the copper electroplated sensor shows an acceptable sensitivity and repeatability in the [6, 20] K temperature range. The response time for both coated sensors is larger than the bar one. Another measurement characterization of a fiber-grating sensor is proposed in Ref. [95]. The authors have evaluated the temperature sensitive coefficient, the strain sensitive coefficient and the cross-sensitivity coefficient of the sensor. Furthermore, a three-order polynomial has been evaluated to convert wavelength shift in temperature.

Another optics technique is proposed in Ref.[96]. The authors have designed an optical fiber sensor based on the temperature-dependent emission characteristics of erbium-doped fiber pumped by a 1480 nm laser diode with an amplitude modulation of the driver current. The authors have obtained a measurement resolution of 0.4 K at room temperature and of 0.07 K for liquid nitrogen temperature.

As described until now, it is possible to say that optical sensors are immune to electromagnetic interference. Nevertheless, all fiber-optical sensors are wired devices requiring special interface packaging for the cryogenic zone. In Ref. [97], the authors propose a hybrid design optical sensor. This sensor consists of a 6H-SiC chip placed in a cryogenic vacuum temperature chamber with a glass window for optical laser beam access. A circular polarization light is targeted on the SiC chip. The light reflected by the chip is measured by a photodetector. By measuring the optical power with the photodetector, it was possible to measure the cryostat temperature.

1.5.3 Semiconductor thermometers

Semiconductor thermometers can be classified in: p-n junction devices and semiconductor resistance thermometers. In the former case, the p-n junction forward voltage drop is proportional to the environmental temperature; in the latter case, the thermometer consists of a resistor made of semiconductor material. For these sensors, the unique disadvantage is the low immunity to magnetic and electric field, as described in Ref. [98].

P-n junction devices

One of promising on-chip thermometer for cryogenic applications is a superconductor-insulator-normal (SIN) metal junction thermometer. Current-voltage characteristic of the junction is non-linear near the gap voltage. High temperature sensitivity for SIN thermometer can be reached with a LC resonance circuit with a high frequency and low noise amplifier. However, the system sensitivity is limited by the signal to noise ratio of the amplifier. For this reason, in Ref. [99], the authors propose a temperature measurement system based on a series of SIN thermometers. In this way, it is possible to increase the system sensitivity and overcome the noise due to the external amplifier.

Semiconductor resistance thermometers

Space is a hard environment for any electronic component. The components must operate at extreme low temperature, in vacuum and high radiation doses. Furthermore, the components should resist to mechanical shock, vibration, and acceleration during launch. Depending on criticality, failure of a single component can cause failure of a portion of mission or of the entire mission. For these reasons, any component must meet rigorous screening before to be chosen for space applications. In Ref. [100], the author proposes a standard for aerospace screening and qualification test for Cernox resistance thermometer. The two most common types of cryogenic thermometers used in space applications are based on resistance or on the p-n junction voltage drop of a diode. Diode temperature sensors have low radiation immunity and a fixed response time. On the other hands, the material composition of resistance thermometers can be manipulated to create a family of response curves for a given application temperature range. Cernox resistance thermometers are into this category. These devices are made via reactive sputtering to create a conducting zirconium nitride material embedded in a non-conducting zirconium oxide matrix. By regulating the nitrogen-to-oxygen gas composition, it is possible to change the temperature measurement range and the sensitivity of the sensor.

Another application of semiconductor resistance thermometer is proposed in Ref. [101]. The next generation of LHC (Large Hadron Collider) superconducting magnets must operate in hard conditions: high radiation doses ($[10,\ 50]$ MGy), high voltage environment ($[1,\ 5]$ kV) during the quench, dynamic high magnetic field up to 12 T, dynamic temperature range ($[1.8,\ 300]$ K in 0.6 s). For this system, it is important to study dynamic thermal effects with high sampling rate above 200 Hz, such as the heat flux through the magnet structure and the hot spot in conductors during a magnet quench. In Ref. [101], the authors propose a high-voltage thin film thermal anchor

for a carbon ceramic sensor, in order to measure the temperature directly on the superconductor cable under the conditions described previously. The temperature measurement system exhibits a time response within the interval of [3, 5] ms at 4.5 K.

1.5.4 Magnetic thermometers

Layered magnetic metallic structure can be used as temperature sensors. The giant magnetoresistance (GMR) increases with the decrease of the temperature. In Ref. [102], the authors propose a Fe/Cr magnetoresistive sensor that exploits the increasing of GMR effect at low temperature. The temperature dependence of the sensor resistivity has been measured in a temperature range of [0.1, 300] K and the authors found that the resistivity becomes constant at temperature below 2 K with an accuracy better than 0.1 %.

1.6 Other measurements

The topologies of measurement performed at cryogenic conditions are continuously growing in different application fields. In this section, a collection of new measurements for cryogenic processes is reported: (i) optical absorption measurements, (ii) viscosity measurements, (iii) hydrogen concentration measurements, (iv) displacement measurements, (v) current measurements, and (vi) mechanical loss measurements.

1.6.1 Optical absorption measurements

Two experimental techniques can be used to measure the optical absorption of a material at cryogenics temperatures: (i) the photo thermal deflection technique, and (ii) the calorimetric measurement.

The first one is based on the mirage effect. The system consists of two lasers: (i) a high power laser, called pump laser, and (ii) a low power laser. The pump laser is focused on the material and so its light is partially absorbed by the sample. The absorbed optical power creates a gradient of temperature on the sample. The probe beam is aligned to intersect the pump beam in the sample and is deflected by the gradient of the refractive index, which changes with the temperature gradient. The deviation of the beam is detected by a quadrant photodetector and it is directly proportional to the amount of power absorbed in the sample. In Ref. [103], the authors measure the optical absorption of doped crystalline silicone, which is a candidate material for the low temperature interferometer of the Einstein Telescope. The authors

observe, using the photo thermal deflection technique, a nearly constant absorption from room temperature down to cryogenic temperatures for two silicon samples both crystals doped with boron.

On the other hand, calorimetric measurements are based on a laser beam passed through a sample and measuring the increase in temperature directly with a temperature sensor.

1.6.2 Viscosity measurements

In Ref. [104], a pressurized gravitational capillary (PGC) viscometer has been developed for sub-cooled liquified gases, such as oxygen, nitrogen, hydrogen and methane. The proposed system provides absolute viscosity measurements with uncertainty of 1 %, necessary for the demands of aerospace engineering. The PGC viscometer cell consists of two reservoirs having the same height. A coiled capillary of electroformed nickel hydraulically connects the two reservoirs. Using helium gas to drive liquid from a third supply reservoir, a level difference is created between the first two reservoirs. Helium gas is then used to pressurize the first two reservoirs equally. Each reservoir holds a capacitive liquid-level sensor that measure the flow induced by gravity through the capillary. The viscosity of the liquid is determined by the relationship of the pressure gradient with the flow rate of the liquid, this relationship parameterized by the geometry of the capillary cross-section.

1.6.3 Hydrogen concentration measurements

In Ref. [105], the authors propose a silica optical fiber sensors coated by different sensitive material to perform gaseous hydrogen detection at cryogenic temperature. The proposed optical sensor is based on the deposition of properly chosen sensitive materials (carbon nanotubes) as nanoscale films on the end of a silica optical fiber. The sensor physical principle is based on the dependence of the reflectance on the optical and geometric properties of the sensitive material. A certain analyte (in that work hydrogen) induces a consequent change in the fiber reflectance. So the concentration of hydrogen can be measured through reflectance measurements.

1.6.4 Displacement measurements

Displacement sensors are employed in superconducting dipoles to steer particles. For correct collimation, the beam must be placed inside the magnetic field with sub-millimeter accuracy. Thus the shrinkage and the expansion of the magnets during

their operations and positioning or aligning of them play important roles in several experiments, such as KATRIN (KArlsruhe TRItium Neutrino experiment) and LHC. Another application for displacement sensor is in the inlet valve of torus cryogenic pump, where the opening and closing of the valve is controlled by the displacement of the valve shaft. Mechanical displacement sensors cannot be used for this kind of applications, because of moving parts failure due to low temperature. On the other hand, electrical and magnetic displacement sensors are quite useful for cryogenic measurements, but they cannot be used in environment with high intensity electrical and magnetic fields. In order to overcome the described lack, the authors in Ref. [106] propose an optical-based displacement measurement system to measure displacement. The authors designed a fiber Bragg grating (FBG) based displacement sensor. This sensor consists of two gratings with two different spatial periods. The former grating is attached to one end of the spring that causes the strain of the sensor due to the displacement of the spring. The latter grating is not affected by strain and measure the temperature during measurement. The grating periods of the two gratings change according to the strain and to the temperature, respectively. The temperature measurements are used to compensate the temperature effects on strain measurement of the first grating. In this way, the temperature-compensated strain data are correlated to displacement. The authors have tested the proposed sensor at temperature around 77 K and the sensor has shown a long-range displacement of 550 mm with an accuracy of 0.142 mm.

1.6.5 Current measurements

Dc current transformers are used in several application fields, such as monitoring of power grid, intensity measurements of particle beam in physics accelerator, control system for power supply, and so on. All these applications operate at room temperature. The increasing interest to the use of superconductors needs the development of dc current transformer for cryogenic temperatures. In Ref. [107], the authors propose a sensor to measure current of a superconducting dc current transformer working for a nominal current of 20 kA at 4.2 K. The sensor shows a precision of 0.05 % with a nonlinearity of 0.05 %.

1.6.6 Mechanical loss measurements

For several experiments, it is important to measure the mechanical loss of materials at cryogenic temperature. For example, in the cryogenic interferometer Kamioka

Gravitational Wave Detector (KAGRA), it is an important issue to characterize the thermal noise of material of fibers used to suspend the interferometer mirrors. This fiber should have low thermal noise, which is proportional to temperature and mechanical loss. For this reason, mechanical loss measurement for several materials at cryogenic temperature is an important issue. In Ref. [108], the authors propose an automated measurement system to measure mechanical loss of a tungsten wire at cryogenic temperature. The measurement is based on a ring-down technique. An electro-static plate excites the resonant vibration of the wire. A laser beam is directed on the wire and the wire vibrations are measured with a photodiode. By measuring the ring-down time and the resonant frequencies, the authors evaluate the mechanical loss.

Chapter 2

Proposal

In this chapter, the proposed solutions for the monitoring, fault detection and early stage isolation, fault diagnosis and predictive maintenance of several cryogenic systems, are presented. In particular, for the monitoring system, in section 2.1.1, the basic idea and two alternative models for helium virtual flow meters are illustrated. Consequently, the alternative helium flow-meters and the operation and uncertainty models are described in sections 2.1.2 and 2.1.3, respectively. Then, the fault detection system, is described: In section 2.2.1, after outlining the proposal concepts, the model definition and identification (2.2.2), as well as the noise power estimation (2.2.3), are described together with the proposed fault detection and diagnostics (2.2.4). The multiple fault diagnosis is formalized in 2.3.1, while in section 2.3.2, the distributed micro-genetic algorithm for multiple-fault diagnostics is presented. Finally, the predictive maintenance problem 2.4.1 is then introduced, by illustrating in section 2.4.2 the proposed predictive maintenance solution.

2.1 ADVANCED MONITORING: Helium virtual flow-meter

2.1.1 Basic Idea

From a conceptual point of view, the transducer (defined as physical sensing elements and other processing units) measures the mass flow $\dot{m}$ indirectly, by processing suitably the physical measurements of the pressure and the temperature at the input and the output of the valve. In particular, a-priori knowledge about the valve and the actual helium behaviours is combined with a-posteriori modelling (*virtual flow-meter*), in order to assess the mass flow through the valve. In Fig. 2.1, the transducer with the corresponding three models (actual helium, valve, and virtual flow-meter) integrated in its structure are highlighted. In particular, at the inlet and outlet of a cryogenic valve, the helium pressure and temperature ($P_{in}, P_{out}, T_{in}, T_{out}$) are measured by means of appropriate transducers (PT and TT, correspondingly).

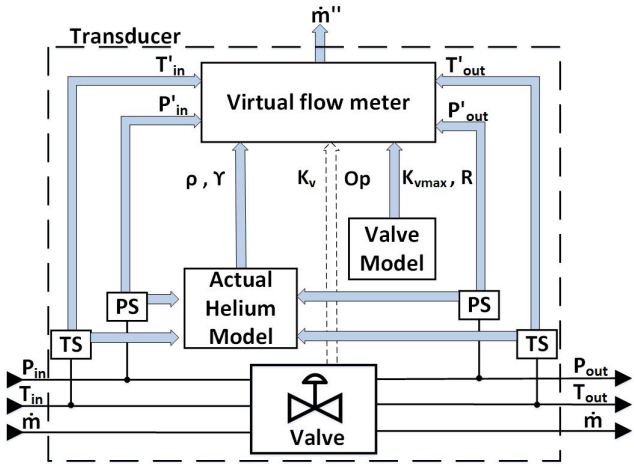

Figure 2.1: Architecture of the virtual flow meter-based transducer (pressure -PT- and temperature -TT- transducers)

The knowledge of the helium thermo-physical properties, namely density ρ and heat capacity ratio γ, is also required at the valve inlet. Particular attention must be paid to the parameter γ, defined as the ratio between the heat capacity at constant pressure, c_p, and the heat capacity at constant volume, c_v. In literature, when the helium is in gaseous phase and far away from the critical point, γ is generally approx-

imated to a constant value (1.66) [109, 110]. However, in cryogenic applications, the helium temperature and pressure conditions vary widely, and for this reason, the heat capacity at constant pressure and the heat capacity at constant volume are calculated at both the inlet and the outlet of the valve, by obtaining γ as:

$$\gamma = \frac{c_{p,average}}{c_{v,average}} \tag{2.1}$$

where:
$c_{p,average} = \frac{c_{p_{in}} + c_{p_{out}}}{2}$ and $c_{v,average} = \frac{c_{v_{in}} + c_{v_{out}}}{2}$.

Some additional phenomena affecting the flow in a valve, such as the stream constriction, have to be taken into account. The parameters mainly influencing the mass flow through a valve are: the pressure drop over the valve, the density, and of course the valve opening. In particular, the valve relative opening l ($0 \leq l \leq 1$) refers to the valve plug position with respect to its closed state. The relationships between the valve opening and the flow rate for the most common valves are illustrated in Fig. 2.2 [111].

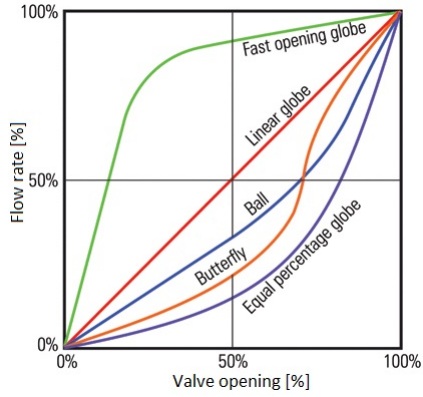

Figure 2.2: Characteristics opening vs flow rate for most common valve types

The flow through the valve is expressed according to the reverse valves sizing problem, described in the international standard IEC 60534-2-1 [112] (flow behaviors mostly laminar or transitional):

- For the liquid phase:

$$Q = N_1 F_R K_v(l) \sqrt{\frac{\rho_w}{\rho} \Delta P} \tag{2.2}$$

- For the gas phase:

$$Q = N_{22} F_R K_v(l) \sqrt{\frac{\Delta P(P_{in} + P_{out})}{M T_{in}}} \tag{2.3}$$

where Q is the volumetric flow rate (m^3/h), N_1 and N_{22} numerical constants, F_R the Reynolds number factor, ΔP the pressure drop (P_{out}-P_{in}) across the valve, ρ_w the density of the water, and ρ and M are the mass density and the molecular mass ($kg/kmol$), respectively, of the flowing fluid. K_v is the valve coefficient, and it is sometimes also referred to as C_v (where $C_v = 1.156\ K_v$). The valve coefficient K_v in (2.2), (2.3) is a function of the valve opening l [113]:

- Fast opening: $K_v/K_{v_{max}} = l^{\frac{1}{\alpha}}, \alpha > 0$
- Linear: $K_v/K_{v_{max}} = l$
- Equal percentage: $K_v/K_{v_{max}} = R^{l-1}$

where $K_{v_{max}}$ is the coefficient at maximum opening, while R and α are parameters provided by the manufacturer.

Finally, the transducer dimensions (specifically, delimited by the pressure and temperature sensor's positions) have to be sufficiently larger than the valve turbulence region. Therefore, in the following, the use of the Bernoulli equation is assumed as reasonable. (This assumption was also validated experimentally: conditions of turbulent flow were never surveyed in all the test points during the experiments of this case study at CERN.)

2.1.2 Alternative virtual flow meters

Both the models of Samson and Sereg-Schlumberger are derived from the Bernoulli equation. In this section, for both the methods, two different formulations are presented according to the gaseous or liquid phases of the helium. In the following, for the sake of simplicity, in cryogenics conditions the fluid is assumed as purely liquid when the temperature is below 5 K.

- Gasified helium Samson

$$A(p_{in}, p_{out}) = \begin{cases} 1; \quad \text{if} \quad \frac{p_{out}}{p_{in}} \leq (\frac{2}{\gamma+1})^{\frac{\gamma}{\gamma-1}} \\ \text{otherwise} \\ 1.379 \cdot \sqrt{\frac{2\gamma}{\gamma-1}(\frac{p_{out}}{p_{in}})^{\frac{2}{\gamma}} \cdot (1 - \frac{p_{out}}{p_{in}})^{\frac{\gamma-1}{\gamma}}} \end{cases} \tag{2.4}$$

$$\dot{m}(p, T) = 14.2 \cdot A(p_{in}, p_{out}) \cdot K_v \cdot \sqrt{\rho \cdot p_{in}} \tag{2.5}$$

- Liquefied helium Samson

$$\dot{m}(p, T) = 31.62 \cdot K_v \cdot \sqrt{\rho \cdot (p_{in} - p_{out})} \tag{2.6}$$

- Gasified helium Sereg-Schlumberger

$$p_v = 1.25; \qquad p_c = p_{in} \cdot (\frac{2}{\gamma+1})^{\frac{\gamma}{\gamma-1}} \tag{2.7}$$

$$p_{sc} = (0.96 - 0.28 \cdot \sqrt{\frac{p_v}{p_c}}) \cdot p_v \tag{2.8}$$

$$K_m = \frac{p_{in} - p_c}{p_{in} - p_{sc}} \tag{2.9}$$

$$X_c = 0.6 \cdot \gamma \cdot K_m; \qquad X = \frac{p_{in} - p_{out}}{p_{in}} \tag{2.10}$$

$$Y(p_{in}, p_{out}) = \begin{cases} \frac{2}{3} & \text{if } X \leq X_c \\ 1 - \frac{X}{3X_c} & \text{otherwise} \end{cases} \tag{2.11}$$

$$\dot{m}(p, T) = 23.6 \cdot K_v \cdot Y(p_{in}, p_{out}) \cdot \sqrt{X \cdot \rho \cdot p_{in}} \tag{2.12}$$

- Liquefied helium Sereg-Schlumberger

$$\dot{m}(p, T) = 23.3 \cdot K_v \cdot \sqrt{\rho \cdot (p_{in} - p_{out})} \tag{2.13}$$

where K_v is in both the cases the valve coefficient describing the valve characteristics.

2.1.3 Model of the Virtual Flowmeter-based Transducer

In the following, *(i) the operation model* and *(ii) the uncertainty model* of the virtual flowmeter-based transducer are illustrated.

Operation model

The virtual flow meter-based transducer measures the mass flow $\dot{m}$ of cryogenic helium through a valve by an indirect method [114]. A-priori knowledge about the valve and the actual helium behaviors is combined with measured pressure and temperature at the input and the output of the valve, as well as with an a-posteriori modeling, in order to assess the mass flow.

In Fig. 2.1 [114], the operation model of the transducer with the three models of the actual helium, the valve, and the virtual flow-meter integrated in its structure, are highlighted. Further details about the transducer operation principle can be found in [114].

Uncertainty model

In order to perform the uncertainty characterization of the transducer, a model of its actual behaviour was defined (Fig. 2.3). At this aim, the functions and the main uncertainty sources of the transducer were analysed. Pressure p_{in}, temperature T_{in}, and nominal mass flow $\dot{m}$ are input to the valve model. The valve behaviour is characterized by its coefficient K_v, corresponding to a defined aperture l affected by the associated uncertainty $u(l)$. On this basis, the valve model determines the output pressure p_{out} and temperature T_{out}. Input and output values of pressure and temperature are measured by means a set of four sensors, pointed out in Fig. 2.3 as PS and TS for pressure and temperature, respectively). The actual behaviours of the sensors are modeled by considering their measurement relative uncertainties u_p and u_T. Measured temperature (T'_{in}, T'_{out}) and pressure (p'_{in}, p'_{out}) are input to both the Helium and the virtual flowmeter models. The former model is mandated to simulate the thermo-physical behaviour of the helium when expanding through the valve, thus estimating its density ρ and the ratio γ between the heat capacity at constant pressure and the volume. ρ and γ (affected by the corresponding relative uncertainties, u_ρ and u_γ) along with the estimated value of K_v are input to the virtual flowmeter model, based on the Sereg-Schlumberger equations [24]. This model estimates the desired mass flow, with an uncertainty u_{model} assessed through the experimental campaign reported in [114].

1. Model parameters

The uncertainty model of the transducer is defined in order to single out the dependency of the metrological performance $\mathbf{P} = (P_1, ..., P_k)$ at the model output over

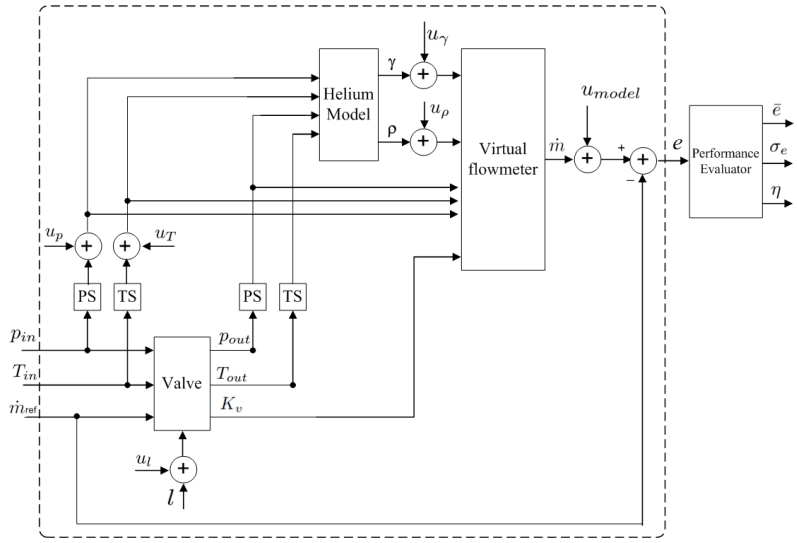

Figure 2.3: Behavioral model of the virtual flowmeter-based transducer for the uncertainty analysis

its operating domain D=(***i***, ***s***, ***c***, ***u***) (Fig. 2.3), defined by the following parameters:

(i) *Measurands* $\boldsymbol{i} = (i_1, ..., i_m)$, the array of quantities to be measured at the model input; namely, for the transducer, the mass flow $\dot{m}$ through the valve to be assessed indirectly by starting from the direct measurements of helium temperature and pressure at the input and output of the valve;

(ii) *Settings* $\boldsymbol{s} = (s_1, ..., s_z)$, the control parameters defined by the operator, namely the valve opening l, considered owing to its direct action on the transducer behavior;

(iii) *Operating conditions* $\boldsymbol{c} = (c_1, ..., c_n)$, the parameters characterizing the external environment where the transducer is operating, namely pressure and temperature at valve input and output p_{in}, T_{in}, p_{out} and T_{out}, respectively, expressing the main working conditions for the cryogenic helium;

(iv) *Uncertainty sources* $\boldsymbol{u} = (u_1, ..., u_q)$ (detailed in the next subsection), affecting the transducer performance, expressing the non-ideal behaviours of components and the unknown influence of environment.

2. Uncertainty sources

In the flowmeter-based transducer, the main significant non-ideality sources $\boldsymbol{u} = (u_1, ..., u_q)$ were identified in:

(i) the uncertainty u_T, affecting both the input and output temperature transducers, and assessed as the instrumental uncertainty;

(ii) the uncertainty u_p, affecting both the input and output pressure transducers, again defined as the instrument uncertainty;

(iii) the uncertainty u_ρ, affecting the Helium density provided by the fluid model, and assessed as the model uncertainty;

(iv) the uncertainty u_γ, affecting the Helium heat capacity ratio provided by the gas model, again assessed as the model uncertainty;

(v) the uncertainty u_l, associated to the knowledge of the valve opening l (in fact, l determines the value of the coefficient K_v, and thus affects the mass flow estimate), assessed in terms of the precision of the determination of the opening level;

(vi) and the mean percentage error u_{model} associated to the Sereg model, ad assessed in the experimental campaign reported in [114].

Main twofold scopes of the metrological analysis are to determine if the influence of these uncertainty sources is significant, and to rank their impact on the metrological performance detailed in the next subsection.

3. Metrological performance

In the uncertainty model of the virtual flow-meter-based transducer, the metrological performance $\mathbf{P} = (P_1, ..., P_k)$ is expressed in terms of the differences between estimated $\dot{m}$ and reference $\dot{m}_{ref}$ mass flow, in different, defined measurement conditions (i.e. for combinations of the model parameters values varying in defined, limited sets). In particular, the transducer overall error e is expressed as percentage of the reference:

$$e = \frac{\dot{m} - \dot{m}_{ref}}{\dot{m}_{ref}} \cdot 100. \tag{2.14}$$

e is processed to determine the following metrological performance indexes:

- the *deterministic error*, assessed as the average over the N error samples e_k observed in each k^{th} configuration,

$$\bar{e} = \frac{1}{N}\sum_{k=1}^{N} e_k, \tag{2.15}$$

- the *uncertainty*, assessed as the associated standard deviation,

$$\sigma_e = \sqrt{\frac{1}{N-1}\sum_{k=1}^{N}(e_k - \bar{e})^2}, \tag{2.16}$$

- and the *total metrological performance*, combining both deterministic error and uncertainty, and assessed as the decomposition of the error sum of squares [115]:

$$\eta = \bar{e}^2 + \frac{N-1}{N}\sigma_e^2. \tag{2.17}$$

Valve model

The uncertainty model of the transducer includes a 3D model of a cryogenic valve by WEKA [116], with two parts: the body and the valve plug (Fig. 2.4). The cryogenic

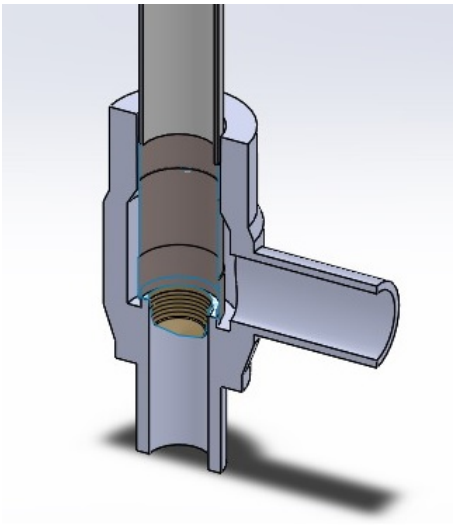

Figure 2.4: 3D CAD model of the cryogenic valve: plug *(grey)* and body *(light grey)*

flow behavior has been modeled through Computational Fluid Dynamics (CFD) analysis. In particular, the software package ANSYS® Fluent, included in the platform Workbench™ ANSYS®, was used to run the CFD simulations. The fluid domain, corresponding to the valve volume, was meshed. An optimum number of elements and nodes, in order to create a grid independent system, was found after several tests. A pipe 10 times longer than the diameter was added to the 3D model to provide a fully developed flow at the valve inlet.

Furthermore, the following boundary conditions were set: *(i)* the turbulence intensity at valve inlet and output equal to 1% and 2%, respectively; *(ii)* a mass flow normal to the valve inlet surface; *(iii)* a no-slip condition on the valve and pipe walls; and *(iv)* an adiabatic simulation.

The CFD software solved the Reynolds-averaged Navier-Stokes equation and the Shear Stress Transport (SST) k-ω [117] was chosen as turbulence model. Among all the tested turbulence models, the SST k-ω yielded the best fit with the experimental data. In the pressure-based solver, the coupled configuration was chosen to solve the governing equations of the steady-time problem. Finally, a second-order upwind scheme was used for the spatial discretization in all the equations, being more precise than the first-order scheme, and the most accurate for this kind of problem with mesh configuration.

The above-described configuration was chosen according to the knowledge of the experimental conditions (experimental data, cryogenic system setup, and so on), and the information provided by WEKA. For running the model, the knowledge of valve parameters, i.e. its coefficient (K_v) and opening (Op), are needed.

2.2 FAULT DETECTION: cryogenic cold compressors with Active Magnetic Bearings

2.2.1 Basic concepts

The key idea, underlying the proposed method, is to exploit the uncertainty inside a single record of the nominal condition, to characterize its natural variability. Therefore, few records of the nominal conditions are needed to statistically characterize its behavior. In details, in a former stage, when the system is guaranteed to work properly, few records are acquired and the nominal condition is characterized. Then, at a later stage, maintenance campaigns are conducted on the same system, with the aim of checking if a faulty condition has occurred. Moreover, some information about

fault isolation can be obtained by analyzing the distance between the values of the chosen figure of merit in the two considered cases and its sensitivity to the model parameters. The method is intended to be used during maintenance tests, where the main influence parameters, such as temperature and rotational speed of the compressor, can be controlled, thus the uncertainty of the unfaulty condition is assumed to be dominated by the noise overlapped on few FRF records.

In particular, the proposed early-stage fault isolation consists of four phases:

- *Modeling the unfaulty condition*: A model based on the FRF representing the nominal behavior is defined and identified from few actual records of measurements taken from a compressor in unfaulty condition. In particular, few frequency-domain records are extracted from the system working in unfaulty condition, and, from such data, a parametric model is identified, using a Total Least Squares approach. The use of a parametric model allows the significant behavior of the faulty condition to be described and to be separated from the overlapped noise.

- *Characterization of the unfaulty condition*:

  Then, the noise power on the records is assessed together with its variance, by evaluating the residuals between the records and the model. The variance of the noise power represents the effect of variation of the estimated parameter due to the noise overlapped to the acquired records. In the paper, (i) the acquired records are considered as corrupted by white Gaussian noise, and (ii) the variance of the remaining noise on the record, filtered by the model application, is assumed much lower than that of the noise on the original records. For the purpose of the fault detection, the evaluated variance is taken into account in order to characterize the variability range of the unfaulty behavior, and to classify not significant changes in the system behavior.

- *Fault detection*: During the maintenance tests, the FRF of the system under test is measured. A statistical test detects an eventual faulty condition by pointing out a significant deviation of the noise power assessed during the maintenance test from the reference noise in the unfaulty condition. In particular, the statistical test evaluates the variance of the noise power.

- *Early-stage fault isolation*: A sensitivity analysis is carried out on the model, in order to (i) identify the most influencing parameters, and (ii) determine the ranges of variation of the most influencing parameters, that cause significant

alteration in the noise power estimate. The method does not allow a complete fault isolation. However, by considering the results of the sensitivity analysis, and evaluating the deviation in the values of the figure of merit, evaluated during the maintenance test and in the unfaulty condition, the set of parameters, whose variations have caused the faults, can be identified with high probability.

In the following subsections, each step of the proposed method is detailed.

2.2.2 Modelling the nominal system

The model of the system is obtained from the measured frequency response, as described in Ref. [118]. The frequency response can be written from the system transfer function:

$$h(f, \boldsymbol{\theta}) = \frac{n(f, \boldsymbol{\theta})}{d(f, \boldsymbol{\theta})} \tag{2.18}$$

where, f is the frequency in the set $[f_1, f_2, \ldots, f_N]$, θ is the vector of the coefficients of the numerator and denominator polynomials $\boldsymbol{\theta} = \begin{bmatrix} \boldsymbol{\theta}_n & \boldsymbol{\theta}_d \end{bmatrix}$, $n(f, \boldsymbol{\theta})$ and $d(f, \boldsymbol{\theta})$ are the numerator and denominator polynomials, respectively, defined as:

$$n(f, \boldsymbol{\theta}) = \sum_{j}^{n} \theta_{nj} \omega_j; \quad d(f, \boldsymbol{\theta}) = \sum_{j}^{n} \theta_{dj} \omega_j \tag{2.19}$$

with θ_{nj} and θ_{dj} the j-th elements of $\boldsymbol{\theta}_n$ and $\boldsymbol{\theta}_d$, respectively, and $\omega_j = e^{-i2\pi f_j T_s}$, being T_s the sampling period.
In general, the polynomial order n of the denominator and numerator can differ. The linearized (weighted) Least-Squares (LS) equation error ε_k is obtained by rewriting (2.18) with the samples h_k of the measured frequency response function and multiplying with the denominator polynomial $d(f, \boldsymbol{\theta})$:

$$\varepsilon_k(\omega_f, \theta) = W_k n_k(f, \boldsymbol{\theta}) - h_k d_k(f, \boldsymbol{\theta}) \approx 0 \tag{2.20}$$

where, W_k is a frequency-dependent weighting function which can be used to improve the estimator.
As (2.20) is linear-in-the-parameters and in the Fourier data, it can be reformulated as:

$$\varepsilon = \boldsymbol{J}\boldsymbol{\theta} \approx \mathbf{0} \tag{2.21}$$

where:

$$\boldsymbol{J} = \begin{bmatrix} \boldsymbol{\Gamma} & \boldsymbol{\Phi} \end{bmatrix}, \tag{2.22}$$

with:

$$\boldsymbol{\Gamma} = \begin{bmatrix} \boldsymbol{\Gamma_1} \\ \boldsymbol{\Gamma_2} \\ \vdots \\ \boldsymbol{\Gamma_N} \end{bmatrix}, \quad \boldsymbol{\Phi} = \begin{bmatrix} \boldsymbol{\Phi_1} \\ \boldsymbol{\Phi_2} \\ \vdots \\ \boldsymbol{\Phi_N} \end{bmatrix}, \tag{2.23}$$

$$\boldsymbol{\Gamma_k} = W_k \boldsymbol{\omega}, \quad \boldsymbol{\omega} = [\omega_1, \omega_2, \ldots, \omega_n] \tag{2.24}$$

$$\boldsymbol{\Phi_k} = -\boldsymbol{\Gamma_k} h_k \tag{2.25}$$

It should be noted that the matrix $\boldsymbol{J}$ is independent on the parameter $\boldsymbol{\theta}$ to be estimated, as (2.20) is linear-in-the-parameters. Therefore, the size of $\boldsymbol{J}$ can be reduced by formulating the normal equations:

$$\boldsymbol{J^H J \theta} = \begin{bmatrix} \boldsymbol{R} & \boldsymbol{S} \\ \boldsymbol{S^H} & \boldsymbol{T} \end{bmatrix} \boldsymbol{\theta} \approx \boldsymbol{0} \tag{2.26}$$

with $\boldsymbol{R} = \boldsymbol{\Gamma^H \Gamma}$, $\boldsymbol{S} = \boldsymbol{\Gamma^H \Phi}$ and $\boldsymbol{T} = \boldsymbol{\Phi^H \Phi}$.
These matrices have a Toeplitz structure and can be constructed in a fast way. Elimination of the numerator coefficients from (2.26) by substitution of

$$\boldsymbol{\theta_n} = \boldsymbol{R^{-1} S \theta_d} \tag{2.27}$$

results in the so-called reduced normal equations:

$$\left[\boldsymbol{T} - \boldsymbol{S^H R^{-1} S}\right] \boldsymbol{\theta_d} = \boldsymbol{M \theta_d} \approx 0 \tag{2.28}$$

It has been proven in Ref. [118] that the LS or TLS solutions for $\boldsymbol{\theta_d}$ obtained by solving the compact problem (2.28) are the same as obtained by solving the full problem (2.26) with the same constraint. Once the denominator coefficients are determined, back substitution in (2.27) is used to derive the numerator coefficients.

2.2.3 Noise power estimation

Once the model has been obtained, a record, representing the nominal behavior cleaned of the noise, can be obtained from (2.18), where the coefficients of the numerator and the denominator, obtained from (2.28) and (2.27), have been substituted. Assuming that the acquired records are corrupted by white Gaussian noise, with variance σ_w^2, and that the variance of the remaining noise on the record, filtered by the

model application is much lower than that of the noise on the original records, an estimate of the noise power can be obtained from the residuals:

$$\boldsymbol{r} = \boldsymbol{h} - \hat{\boldsymbol{h}} \tag{2.29}$$

In particular, indicating with $\bar{P}_r$ the mean squared value of $\boldsymbol{r}$:

$$\bar{P}_r = \frac{1}{N}\sum_{i=1}^{N} r_i^2, \tag{2.30}$$

under the assumption that r_i are Gaussian distributed with null mean and variance σ_w^2, it follows that $\bar{P}_r N/\sigma_w^2$ is chi-squared distributed with N degrees of freedom[**?**]. Therefore, taking the mean value leads to:

$$\mathrm{E}\left\{\frac{\bar{P}_r N}{\sigma_w^2}\right\} = N. \tag{2.31}$$

An estimate of σ_w^2 is then obtained directly evaluating $\bar{P}_r$:

$$\hat{\sigma}_w^2 = \bar{P}_r \tag{2.32}$$

Taking the variance of $\bar{P}_r N/\sigma_w^2$ leads to:

$$\mathrm{Var}\left\{\frac{\bar{P}_r N}{\sigma_w^2}\right\} = 2N, \tag{2.33}$$

and:

$$\mathrm{Var}\left\{\bar{P}_r\right\} = \mathrm{Var}\left\{\hat{\sigma}_w^2\right\} = \frac{2}{N}\sigma_w^4. \tag{2.34}$$

For large N, the noise power estimate can be approximated as being Gaussian distributed with mean σ_w^2 and variance $\frac{2}{N}\sigma_w^4$.

2.2.4 Fault detection

Having characterized the nominal condition, a binary hypothesis test can be defined to detect the fault on newly acquired records. As mentioned in the previous subsection, the power of residuals, computed on the original records P_{REF}, acquired in nominal condition, is a Gaussian distributed random variable, with mean σ_w^2 and variance $\frac{2}{N}\sigma_w^4$. Instead, the power of residuals computed from the records of the system under test P_{SUT}, is also a random variable, but its distribution depends on the presence of

the fault.
Therefore, the following hypothesis can be defined:

$$\begin{aligned} H_0 &: \quad \text{a fault has not occurred} \\ H_1 &: \quad \text{a fault has occurred} \end{aligned}$$

Under the hypothesis H_0, the power of residuals computed on a record acquired during the maintenance test is also Gaussian distributed with the same mean and variance of the record in unfaulty condition.
Under the hypothesis H_1, instead, the power of residuals can be still approximated as Gaussian distributed, however, it has a nonzero mean. The difference $P_{SUT} - P_{REF}$, under the hypothesis H_0, is also Gaussian distributed with null mean and variance equal to $2\,\mathrm{Var}\{P_{REF}\} = \frac{4}{N}\sigma_w^4$.
Therefore, the following test can be defined to discriminate between a non-faulty and a faulty condition, respectively:

$$\begin{aligned} &\text{if } P_{SUT} - P_{REF} \geq \tau \quad \text{then reject } H_0 \\ &\text{if } P_{SUT} - P_{REF} < \tau \quad \text{then do not reject } H_0 \end{aligned}$$

where τ is a threshold that can be obtained from the Gaussian distribution by fixing a certain probability of false alarms.
In details, indicating with P_{fa} the probability of false alarm, the threshold τ is obtained from:

$$\tau = 2\sqrt{\mathrm{Var}\{P_{REF}\}} \cdot \mathrm{erf}^{-1}(2(1 - P_{fa}) - 1), \tag{2.35}$$

where $\mathrm{erf}(\cdot)$ is the error function.

2.2.5 Early-stage fault isolation

A sensitivity analysis allows the most influencing model parameters to be identified and their influence on the estimated noise power to be assessed. In particular, the analysis consists of two subsequent steps: *(i) parameters ranking*, and *(ii) faulty parameter identification*.

Parameters ranking

An analysis of variance (ANOVA) is carried out on the model parameters, using as figure of merit the estimated noise power. Such an analysis allows the most influencing parameters among all the coefficients of the model to be identified. This is carried out by assessing the noise power variation versus the variation of the model parameters.

Considering the set $\mathcal{S}$ of the most influencing parameters, let indicate by $\mathcal{R}$ and $\mathcal{C}$, the subsets of the real poles and of the complex poles, respectively, and be p the cardinality of $\mathcal{R}$ and q the cardinality of $\mathcal{C}$. In particular, variations are introduced on the real poles, the damping ratios and the frequencies, thus giving a vector $\mathbf{u} = \begin{bmatrix} u_1 & u_2 & \dots & u_{p+2q} \end{bmatrix}$, where $\begin{bmatrix} u_1 & u_2 & \dots & u_p \end{bmatrix}$ are variations of the real poles, $\begin{bmatrix} u_{p+1} & u_{p+2} & \dots & u_{p+q} \end{bmatrix}$ are variations of the damping ratios, and $\begin{bmatrix} u_{p+q+1} & u_{p+q+2} & \dots & u_{p+2q} \end{bmatrix}$ are variations of the frequencies. Then, on this basis, the significance of the impact of each model parameter on the figure of merit (noise power P_n) is assessed.

In Ref. [26], a method for determining the optimum set of experiments, in terms of subspace points of the operating domain and minimum number of tests, for performing the desired analysis within a prefixed significance is defined. This is a well-known approach of design of experiments, mainly based on the basic idea of exploring only the points related to the desired information.

At this aim, a plan of experiments[119] is adopted for its capability of investigating combinatorial spaces generated by several multi-levels discrete parameters. In particular, for the *i-th* parameter, the nominal value p_i plus/minus the variability range is chosen. This range is defined according to the actual system knowledge. The probability that the variation associated with the considered parameter does not influence the corresponding performance factor is indicated according to a multi-way ANOVA and the traditional Fisher-Snedecor statistical test.

Faulty parameter identification

The most influencing parameters are analyzed with the aim of finding a quadratic model approximating the influence of such parameters on the noise power estimation. In this way, the sensitivity of the figure of merit to the different model parameters can be assessed, and the values that the model parameters can assume in case of fault can be identified. In particular, once the most influencing parameters are identified by the ANOVA, new experiments are performed using the Box-Behnken design [25].The Box-Behnken design (BBd) is an independent quadratic design because does not contain an embedded or fractional factorial design. In this design, the treatment combinations are at the midpoints of edges of the process space and at the center. These designs are rotatable (or near rotatable) and require 3 levels of each factor. When the analysis is relatively close to the optimum, a second-order model is usually required to approximate the response because of curvature in the true response surface [120].

Therefore, the results obtained from the experiments selected by the BBd allows the following second-order model, representing the behavior of the noise power versus the variation of the model parameters, to be fitted:

$$f(u_{i_1},\ldots,u_{i_L}) = \beta_0 + \sum_{l=1}^{L}\beta_l u_{i_l} + \sum_{l=1}^{L}\beta_{ll}u_{i_l}^2 \quad + \sum_{l<m}\sum\beta_{lm}u_{i_l}u_{i_m} \tag{2.36}$$

where L is the number of parameters $\begin{bmatrix} u_{i_1} & u_{i_2} & \ldots & u_{i_L} \end{bmatrix}$ selected by means of the ANOVA. Suitable variations are chosen for the model parameters. Considering these factors, a corresponding number of runs is performed for the BBd. The noise power P_n is then evaluated for each run, and used to estimate, with the least square method, the coefficients $\beta_0, \beta_l, \beta_{ll}, \beta_{lm}$. The intersection with the plane corresponding to the threshold value highlights the locus of the intersecting points. In this way, the subspace of the model parameters that will cause a faulty condition is identified.

2.3 FAULT DIAGNOSIS: Decentralized diagnostics for large experimental systems

2.3.1 Multiple fault diagnosis

In monitoring complex experimental systems, the most challenging problem of finding the causes of several simultaneous anomalies (Multiple-Fault Diagnosis) [40] is stated as an *adductive* problem [41]: the hypothesis, i.e., the set of causes, best explaining the observed anomalies, is to be found. Combinatorially, it can be stated as [41]: given a graph with N nodes numbered from 1 to N, an accurate permutation of N elements among 2^N in the worst case verifying a specified rule has to be found. This problem is classified as a hard combinatorial optimization, here formalized as:

- the 4-tuple $\langle D, M, C, M^+\rangle$, where D is a finite nonempty set of faults d, M is a finite set of anomalies (symptoms) m, C is a relation defined as a subset of DM, pairing faults with the corresponding anomalies, and $M^+ = \{m_1, m_2, \cdots, m_u\}$ is a subset of M identifying the observed anomalies. Namely, $(d, m) \in C$ means that the fault d may cause the anomaly m.

- the diagnosis DI is the solution of the problem, defined as the subset of D identifying the faults eventually responsible for the anomalies in M^+.

- an *a priori* probability p_j is associated to each fault d_j in the set of faults D. Values are assumed to exist and faults in D are assumed to be statistically independent.

- moreover, the relation C, pairing faults with the corresponding anomalies, is assumed to be a matrix of causal strength c_{ij}, (such that $0 < c_{ij} < 1$), representing how frequently a fault d_j causes the anomaly m_i. Formally, the causal strength c_{ij} is expressed as the conditional probability P (d_j causes $m_i|d_j$), i.e., the fault d_j causes the anomaly m_i.

Symbolic, causal, and numeric probabilistic knowledge is exploited to generate and assess plausible hypotheses about DI. At this aim, a relationship for calculating the relative likelihood, denoted as $L(DI, M^+)$, of a diagnosis DI, given the observable anomalies M^+, can be derived. The likelihood is the product of three factors:

$$\begin{aligned} L(DI, M^+) &= L_1 L_2 L_3 = \\ &\left\{ \prod_{m_i \in M^+} \left[1 - \prod_{d_j \in DI} (1 - c_{ij}) \right] \right\} \times \\ &\times \left\{ \prod_{d_j \in DI} \left[\prod_{m_l \in effects(d_j) - M^+} (1 - c_{ij}) \right] \right\} \times \\ &\times \left\{ \prod_{d_j \in DI} \left[\frac{p_j}{(1 - p_j)} \right] \right\}. \end{aligned} \tag{2.37}$$

where

- L_1 is the likelihood that faults in DI cause the anomalies in M^+. For a diagnosis not covering M^+, L_1 evaluates to 0, thus forcing L to 0.

- L_2 is the likelihood that faults in DI do not cause anomalies outside of M^+. Ideally, L_2 values close to 1 are preferred.

- L_3 is the likelihood that a highly probable fault d_j contributes significantly in the overall likelihood of a diagnosis DI containing d_j.

L in (2.37) has to be maximized in order to find the most probable causes (faults) determining the observed anomalies.

2.3.2 Distributed micro-genetic algorithm

In this section, the concept design, the working principle, and the procedure of the distributed micro-genetic algorithm for multiple-fault diagnostics are illustrated.

Concept design

The architecture of the proposed distributed system for automatic monitoring and multiple-fault diagnostics of large experimental systems is depicted in Fig. 2.5. Two distributed functions are integrated at physical level on a network of smart transducers: (*i*) monitoring and fault detection (continuous line in Fig. 2.5), for measuring and processing the main parameters of the system, as well as detecting possible anomalies, and (*ii*) diagnostics (dashed line), for finding the corresponding faulty causes. When one or more transducers (Monitoring Units in Fig. 2.5) detect a set of anomalies M^+, the monitoring system expands its capabilities and a diagnostic process is triggered.

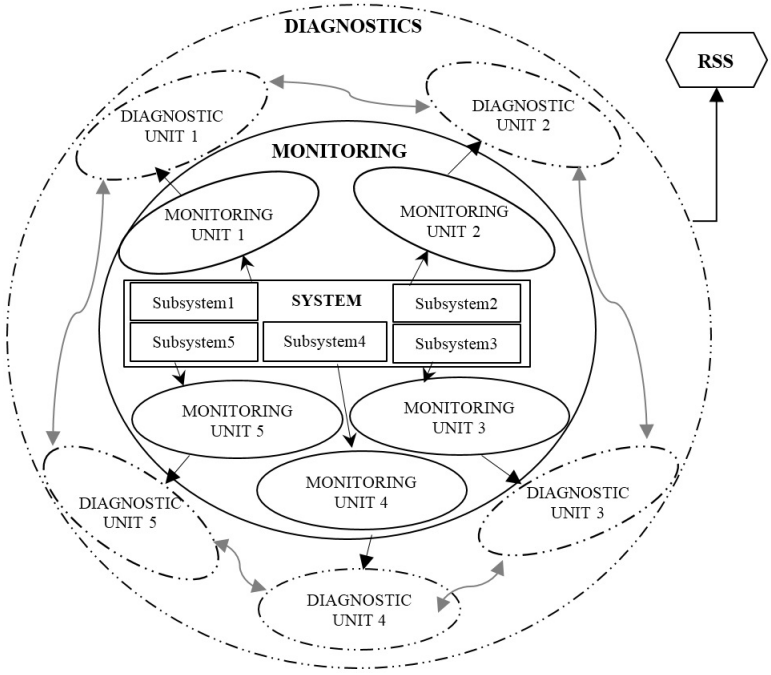

Figure 2.5: Architecture of the distributed monitoring and multiple-fault diagnostics.

Each smart transducer acts as an isolated processor (Diagnostic Unit in Fig. 2.5) executing a local independent task in order to determine the final diagnosis DI. This multiple-fault diagnostics function is based on a distributed Micro-Genetic Algorithm (dMGA). Different algorithm instances, allocated on the transducers of the monitoring network, evolve independently in parallel [121]. At each T generations (*immigration interval*), the adjacent processes exchange their best individuals synchronously, according to the *elitist stepping-stone migration* model with a bi-directional ring topology [122]. This topology is based on a classical *coarse-grained* approach [121]: each instance on the Diagnostic Units is connected locally to other two instances, in order to exchange best individuals during the migration phase (bidirectional gray arrows in Fig. 2.5). For distributed networks monitoring large systems, this topology has several advantages: (*i*) improved efficiency owing to the parallel process, shortening time execution, and fostering population diversity; (*ii*) broadcast communication network emulated via point-to-point connections; (*iii*) extension up to geographical distances; (*iv*) increased reliability and easy network re-modulation in case of a faulty node, because only the transducers in other subnets sending messages to the faulty node are affected; and (*v*) very-low cost of implementation and maintenance.

dMGA communications exploit the *message passing interface* (MPI) concept [54], widely adopted to develop portable parallel programming. Most important features are: essential virtual topology, synchronization and communication function among a set of processes mapping network nodes in a language-independent way, with language-specific syntax (bindings), plus a few language-specific features.

In the concept design of the dMGA, the difficulty of integrating the diagnostic knowledge into a unique representation for a complex, dynamic, and distributed system is solved by twofold distribution mechanisms [123]: *(i) spatial*, where the knowledge is integrated from different local diagnostic processes placed in different subsystems and *(ii) semantic*, where the knowledge is integrated from different fields of expertise, related to the system physics, structure, and so on.

In the architecture of Fig. 2.5, the diagnostic process is *decentralized* (non-distributed) because each spatially de-localized processor shares the same information about the relationships anomaly-faults. In particular, a processor not only has detailed knowledge about its monitored sub-system but also an abstract view of the neighbouring subsystems and of the system as a whole. Cooperating processors diagnose faults affecting more than one subsystem. A node triggers the cooperation process locally, when it realizes that the anomalies cannot be explained only within its subsystem. The cooperation process is driven by a small amount of topological information. The

Remote Supervision Station (RSS in Fig. 2.5) is not involved in such a diagnostic process and acts mainly as a final user interface. This decreases diagnostic response time dramatically for large experimental systems. Conversely, for a centralized diagnostics, the size of the system description is linear in the processor number and execution time will usually be even worse than linear [124]. Moreover, all observations have to be transmitted to the central diagnosis machine, causing a large communication overhead.

The diagnostic process so conceived turns out to be *global*, because the nodes exchange continuously information about all the anomalies and the same information about the relationships anomaly-faults. Conversely, the dMGA computing for the solution search is *distributed*, because each processor scans the solution space independently from the others. The unique information shared among evolutions allocated on different processors is the best solution.

Working principle

The working principle of the dMGA is highlighted by referring to its main design issues: (i) the *initialization*, (ii) the *knowledge coding*, (iii) the *fitness*, and (iv) the *operators*.

1. Initialization

At the beginning, for each dMGA instance situated on the node of the transducer network, each population of N individuals is sampled randomly through a pseudo-random generator with different seeds. Consequently, each instance starts its search from a different place of the solution space.

2. Knowledge coding

Given a set of relieved anomalies $M^+ = \{m_1, m_2, \cdots, m_u\}$ as input, the dMGA returns the solution diagnosis as a sequence of multiple faults $DI_{best} = \{d_1, d_2, \cdots, d_v\}$. The individuals are designed as binary strings with length v equal to the cardinality of DI. At each generation, evolutionary operators update the individuals by modifying their own genes (bits).

Each gene corresponds to one and only one fault in DI, thus each individual represents a potential multiple-fault diagnosis causing the anomalies M^+. The gene is expressed, i.e., the bit value is 1, if the corresponding fault is present in the diagnosis as a probable cause in the solution. Conversely, it is 0. Each individual, corresponding to a diagnosis DI, is assessed through the fitness for checking its attitude to represent

the sequence of faults causing M^+.

3. Fitness

Each individual, representing a potential diagnosis DI, is assessed by means of (2.37) for estimating the correspondence between the diagnosis it encodes and the most likely sequence of faults causing M+ found until now. The likelihood $L(DI, M^+)$ is assessed by exploiting the matrix C reporting the uv causal strengths anomalies/faults. During the evolution, an individual is selected as the best until the diagnosis it encodes has the greatest likelihood.

4. Operators

On each node of the transducer network, the dMGA instances initialize their own populations composed of N individuals and perform the optimization process by applying, at each generation, for a maximum number G_{max}, the following six evolutionary operators:

1. *Elitism*: Memory about the best solution achieved so far is kept by introducing the survival of the best individual. Elitism reserves a place in the offspring for the individual of the current generation with highest fitness, by avoiding that other evolutionary operators affect its genome [125].

2. *Tournament selection*: Individuals are selected for participating to a mating pool in order to generate the offspring for the next generation. The selection relies on several tournaments among groups composed of a number of individuals (the *tournament size* parameter, equal to $N/2$ in dMGA) randomly selected without replacement from the population. In each tournament, the individual with higher fitness wins and becomes an element of the parent population for reproduction. Generally, the needed tournaments number is equal to the population size, but in dMGA it is equal to $N - 1$ owing to the elitism.

3. *One-point crossover*: It is a very common crossover variant for GAs. Initially, a unique genome point is randomly chosen with a probability P_C for two parent individuals. Subsequently, the part of the individuals genome situated after the point is swapped between the parent individuals, by reproducing two child individuals.

4. *Bit-flip mutation*: Usually, mutation is not used in MGA because the diversification of the population relies on re-initialization operator. However, in dMGA, it results very useful to increase population and thus the solution diversity. At

this aim, the genome bits of the child individual are flipped according to a probability P_M. In practice, a bit is probabilistically inverted in its complementary.

5. *Re-initialization*: This is a peculiar operator of MGAs.12 Its dMGA application supports the exploration phase, otherwise penalized by the small size of the population. At each generation, the re-initialization operator checks if the genome of the highest-fitness individual has a bit number less than a given percentage H_{micro} from the other population elements. In this case, a nominal convergence is relieved and the operator applies a new initialization. Otherwise, the re-initialization operator is applied when evolutionary process reaches a number of inner generations (or *micro-cycle*) equal to G_{micro}.

6. *Migration*: Solutions achieved in different evolutionary algorithms running in parallel can be exchanged by means of the migration operator. This permits single executions to share their search spaces by generating, as a consequence, a global search process involving the distributed algorithm as a whole. The dMGA migration operator is based on the above mentioned classical elitist stepping-stone migration [122]. Specifically, at every fixed generation interval T, the copies of the best local individuals migrate between neighbouring node processors DU. Once reached a neighbouring processor, the copy replaces an individual randomly selected among the individuals of the host population but differing from the local best one.

Procedure

dMGA consists of a set of MGAs instances assigned to different smart transducers and provided with the above operators. These instances run in parallel in a folded bi-directional ring topology with a process casually set as master. The master process acts as an interface to the user, e.g., the Remote Supervision Station (RSS of Fig. 2.5): it collects the current local best solutions of the slave processes and saves the best element at each generation. Moreover, it compares this latter solution to the best found so far, saves the best among them, and transmits them to RSS. The dMGA procedure includes the following steps (Fig. 2.6):

1. For each MGA instance allocated on the *DU* of a smart transducer, a small-size population is initialized.

2. For each individual of the instance, the fitness value is assessed.

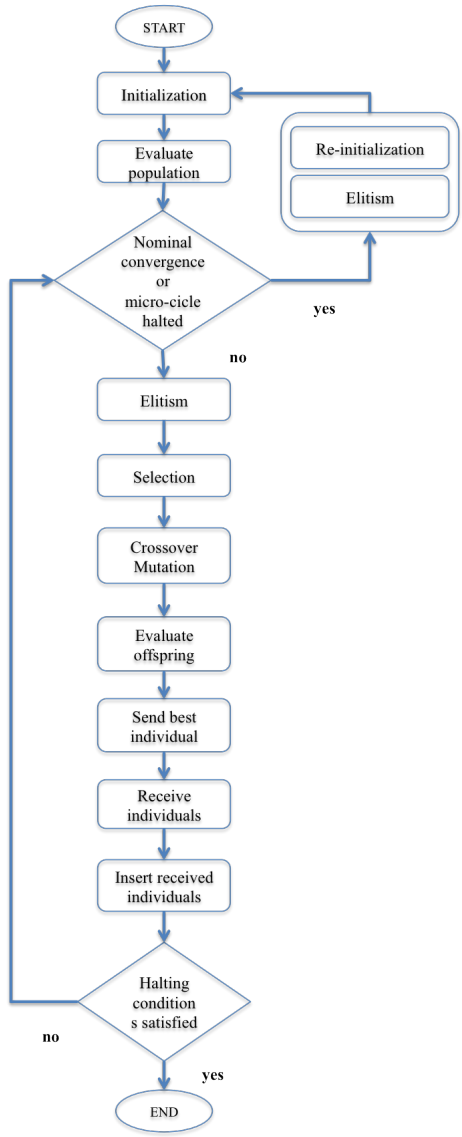

Figure 2.6: Procedure of dMGA.

3. For each instance, if the nominal convergence subsists or a micro-cycle halts, the local best individual is cloned via the elitism operator and the rest of the local population is re-initialized. Afterword, the procedure comes back to step2.

4. In each local population of an instance, the best local individual is cloned by elitism and added to the local offspring.

5. Locally, for each instance, individuals are chosen by means of the selection operator for reproduction.

6. Both crossover and mutation operators are applied to each group of reproductive individuals selected in the different dMGA instances in order to generate local offspring.

7. The fitness of the new individuals belonging to every local offspring is evaluated.

8. In each dMGA instance, the local best individual is sent to the neighbouring instances.

9. Each dMGA instance receives the copies of the best individuals sent by the neighbouring instances.

10. In each local population, the received individuals replace other ones randomly chosen but different from the local best individual.

11. If a halting condition is satisfied (number max of generations, reached convergence, and so on), the corresponding dMGA instance halts; otherwise, the procedure returns to step 3.

2.4 PREDICTIVE MAINTENANCE

2.4.1 Problem statement

The main idea of this work is to evaluate GEO's algorithm performance on large experimental systems.

In this section, a function that takes into account the cost associated to the maintenance action (for example, the replacement or the calibration of a given component), and the cost associated to the system operating in the normal state (as monitoring, inspection and so on) is defined. Thanks to that, the effects of whatever given maintenance operation can be assessed.

Let N be the available resources to maintenance operation, and m_i (for i=1,..., M) the i^{th} system component that must be maintained (for a total of M components).

The function C, representing the total cost of planned maintenance, can be expressed as:

$$C = \sum_{t=1}^{T} [\sum_{i \in G_t} (a_i + p_i(t) \cdot B_i) + \sum_{j \in H_t} (k_j + b_j)] \tag{2.38}$$

where:

-T finite time horizon of planned maintenance;

-t for t = 1, ..., T, the $t-th$ instant of the time horizon T;

-a_i the operating cost of the $i-th$ component;

-k_j the replacement cost for the $j-th$ component;

-b_j maintenance cost of the $j-th$ component;

-$p_i(t)$ probability of failure of the $i-th$ component at the time t;

-B_i cost of breakdown of the $i-th$ component;

-G_t the set of every component not maintained at the time t;

-H_t the set of every maintained component at the time t.

Moreover, each given planned maintenance evaluated by means of (2.38) is subject to the following constraints:

i) Each m_i can be served (maintained) by only one of the N available resources at any time t;

ii) Each m_i has to be served at least one time instant t during the total time horizon T.

Finally, the probability of failure p_i at the time t could be derived from various deterioration models, depending on the type of monitored component, and from the nature of information or acquired signals.

2.4.2 The proposed method

In the present work, each maintenance schedule S (called sequence, in the following) assessed by (2.38) is expressed through a binary string representation as:

$$S = [s_{11}, s_{12}, ..., s_{1M}; .....; s_{T1}, s_{T2}, ...s_{TM}] \tag{2.39}$$

where the single s_{TM} is the value of the corresponding bit. For example, s_{23} =1 means that the third component is maintained at the time instant t =2. The sequence representation in (2.39) is suitable for the proposed GEO approach. The maintenance problem is hard to solve even for apparently simple cases [126], as the time required for computing an optimal solution increases rapidly with the size of the study case.

Generalized extremal optimization

The goal of the proposed method is to find the best sequence, expressed as in (2.39), that minimizes the objective function (2.38) for the above problem. Let us consider a sequence (i.e., a maintenance schedule); a sequence can be encoded in a binary string, denoted by S of length $(M \cdot T)$ by means of the representation shown in (2.39). This sequence expression is particularly suitable to be faced through a GEO. Indeed, in analogy to what EO algorithm does, GEO works on a population (configuration) by muting, generation after generation, a single species (component) and by estimating the obtained candidate solution, for reaching the optimum. Thus, if each representation bit encodes a single species, then an entire population can be expressed by means of a binary string, hence by a sequence in the form (2.39) too. For the above reasons, a GEO algorithm can straightly work on a sequence S by evaluating the candidate solution to the considered maintenance problem through the cost function (2.38). This means that the lesser is the cost of the sequence the better is the scheduling. At each bit (species) is assigned a fitness value proportional to the decrease of the function (2.38) computed for the sequence with that bit flipped (i.e., mutated from 1 to 0 or vice versa). Then, each bit is ranked, such that: to the one with the least fitness is assigned rank 1, while to the one with the best fitness rank N. Subsequently, a new sequence is generated by flipping a bit chosen according the probability law:

$$P(k) \approx k^{-\tau}, 1 \leq k \leq N \tag{2.40}$$

where τ is a positive setting parameter.

A candidate solution in our GEO approach is a sequence S (assessed by (2.38)), composed of $(M \cdot T)$ bits, as defined in (2.39). An example of the GEO encoding consists of N design variables of 6 bits. Each bit is considered as a species [62]. In this example, M=6 components are maintained by N=3 resources in the time horizon T. This iterative process halts after a prefixed number of generation, and it returns the best sequence S_{best} which minimizes the objective function (2.38). The proposed procedure is described by the following pseudo-code:

1. Initialize a bit sequence S (with size $M \cdot T$) randomly and evaluate the objective function C (as in (2.38));
2. Set: $S_{best} = S$ and $C_{best} = C(S)$;
3. For each generation:
   (a) For each bit i of S:

- Change the bit i (from 1 to 0, or vice versa) and evaluate the cost $C(S_i)$(as in (2.38))for S_i;
- Assess the fitness of bit i as $\Delta C(S_i) = C(S_i) - C_{best}$
- Restore the bit i to its previous value.

(b) Sort $\Delta C(S_i)$ in ascending way;

(c) Choose the bit to change with probability (2.40);

(d) Set $S = S_i$ and $C = C(S_i)$;

(e) If $C < C_{best}$ then set $C_{best} = C$, and $S_{best} = S$;

4. Return S_{best} and C_{best}.

As regard to the traditional evolutionary algorithms (GA, SA and so on), the present procedure has twofold advantages: (i) there is only one adjustable parameter τ, by simplifying the setting, and (ii) the entire evolution is made on one configuration solution S at the time, unlike the traditional evolutionary population-based algorithms, with lower computational costs and a better memory management.

Chapter 3

Numerical case studies

In this chapter, the numerical case studies for the proposed methods, together with their results, are presented. In particular, the main design solutions related to the virtual flow meter and to the transducer calibration function are characterized in 3.1. The results of the metrological analysis of the transducer, assessing the effect of the main uncertainty sources on its metrological performance, are presented and discussed in 3.1.4. Furthermore, a numerical characterization of the proposed fault detection method for the AMB is illustrated in 3.2. Finally, in section 3.3, efficiency and accuracy performance of the decentralized diagnostic procedure is highlighted by a simulation case studies related to the diagnostics of the cold box for the cryogenic system of the Large Hadron Collider at CERN.

3.1 ADVANCED MONITORING: transducer design

In this section, the *virtual flow meter characterization* (3.1) is reported. In particular, the *transducer calibration function* (3.1.2), the *valve model validation* (3.1.3), and the transducer *uncertainty analysis* results (3.1.4) are detailed.

3.1.1 Virtual flow meter characterization

The models Samson and Sereg-Schlumberger were characterized initially at CERN [127] only under certain conditions (fixed pressure drop and temperature). In the following, the behaviour of the methods is investigated by simulation, by avoiding superfluid and two-phase states (liquid-gas), for a temperature range from 3.5 to 295 K and for different pressure drops from 0.00 to 2.48 bar is investigated by simulation. Once the valve parameters $K_{v_{max}}$ and R are defined, the mass flow is calculated for both the helium *gas* and *liquid* phases.

For the *gas* phase, as an example, in Fig. 3.1, the gas mass flow calculated by both the Samson and Sereg-Schlumbeger methods and the (2.3) (reverse sizing valve problem, IEC 60534-2-1 [112]) are reported for a temperature range between 15 and 295 K and for a variable pressure drop. In Fig. 3.2, the methods are compared for a fixed temperature of 270 K at different pressure drop values. In Figs. 3.1 and 3.2, it is possible to notice that the Samson method, compared to the standard IEC 60534, overestimate the mass flow for small pressure drops, while the Sereg-Schlumbeger method overestimate the mass flow for high pressure drops.

For the *liquid* phase, eqs. (2.6) and (2.13) are expressed analogously for both the Samson and Sereg-Schlumberger methods:

$$\dot{m}_{liquid} = const \cdot \sqrt{\rho \cdot (p_{in} - p_{out})} \tag{3.1}$$

provided that the value of *const* is different. For this reason, a difference in the calculated flow much lower than in the gasified phase is achieved.

Such as usual in metrology, the quality of the proposed transducer has been assessed with respect to a certified reference (metrological traceability). In this case, the standard IEC 60534 is assumed as a widely-shared reference in order to assess the performance of the proposed transducer conventionally. In particular, the methods' performance is compared by assessing the percentage difference vs the reference of the standard IEC 60534-2-1:

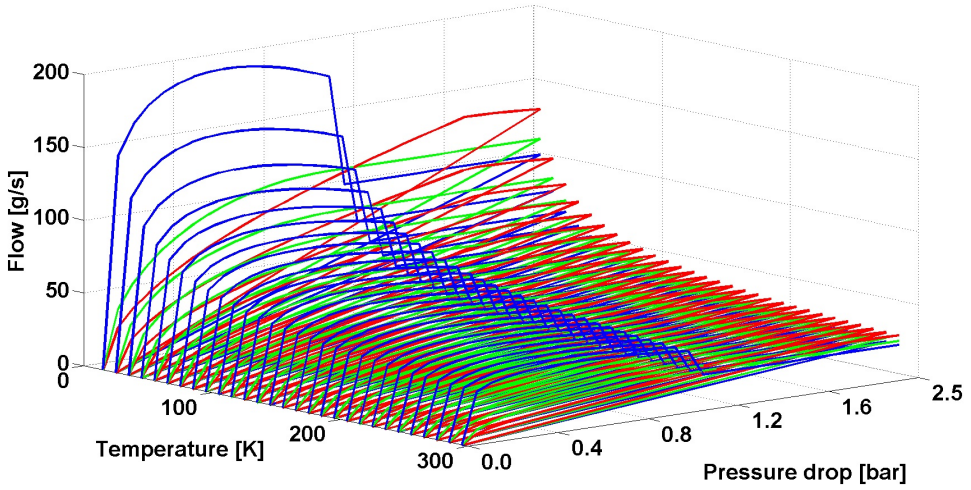

Figure 3.1: Gas helium mass flow vs. temperature and pressure drop by Samson (blue line), Sereg-Schlumbeger (red), and IEC 60534 (green).

$$e_{Sam} = \frac{|\dot{m}_{Sam} - \dot{m}_{IEC}|}{\dot{m}_{IEC}} \cdot 100 \tag{3.2}$$

$$e_{Ser} = \frac{|\dot{m}_{Ser} - \dot{m}_{IEC}|}{\dot{m}_{IEC}} \cdot 100 \tag{3.3}$$

In the gas helium phase, mean percentage errors of 66.7 % and 16.4 % were observed, for the Samson and the Sereg-Schlumberger method, respectively. For liquid helium, as already pre-announced, the mean percentage error is much lower: 0.09 % for Samson and 1.00 % for Sereg-Schlumberger.

The direct use of the IEC approach to predict the flow needs for the knowledge of some physical information about the valve and the pipes under test. Such information could turn out hard to find, especially in old installations. Conversely, Samson and Sereg-Schlumberger models do not require the a-priori knowledge of these physical parameters, and therefore they are considered as more generally applicable.

In synthesis, for the virtual flow meter design, the Samson method, for the helium liquid phase, performs better than the Sereg-Schlumberger; conversely, for the gaseous phase.

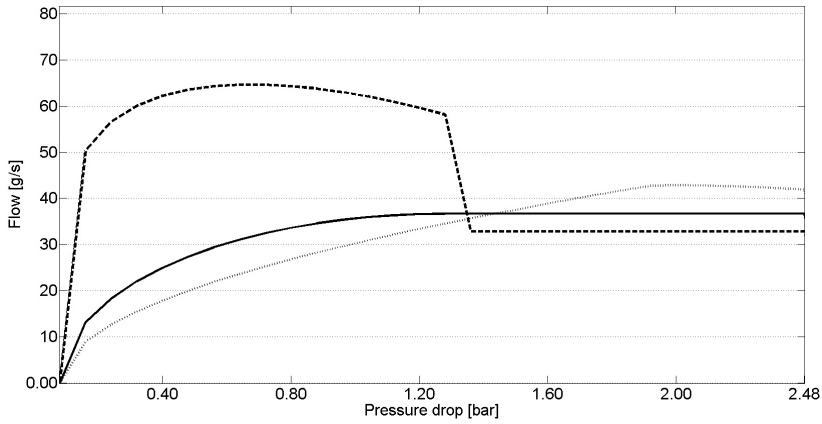

Figure 3.2: Gas helium mass flow vs. pressure drop by Samson (dashed line), Sereg-Schlumbeger (dotted), and IEC 60534 (continuous).

3.1.2 Transducer calibration function

Another important point of the design is the definition of the calibration function of the transducer. This function expresses analytically the inverse model of the measurement process (calibration model) by relating the transducer output (measured flow $\dot{m}_{meas}$) to the measurand (reference flow $\dot{m}_{ref}$). The data trends in Fig. 2.2 point out a nonlinear relationship between valve opening and flow rate. Furthermore, thermodynamic constraints on the process lead to approximate the valve characteristic as piece-wise linear. For this reason, in the transducer calibration, a classical segmented linear regression [128] is exploited. For each *i-th* segment, the relation between reference and measured flow is expressed as:

$$\dot{m}_{ref} = \beta_i \cdot \dot{m}_{meas} + \epsilon_i \tag{3.4}$$

In particular, using the Ordinary Least Square (OLS) regression, the coefficients array $\theta = [\beta; \epsilon]$ is calculated as:

$$\theta = (M_{meas}^T M_{meas})^{-1} M_{meas}^T M_{ref} \tag{3.5}$$

where M_{meas} and M_{ref} represents the array of $\dot{m}_{meas}$ and $\dot{m}_{ref}$, respectively.

The approach of fitting the "valve opening curves" (namely, flow vs. opening) was not adopted, but conversely the flow is fitted as a function of time, in order to have a model including all the effects as a whole. Moreover, the flow is dependent also on the opening and thus this aspect is considered also.

3.1.3 Valve model validation

In the simulation, the helium mass flow $\dot{m}_{ref}$, the fluid temperature (at the inlet T'_{in} and the outlet T'_{out} of the valve), and the valve outlet pressure p'_{out} were input to the model by obtaining as output the inlet valve pressure p_{sim}. Such a simulated result was compared with the actual pressure p'_{in}, measured at the inlet of an actual valve on a hot-gas line of the Long Station by a sensor by WIKA[129]. In particular, the percentage difference between simulated p_{sim} and measured pressure p'_{in} was assessed:

$$error_{\%} = \frac{|p_{sim} - p'_{in}|}{p'_{in}} \cdot 100 \tag{3.6}$$

A set of 21 measurements were performed at the valve inlet with an opening range between 50 and 80 %. In Fig. 3.3, the percentage error vs the valve opening (%) is presented.

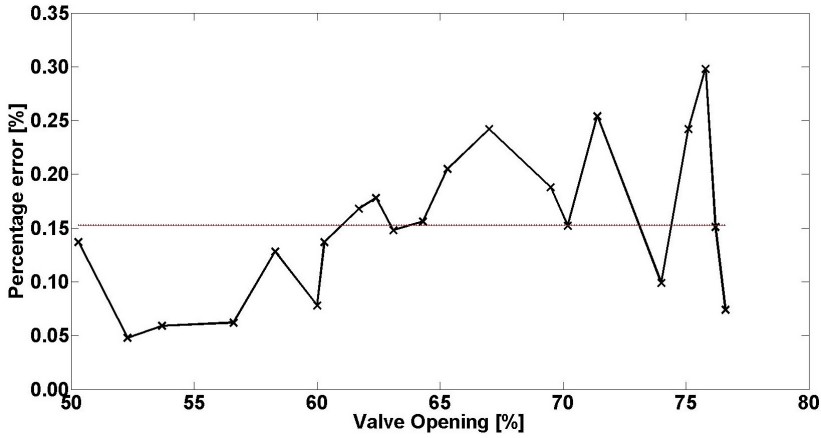

Figure 3.3: Percentage error of the valve model vs opening (dotted line: average).

The mean percentage error is equal to 0.15 %, and for this reason, the use of a simulated valve for the uncertainty analysis was considered as an acceptable assumption.

3.1.4 Uncertainty analysis

The uncertainty analysis of the transducer is carried out according to a *sensitivity analysis* approach [130]: the parameters expressing the uncertainty sources are varied

inside their typical tolerance interval. aimed at computing the metrological performance η, as well as its components of uncertainty σ_e (random error) and deterministic error $\bar{e}$, over the operating domain D=*(l,* $p_{in}, T_{in}, p_{out}, T_{out}, \dot{m}, u_T, u_p, u_\rho, u_\gamma, u_l, u_{model}$*)*:

- in different *setting configurations* of valve opening l,
- at varying the *operating conditions* of input and output pressure and temperature p_{in}, T_{in}, and p_{out} T_{out}, respectively,
- over the *measurand* input range of mass flow $\dot{m}$ as a whole,
- under the action of the above mentioned *uncertainty sources* $\boldsymbol{u} = (u_T, u_p, u_\rho, u_\gamma, u_l, u_{model})$, namely arising from direct measurement uncertainty of the pressure and temperature sensors, nonideal valve opening, actual helium behavior, and uncertainity of the virtual flow-meter.

Then, on this basis, the significance of the impact of each uncertainty source on the metrological performance has to be assessed. Finally, the impact on the metrological performance is to be ranked in order to classify the importance of the uncertainty sources for the transducer operation.

In the following, the main steps of the uncertainty analysis, namely *the metrological performance assessment*, *the uncertainity source significance*, and *the uncertainty ranking*, are described.

Metrological performance assessment

An important point of the uncertainty analysis is assuring a comprehensive investigation of the transducers operating domain D=*(l,* $p_{in}, T_{in}, p_{out}, T_{out}, \dot{m}, u_T, u_p, u_\rho, u_\gamma, u_l, u_{model}$*)* with a reduced operative burden.

In [26, 25], a method for determining the optimum set of experiments, in terms of subspace points of the operating domain D and minimum number of tests, for performing the desired analysis within a prefixed significance is defined. This is a well-known approach of design of experiments, mainly based on the basic idea of exploring only the points related to the desired information.

According to this approach, D has been sampled through two different and combined ("nested") schemes (Fig. 3.4) defined according to the parameters typology.

As a matter of fact, D includes 4 subdomains related to the measurand input range, the settings, the operating conditions, and the uncertainty. At the sampling aim, these subdomains have been grouped in two typologies, related to inner and outer model working: (i) settings and uncertainty, and (ii) measurand input range

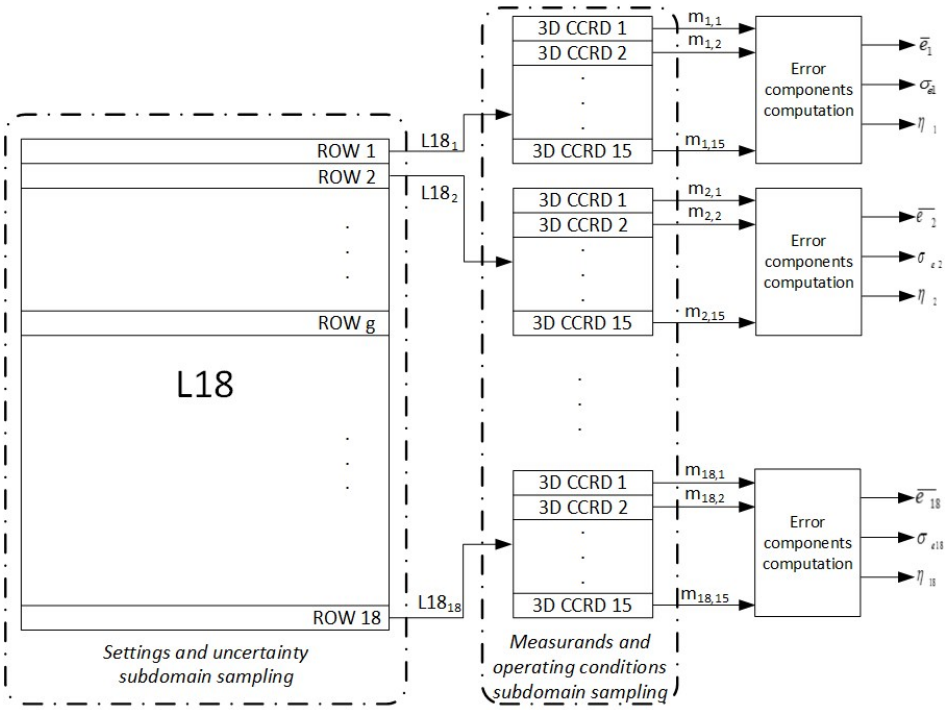

Figure 3.4: Nested procedure for sampling the operating domain $D = (l, p_{in}, T_{in}, p_{out}, T_{out}, \dot{m}, u_T, u_p, u_\rho, u_\gamma, u_l, u_{model})$ of the virtual flow-meter-based transducer and computing the metrological performance components of uncertainty σ_e (random error) and deterministic error $\bar{e}$

and operating conditions.

1. Sampling setting and uncertainty subdomains

For the first subdomain of settings and uncertainty parameters, the optimum sampling subset is determined according to: *(i)* the number of values to be investigated for each parameter, and *(i)* the desired level of knowledge about the parameters covariance (usually referred to as *resolution* [26]). For appreciating at least the curvature of each interval of the setting and uncertainty parameters, three levels were selected (Tab.3.1). In particular, for the valve aperture setting, three equally spaced values of l have been considered from 50 % to 100 %. For the uncertainty parameters, the sensitivity analysis approach yields to consider, for the *i-th* parameter, the nominal value x_{nom} plus/minus the uncertainty band u_i: $(x_{nom} - u_i), x_{nom}, (x_{nom} + u_i)$. In synthesis, this yields to a total of seven 3-levels discrete parameters, one for the settings and six for the uncertainty sources.

On this basis, a standard Taguchi plan L18 [119] is adopted for its capability of investigating combinatorial spaces generated by up to seven 3-levels and one 2-level discrete parameters.

Table 3.1: Levels of setting and uncertainty parameters (in p.u.).

Parameter	**Level**		
	1	2	3
l	0.50	0.75	1.00
u_T	-0.001	0.000	0.001
u_p	-0.001	0.000	0.001
u_l	-0.01	0.000	0.01
u_γ	-0.03	0.00	0.03
u_ρ	-0.005	0.000	0.005
u_{model}	-0.045	0.000	0.045

2. Measurand input range and operating conditions subdomain sampling

The measurand input range and operating conditions subspace is discretized uniformly by means of the strategy 3D Central Composite Rotatable Design (3D CCRD) [120]. Originally conceived for surface-response techniques [119], CCRD turned out to be efficient to explore large multidimensional domains for pointing out most of the desired information. According to this sampling scheme, the points in the 3D subdomain

$SD(\dot{m}, T_{in}, p_{in})$ are disposed symmetrically by concentric rings (Fig. 3.5). The re-

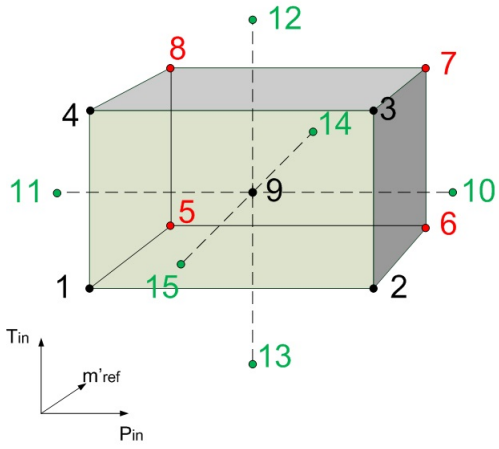

Figure 3.5: 3D CCRD experimental plan for sampling the subdomain of measurand $\dot{m}$ and operating conditions T_{in},p_{in}

sulting sampled points are reported in Tab.3.2. Each point corresponds to a specific

Table 3.2: Values of measurand $\dot{m}$ and operating conditions T_{in},p_{in} sampled according to 3D-CCRD.

Mass flow [g/s]	**Pressure [kPa]**	**Temperature [K]**
0.00	100	100.0
2.98	595	166.4
5.00	1000	211.5
7.98	1595	277.9
10.00	2000	323.0

combination of measurand and operating conditions values: As an example, the point 3 in Fig. 3.5 determines the test configuration characterized by 5 g/s, 1000 kPa, and 211.5 ^oC.

3. Error components computation

The final nested test procedure consists of the following steps:

a) A specific configuration of setting and uncertainty parameters (indicated as $L18_g$, with g=1,..,18, in Fig. 3.4) is set for the g^{th} row of the matrix L18;

b) Once determined the g^{th} test configuration, the mass flows $\dot{m}_{g,r}$, with r=1,.., 15, measured by the virtual flowmeter-based transducer in the measurand and operating conditions parameters subset defined by the 3D-CCRD, is determined by means of the uncertainty model of Fig. 2.3;

c) The set of differences e_r, with r=1,.., 15, between measured and reference mass flows, is computed;

d) A corresponding estimate of the metrological performance factors, $\bar{e_g}$, σ_{eg}, and η_g is achieved.

e) Steps from a) to d) are repeated until all the rows of L18 matrix have been considered, and a set of 18 values of $\bar{e}$, σ_e, and η is obtained.

The results of the metrological performance factors $\bar{e}$, σ_e, and η are reported in Tab.3.3.

Uncertainity source significance

The significance of the influence of an uncertainty source on the metrological performance is evaluated through the analysis of variance (ANOVA). In particular, the model uncertainty is assessed as the error variance:

$$\sum_{g=1}^{M} \epsilon_g^2 = \sum_{g=1}^{M} P_g^2 - M \cdot m_P^2 - \sum_{i=1}^{n_q+n_z} \sum_{j=1}^{n_r} n_{ij} \cdot (m_{ij} - m_P)^2 \tag{3.7}$$

where ϵ_g is the error computed for the g^{th} test configuration; M is the number of the experiments (in this case 18); P_g is the generic metrological performance factor at the g^{th} test configuration; m_P is the average of the performance factor considering all the L18 matrix rows; n_q is the number of uncertainty sources; n_z is the number of setting configurations; n_r is the number of parameters levels; n_{ij} the repetition number, i.e. the times the i^{th} parameter is set at j^{th} level; and finally m_{ij} is the average of the performance computed with the i^{th} parameter at the j^{th} level.

The *variance ratio* F_i (usually referred to also as F-statistic [120]) has been computed as the ratio between the variance due to the i^{th} uncertainty source and the variance of the model error:

$$F_i = \frac{\sigma_i^2}{\sigma_\epsilon^2} \tag{3.8}$$

The significance of an uncertainty source is evaluated by means of a Fisher-Snedecor statistical test with a confidence level of 70%. This relevant level of α

Table 3.3: Results for the metrological performance η and its components of uncertainty σ_e (random error) and deterministic error $\bar{e}$.

Trial	η	$\bar{e}$	σ_e
1	10.093	-3.527	9.789
2	9.403	0.929	9.685
3	11.109	5.401	10.048
4	9.146	5.213	7.779
5	20.626	1.501	21.293
6	15.922	-3.275	16.128
7	13.443	2.145	13.737
8	30.610	2.223	31.601
9	10.295	-2.618	10.306
10	9.989	-3.331	9.748
11	9.487	1.214	9.739
12	10.440	4.919	9.532
13	8.441	0.417	8.727
14	6.250	3.769	5.162
15	8.173	-4.204	7.255
16	21.098	0.562	21.831
17	15.491	3.129	15.705
18	13.907	-4.714	13.543

allows all the uncertainty sources having a relevance at least double than the analysis error ($F_i \geq 2$) to be highlighted.

The corresponding results for $\bar{e}$, σ_e and η are shown in Tab. 3.4, 4.4 and 3.6, respectively. (For the sake of completeness also the action of the valve openings l is assessed.) In particular, each table provides: *(i)* the sum of the squares **SS**, *(ii)* the related degrees of freedom **DF**, *(iii)* the contribution **MS** of the parameter to the overall variance, assessed as the ratio between the corresponding **SS** and **DF**, and *(iv)* the variance ratio F_i related to the i^{th} uncertainty source.

The following results are achieved:

- the setting of valve opening l do not have a significant influence on the deterministic error $\bar{e}$, but on σ_e and, consequently, also on the metrological performance η;

Table 3.4: ANOVA results for $\bar{e}$.

	SS	**DF**	**MS**	F_i
l	1.991	2	0.9954	0.91
$u(T)$	25.598	2	12.799	11.73
$u(P)$	4.088	2	2.0442	1.87
$u(l)$	16.794	2	8.397	7.7
$u(\gamma)$	4.627	2	2.3137	2.12
$u(\rho)$	17.65	2	8.8248	8.09
u_{model}	120.864	2	60.4318	55.38
Error	3.273	3	1.0911	

Table 3.5: ANOVA results for σ_e.

	SS	**DF**	**MS**	F_i
l	222.922	2	111.461	3.34
$u(T)$	65.783	2	32.892	0.99
$u(P)$	96.14	2	48.07	1.44
$u(l)$	32.438	2	16.219	0.49
$u(\gamma)$	114.83	2	57.415	1.72
$u(\rho)$	7.148	2	3.574	0.11
u_{model}	81.619	2	40.809	1.22
Error	99.975	3	33.325	

- all the uncertainty sources have significant influence on the deterministic error $\bar{e}$, but no one on σ_e, and consequently not even on η.

These results confirm, at a relevant level of α (30%), the quality of the metrological design of the current transducer release.

Discussion

The sources impact was ranked according to their capability of influencing the performance assessed by F_i. For the sake of completeness, all the sources were considered (again with the valve opening l), independently on their absolute significance, in order to have a deeper insight on the uncertainty of the transducer, as well as indications for further improvements. At this aim, only a relative 5% of the cumulative distribution of F_i was neglected, by considering the first 95% as interesting.

Table 3.6: ANOVA results for η.

	SS	**DF**	**MS**	F_i
l	185.878	2	92.9388	3.12
$u(T)$	48.723	2	24.3615	0.82
$u(P)$	87.637	2	43.8184	1.47
$u(l)$	33.589	2	16.7943	0.56
$u(\gamma)$	94.260	2	47.1301	1.58
$u(\rho)$	8.976	2	4.4881	0.15
u_{model}	65.874	2	32.9371	1.11
Error	89.416	3	29.8052	

For the deterministic error $\bar{e}$, the histogram of Fig. 3.6 (*Pareto diagram*[120]) highlights that the uncertainty affecting the Sereg model is the most influencing source, followed in order by the temperature sensor, the valve opening, and the Helium density.

For the transducer uncertainty σ_e and the overall metrological performance η, the impact is more leveled (the uncertainty sources have no impact), and only the valve opening plays a mayor role, owing to its capability of *"modulating"* the uncertainty impact (Fig. 3.7).

The results of the metrological analysis highlight the quality of the metrological design of the current transducer release. Furthermore, the possibility of exploiting cheap pressure sensors is pointed out: sensors with 0.1% relative uncertainty turned out to be uselessly outperforming. Conversely, the uncertainties characterizing the temperature and pressure measurement, the valve opening, the helium density heat capacity and the flowmeter model produce a deterministic error on the mass flow measurement to be corrected.

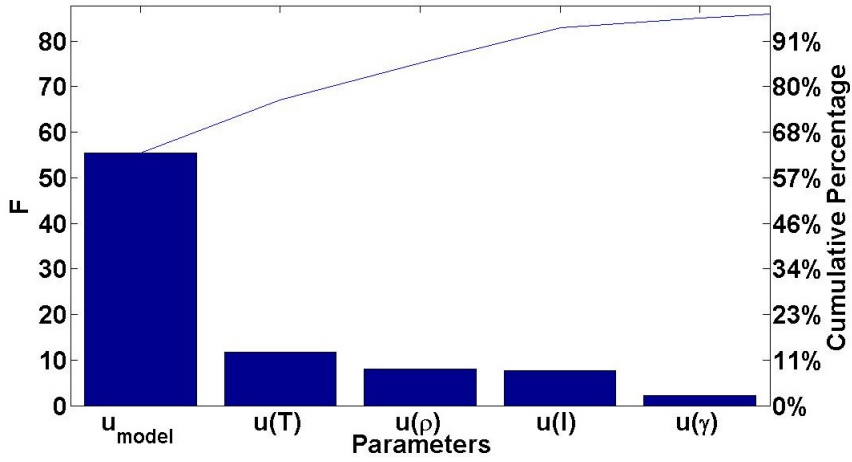

Figure 3.6: Ranking of uncertainty source impact on the transducer deterministic error $\bar{e}$

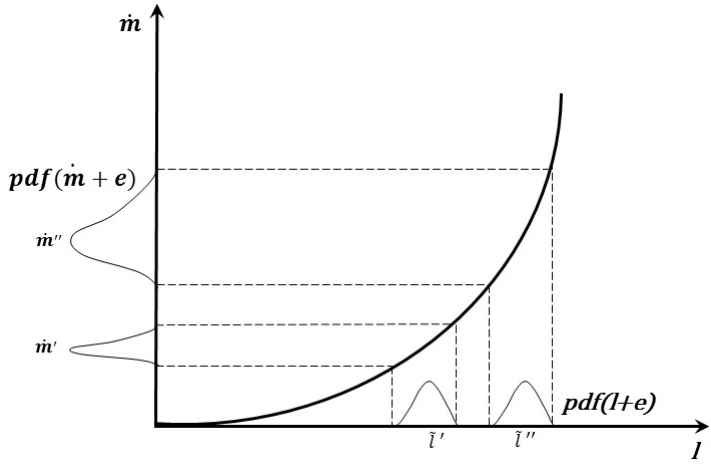

Figure 3.7: Effect of the function slope for the equal percentage valve on the uncertainty propagation of the source u_l on $u_{\dot{m}}$

3.2 FAULT DETECTION: characterization of the proposed method

The proposed method of fault detection was characterized in simulation, in order to verify its capability of estimating the noise power and its variance, as well as to

identify the faulty condition with a certain false alarm rate. In particular, for *noise power estimation*, starting from a record of measurements, obtained from the nominal condition, the model was identified and its frequency response evaluated. Then, the frequency response magnitude was corrupted by white Gaussian noise with null mean and variance equal to 1.0×10^{-4}. The proposed method for estimating the noise power and its variance was executed on 10 000 simulation trials in the GNU/Octave environment. Finally, for each trial, the noise power and its variance were estimated.

In Fig. 3.8, the normalized histogram of the estimated values of noise power is reported, together with the Gaussian probability density function (pdf). It was evaluated with *(i)* a mean value equal to the average of the estimated noise power values, and *(ii)* a variance equal to the average of the estimated variances. The figure highlights a significant agreement between the experimental histogram and the Gaussian pdf, assessed by a chi-square test, for a significance level of 1×10^{-3}.

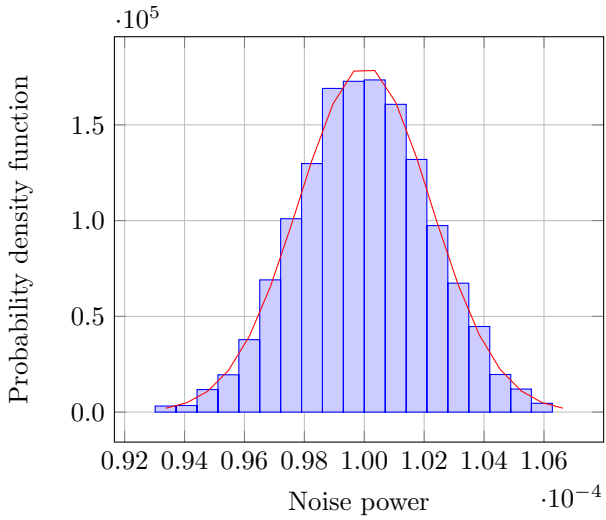

Figure 3.8: Normalized histogram of the estimated values of noise power (blue bars) and Gaussian probability density function (red line), having mean equal to the average of the estimated noise powers, and variance equal to the average of the estimated variances.

Further simulations were carried out to verify the fault detection performance in terms of false alarms. In this case, 10 000 couples of reference and under-test records were generated. The records obtained by the model were corrupted by white Gaussian noise with null mean and variance equal to 1.0×10^{-4}. In this way, an unfaulty system was emulated by assessing the false alarm rate.

In Fig. 3.9, the results of such simulations are shown. In the figure, the histogram

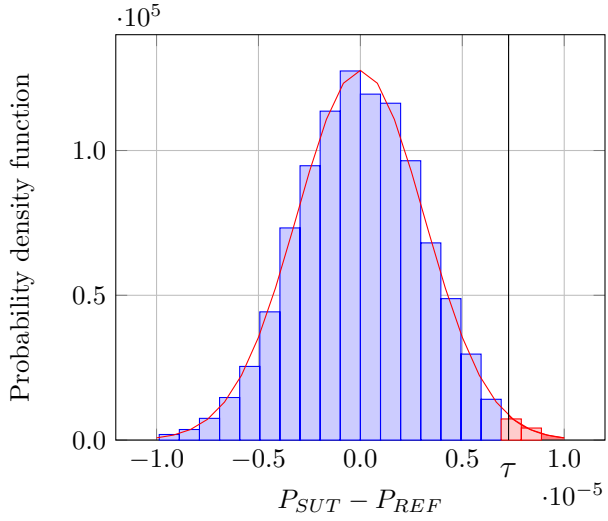

Figure 3.9: Normalized histogram of $P_{SUT} - P_{REF}$ (blue) and Gaussian probability density function, evaluated with a mean value equal to 0 and a variance equal to twice the average of the estimated variance of P_{REF} (red line). The black line highlights the threshold τ, corresponding to a $P_{fa} = 0.01$.

of the measured $P_{SUT} - P_{REF}$ has been reported, together with the Gaussian pdf, having null mean and variance equal to twice the average of the estimated values of the variance of P_{REF}. Even in this case, the figure highlights a not significant difference between the experimental data and the Gaussian distribution, for a significance level of 1×10^{-3}, assessed by a chi square test.

As mentioned in Sec. 2.2.4, the threshold τ can be chosen such to have a certain probability of false alarm. In this case, by fixing the probability of false alarm $P_{fa} = 0.01$, and substituting it in (2.35), a value of τ equal to 7.27×10^{-4} is found. A black line corresponding to such value has been reported in the figure. With this value of the threshold, it has been obtained from the simulations a false alarm rate of 0.0103, which is very close to the imposed value of P_{fa}.

3.3 FAULT DIAGNOSIS: LHC cryogenics diagnostics developments

The dMGA proposed in the previous chapter was applied at CERN to a first case study for analyzing possible future developments in the cryogenic equipment for 1.8 K refrigeration units. The cooling capacity below 2.0 K for the superconducting magnets of the Large Hadron Collider is provided by 8 refrigeration units of 2.4 kW by IHI-Linde and Air Liquide.

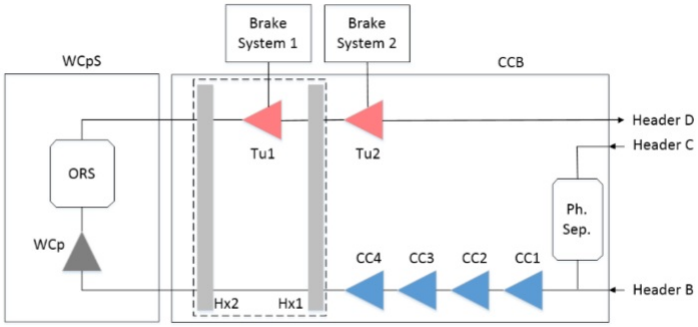

Figure 3.10: Architecture of the 1.8 K refrigeration unit by IHI-Linde.

This case study is devoted to the diagnostics of one refrigeration unit by IHI-Linde composed by (Fig. 3.10) [131]: *(i)* a warm compression station (WCpS), including an oil lubricated screw compressor (WCp), with the associated oil removal system (ORS); *(ii)* a cold compressor box (CCB), including mainly a train of cold compressors (CC1-4), 2 heat exchangers (Hx1-2), a phase separator (Ph. Sep.), and 2 turboexpanders (Tu1-2); *(iii)* the interfaces with the LHC (header B); and *(iv)* a 4.5 K refrigerator (headers C and D).

3.3.1 Diagnostics problem

In the current situation at CERN, the refrigeration unit is handled by a monitoring and control system. Several sensors are linked to the PLCs, used to control the devices and to send the measured values to the general CERN monitoring system. This simulation case study is aimed at assessing the performance of a future advanced diagnostic function to be integrated in the monitoring system to support the

operators [132]. Most critical devices in the refrigeration unit are: (i) in the warm compression station, the oil removal system, and (ii) in the cold compressor box, the compressors CC1-4 and the cryogenic turbines Tu1-2. The WCp is a screw compressor, using a particular oil (Breox) to increase the tightness of the entire process. Before sending the compressed helium to the cold compressor box, all the possible traces of oil have to be removed up to a residual of only few ppb. The cold compressors installed in the box are critical because they are complex systems relying on active magnetic bearings for shaft levitation. Particular attention must be paid also to the cryogenic turbines, because they cannot correctly run in presence of impurities in the helium flow (Breox, water or nitrogen). Furthermore, it is important to properly regulate the break system, aimed at dissipating the mechanical energy produced by the expansion process.

The distributed diagnostic system (Fig. 3.11) was conceived to carry out the diagnostic task locally. The achieved diagnosis response is sent to the CERN monitoring system (acting as Remote Supervision Station), while the PLCs are still used for the control process.

3.3.2 dMGA configuration

For this case study, dMGA instances, logically connected in a stepping-stone bidirectional ring topology, were realized. The dMGA was implemented in language C and was executed on 3 virtual machines (64 bit architecture, 2 cores, 2GB RAM). The Linux library Message Passing Interface was used for passing messages by Secure Shell protocol between the machines.

The following parameters configuration was used: number of machines: 3; number of runs: 10; population size: 15; migration rate: 10; crossover probability: 0.8; mutation probability: 0.05; maximum number of generations: 100; and maximum number of micro-generations: 10. A centralized brute force algorithm was also implemented in MATLAB and executed on a pc with i7 processor (3.40 GHz) with 8 GB RAM. This algorithm consists of systematically enumerating all the candidates for the solution and searching for the maximum likelihood.

3.3.3 Proof-of-principle scenario

The anomalies and faults vectors (Tables 3.7 and 3.8, respectively), compiled according to the plant engineer's experience and requirements, include 80 anomalies and 55 faults. In these tables, low pressure side and high pressure sides are respectively

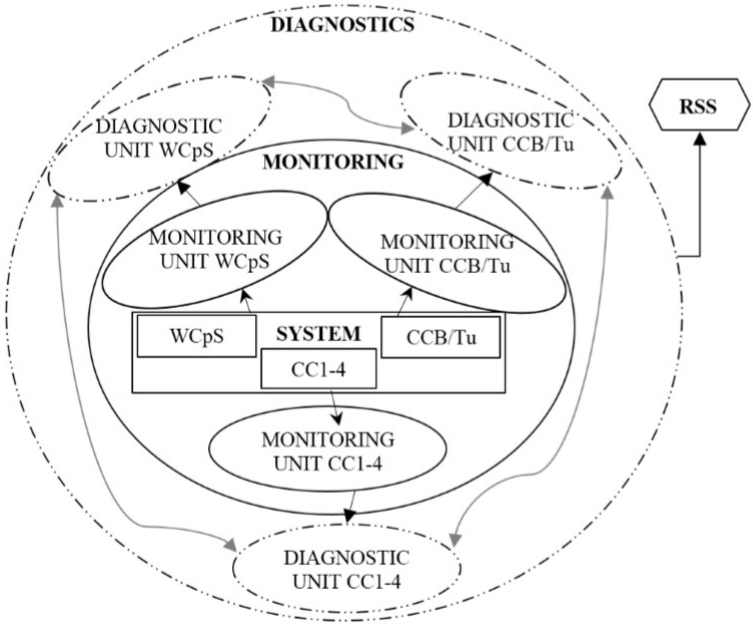

Figure 3.11: Architecture of distributed monitoring and multiple-fault diagnostics proposed for LHC cryogenics at CERN.

indicated as L.P. and H.P.

The a priori probabilities p_j and the causal strengths c_{ij} were identified from a statistical analysis based on engineers and operators knowledge and historical faults. All the faults of Table 3.8 are critical because they definitely lead to system failures (permanent interruptions). An interruption for a single refrigeration unit means a stop for the LHC as a whole. Moreover, also from a technical point of view, this case study is a hard combinatorial optimization problem [41]: 55 faults give rise to 2^{55} possible solutions of the MFD problem. For this reason, it turns out to be intractable with a brute-force algorithm. To give an idea, after 10 days of continuous running, the algorithm was capable to assess only 7.3642×10^9 possible solutions on a total of 3.6029×10^{16}.

According to the literature about evolutionary algorithms [133], main performance indexes are *effectiveness* (a measure of the quality solution within a given computational limit) and *efficiency* (a measure of the amount of computing needed to achieve a satisfactory solution). In this paper, the effectiveness was calculated as the average

Table 3.7: Anomalies vector.

Anomalies			
Water flow low	A1	Bearings currents high CC2	A41
Air pressure low	A2	No sensors signal CC2	A42
Voltage low	A3	Axial force high CC2	A43
Vacuum pressure high	A4	Unbalance level bearing A high CC2	A44
Water contamination	A5	Unbalance level bearing B high CC2	A45
Nitrogen contamination	A6	Motor currents high CC2	A46
Breox contamination	A7	Motor temperature high CC2	A47
Temperature brake circuit Tu1 high	A8	Motor voltages high CC2	A48
Temperature brake circuit Tu2 high	A9	Levitation lost CC3	A49
Pressure brake circuit Tu1 high	A10	Bearings currents high CC3	A50
Pressure brake circuit Tu2 high	A11	No sensors signal CC3	A51
Pressure Tu1 bearings low	A12	Axial force high CC3	A52
Pressure Tu2 bearings low	A13	Unbalance level bearing A high CC3	A53
Temperature Tu1 bearings low	A14	Unbalance level bearing B high CC3	A54
Temperature Tu2 bearings low	A15	Motor currents high CC3	A55
Inlet pressure Tu1 low	A16	Motor temperature high CC3	A56
Inlet pressure Tu2 low	A17	Motor voltages high CC3	A57
Inlet T1 mass flow low	A18	Levitation lost CC4	A58
Overspeed Tu1	A19	Bearings currents high CC4	A59
Overspeed Tu2	A20	No sensors signal CC4	A60
Inlet temperature Tu1 low	A21	Axial force high CC4	A61
Inlet temperature Tu2 low	A22	Unbalance level bearing A high CC4	A62
Out temperature Tu2 low	A23	Unbalance level bearing B high CC4	A63
Inlet cold box mass flow low	A24	Motor currents high CC4	A64
Pressure (L.P.) high	A25	Motor temperature high CC4	A65
Pressure (L.P.) low	A26	Motor voltages high CC4	A66
Pressure (H.P.) high	A27	Helium mass flow low	A67
Pressure (H.P.) low	A28	Pressure (WCS L.P.) high	A68
Dewar helium level high	A29	Pressure (WCS L.P.) low	A69
Inlet pressure CC1 high	A30	Pressure (WCS H.P.) high	A70
Levitation lost CC1	A31	Helium temperature (WCS H.P.) high	A71
Bearings currents high CC1	A32	Oil temperature high	A72
No sensors signal CC1	A33	Oil mass flow low	A73
Axial force high CC1	A34	Compressor vibrations level high	A74
Unbalance level bearing A high CC1	A35	Pump currents high	A75
Unbalance level bearing B high CC1	A36	ΔP on filters high	A76
Motor currents high CC1	A37	Oil contamination on absorber system	A77
Motor temperature high CC1	A38	Motor currents high	A78
Motor voltages high CC1	A39	Bearings temperature high	A79
Levitation lost CC2	A40	Motor temperature high	A80

Table 3.8: Faults vector.

Faults			
Water cooling system fault	F1	Compressor motor faults CC2	F29
Valves air system fault	F2	Controller faults CC3	F30
Power supply system fault	F3	Position sensor failure CC3	F31
Vacuum pumps fault	F4	Magnetic bearing coil fault CC3	F32
Cold box leakage	F5	Compressor shaft faults CC3	F33
Connections leakage	F6	Compressor motor faults CC3	F34
Tu1 inlet valve fault	F7	Controller faults CC4	F35
Filter Tu1 fault	F8	Position sensor failure CC4	F36
Filter Tu2 fault	F9	Magnetic bearing coil fault CC4	F37
Cryostat fault	F10	Compressor shaft faults CC4	F38
Joule Thomson valves fault	F11	Compressor motor faults CC4	F39
Break system 1 fault	F12	Bypass valve failure	F40
Break system 2 fault	F13	Buffer system fault	F41
Helium pollution	F14	Hand valve failure (L.P.)	F42
Gas analyzer fault	F15	Discharge valve failure	F43
Bearing pressure regulator 1 fault	F16	Heat exchanger fault	F44
Bearing pressure regulator 2 fault	F17	Hand valve failure (H.P.)	F45
Dewar level sensor fault	F18	Oil filter faults	F46
Dewar level circuit fault	F19	Circuit leakage	F47
Controller faults CC1	F20	Oil level sensors faults	F48
Position sensor failure CC1	F21	Oil pump faults	F49
Magnetic bearing coil fault CC1	F22	Oil valves faults	F50
Compressor shaft faults CC1	F23	Absorbers filters faults	F51
Compressor motor faults CC1	F24	Compressor bearings faults	F52
Controller faults CC2	F25	Gearbox failures	F53
Position sensor failure CC2	F26	Compressor shaft faults	F54
Magnetic bearing coil fault CC2	F27	Motor faults	F55
Compressor shaft faults CC2	F28		

likelihood of the best in run solutions, while the efficiency as the average of the generations number corresponding to the best likelihood solution.

The dMGA was tested on 4 different cases, consisting of different scenarios up to 5 simultaneous faults: (i) two cases, related to the cold compressors (CC1-4) with magnetic bearings, owing to past reliability problems; and (ii) two related to the warm compression station and to the cold box.

3.3.4 Simulation results

The dMGA was executed to evaluate the best solution in terms of the faults with their occurrence probability. In effectiveness and efficiency tests, the dMGA worked according to configuration described in Sec. 3.3.2. The results for the 10 most significant scenarios are reported in Table 3.9. The anomalies and the faults are encoded as arrays of binary chromosomes, thus, in Table 3.9, the array locations where the bit 1 is present are indicated. The solutions correspond to reasonablefaults. As an example, in test case 2, if the low voltage anomaly (A3) is detected, the power supply system fault (F3) is diagnosed. The average likelihood (3.502×10^{-2}) is quite close to the best one (3.890×10^{-2}) and the average generation's number is reasonable (61). The results of Table 3.9 highlight how the dMGA is capable of reaching the best likelihood solution in a fairly good number of generations and the average likelihood is close to the best likelihood. As an example, in test case 4, the average likelihood is equal to the best likelihood: 3.189×10^{-4}, and the algorithm reaches the best solution in an average generation's number of 56, with a standard deviation of 17, over 10 test repetitions.

Table 3.9: Anomalies and corresponding faults with related likelihood and indexes determined by the dMGA.

Test	**Anomalies**	**Faults**	**Best likelihood**	**AVG likelihood**	**AVG gen. num.**
1	A4	F4	3.890×10^{-2}	$(3.502 \pm 1.167)10^{-2}$	(61 ± 20)
2	A3	F3	3.890×10^{-2}	$(3.516 \pm 1.123)10^{-2}$	(51 ± 15)
3	A5, A6, A7, A12, A13, A19, A20, A21, A22, A23, A30	F10, F14	8.289×10^{-10}	$(7.460 \pm 2.487)10^{-10}$	(64 ± 21)
4	A4, A76, A77	F4, F51	3.189×10^{-4}	$(3.189 \pm 0.000)10^{-4}$	(56 ± 17)
5	A1, A8, A9, A16, A17, A18, A19, A21, A22, A23	F1, F7, F11	9.026×10^{-10}	$(6.494 \pm 3.873)10^{-10}$	(56 ± 18)
6	A34, A35, A36, A49, A50, A51, A64, A65, A66	F23, F31, F39	5.202×10^{-8}	$(4.805 \pm 1.192)10^{-8}$	(64 ± 17)
7	A3, A4, A67, A68, A69, A70, A76, A77	F3, F4, F41, F51	4.139×10^{-9}	$(2.942 \pm 1.829)10^{-9}$	(64 ± 17)
8	A1, A8, A9, A16, A17, A18, A19, A21, A22, A23, A78, A80	F1, F7, F11, F55	1.131×10^{-11}	$(8.065 \pm 4.960)10^{-12}$	(64 ± 17)
9	A4, A64, A65, A66, A67, A68, A69, A70, A73, A74, A75, A76, A77	F4, F39, F41, F49, F51	1.169×10^{-12}	$(8.313 \pm 5.161)10^{-13}$	(69 ± 16)
10	A3, A5, A6, A7, A12, A13, A19, A20, A21, A22, A23, A29, A30, A67, A73	F3, F10, F14, F19, F47	3.300×10^{-15}	$(1.540 \pm 1.226)10^{-15}$	(62 ± 21)

Chapter 4

Experimental case studies

In this chapter, the experimental case studies for the proposed methods, together with their results, are described. All the methods, except for the fault diagnosis technique, were validated on CERN facilities. In particular, the proof of principle of the alternative virtual flow meters for the helium gaseous state, carried out on the test station for superconducting magnets in the test facility SM18, are presented in 4.1. Furthermore, in section 4.2, the experimental results of the fault detection proof-of-principle demonstration for a case study on AMB-based cold compressors of the LHC are reported. In section 4.3, the efficiency and accuracy performance of the dMGA procedure is highlighted by a case study related to diagnosing the main edifices systems (e.g., anti-theft/anti-intrusion, air conditioning, and so on) in remote building automation. Finally, the preventive maintenance experimental results of a case study on the CERN liquid helium storage system are reported in section 4.4.

4.1 ADVANCED MONITORING: proof of principle

A validation case study for the helium gaseous state, carried out at CERN on the test station for superconducting magnets in the laboratory SM18 [134, 135, 136], is reported. The models of Samson and Sereg-Schlumberger were identified and validated experimentally. Predicted and experimental helium mass flows were compared in order to assess the models performance and to validate the design of the helium flow transducer.

In the following, (4.1.1) the *helium flow in long-magnet test bench* of the test facilities SM18, (4.1.2) the *experimental setup*, the *virtual flow meter* (4.1.3) *identification* and (4.1.4) *validation* are illustrated.

4.1.1 Helium flow in long-magnet test bench

The laboratory SM18 [136] is the cryogenic facility where all the main components of LHC were tested before final installation in the tunnel. In particular, the flow meter experiments were carried out in the cryogenics supervisory system of the test station for superconducting magnets in vertical position, called the 'Long Station'.
Figure 4.1 shows the synoptic of the Long Station. The helium flow for the cryostat is controlled by the valves (CV): (i) $CV810$, for the flow of liquid helium inlet; (ii) $CV813$, $CV823$, $CV833$, and $CV843$, for the flow of the outgoing hot gaseous helium from the cryostat; and (iii) $CV812$, for the flow of the cold gaseous helium outlet. Each outgoing hot gaseous helium line has a flow-meter already installed. Conversely, on the liquid inlet and cold gas outlet lines, flow-meters are not installed. Inside the cryostat, a heater varies the helium bath temperature. The flow motion is caused by the pressure differential between the cryostat (shown in Fig. 4.1) and the helium circuit without operating machinery (e.g. pumps).

4.1.2 Experimental setup

The virtual sensor effectiveness was validated by multiple experiments (cross-validation). The valves working conditions, and thereby the helium flow, were measured on the test station of the magnets in a vertical position (Fig. 4.1). The gaseous-state models (2.1.2) underlying the virtual flow-meters were identified, and validated on the control valve lines 813. In the corresponding hot-gas line, also an actual flow-meter transducer by Brooks [137] is installed. This transducer was assumed as a reference

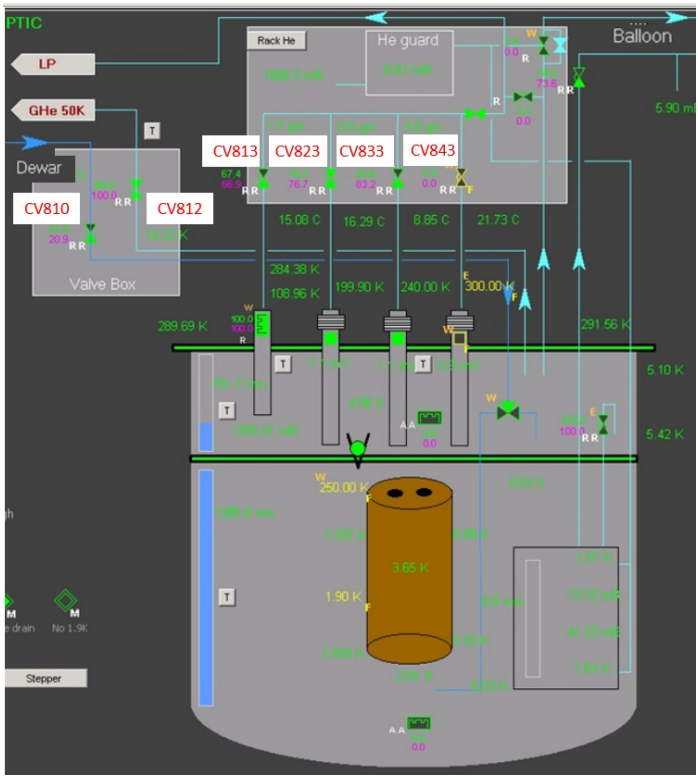

Figure 4.1: Long station synoptic at CERN test facility SM18

for comparing modelled and measured data in all the tests reported in this section. At this aim, both the models were implemented on an equal percentage valve (813, for the flow of the outgoing hot gaseous helium from the cryostat), with a K_{vmax} of 5.8 m^3/h and a rangeability of 1:50. The temperature at the valve inlet and outlet is considered constant, and for this reason, only the inlet temperature was measured (sensor TT813). The valve inlet pressure was measured by the sensor PT820c, while the valve outlet pressure by the PT240. The flow rate was changed by increasing the temperature and opening the valve, at constant pressure, inside the cryostat. The Reynolds numbers observed during the experimental tests are in the range (90, 4275). Looking at the ΔP variations, the flow is in the laminar and in the transient regime. The tests were carried out in a large experimental facility at CERN by setting the flow behaviour as demanded by the cryogenic process need.

4.1.3 Virtual flow meter identification

At CERN, the process variable measurements (pressure, temperature, liquid level, and so on) for monitoring and control purposes are stored in a database. Due to the data size and the high number of sensors, the sampling time of stored data is not uniform. The sampled data are stored either when the sensor input varies significantly or after a suitable prefixed sampling time. On these basis, in the following figures, the samples of the various data sets are fitted to a common time base by the supervision software.

For the identification and validation experiments, after choosing a suitable time window, e.g. 30 minutes, the sensors measurements were remotely extracted from the supervision station database. The helium parameters, i.e. density ρ, and heat capacity (both at constant pressure c_p and constant volume c_v), were then calculated using the software package HePak by Cryodata [138].
The Samson and Sereg-Schlumberger models were implemented in Matlab and the flow was first estimated for gaseous helium.

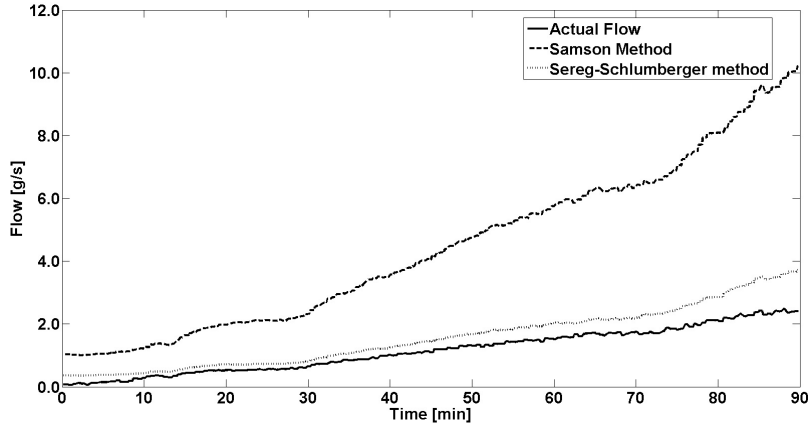

Figure 4.2: Gaseous helium flow through the valve CV813

In Fig. 4.2, as expected, the overall model trends follow the measured flow only qualitatively. As a matter of fact, modelled and actual values have a significant local difference (especially Samson). Therefore, the segmented linear regression (3.4) was applied. The best model identification is achieved by 3 breakpoints, therefore the valve opening range was divided in 4 intervals, and the models were identified piece wise for each of them. Correspondingly, the offset and proportional coefficients β_i and

Table 4.1: Offset and proportional coefficients for Samson and Sereg-Schlumberger models

Coefficient	Valve opening (%)			
	0-33 %	33-46 %	46-70 %	70-100 %
β_{Sam}	5.96	3.72	3.39	2.87
ϵ_{Sam}	-0.29	0.03	0.13	0.44
β_{Ser}	33.6	21.2	17.4	15.7
ϵ_{Ser}	-0.28	0.02	0.21	0.44

ϵ_i were determined (Tab. 4.1), by minimizing the mean square error between measured and modelled values. In particular, for the model identification, the coefficients were computed as averages on 19 independent acquisitions, while the validation is highlighted on a further independent data set.

4.1.4 Virtual flow meter validation

In Fig. 4.3, modeled and experimental flow values are compared for both the modified models. In Fig. 4.4, the percentage error is assessed for both the methods.

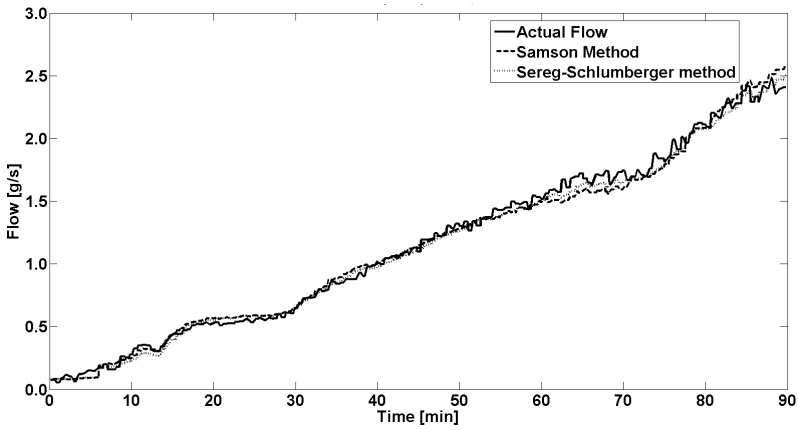

Figure 4.3: Comparison between modified Samson and Sereg modeled and measured flows

The high percentage error fluctuations for the first samples (Fig. 4.4), depends from the low number of the available data used as reference in that opening range. In Figs. 4.5 and 4.6, the calibration functions (predicted and measured flow) are presented for both the modified Samson and Sereg methods, respectively. The red line

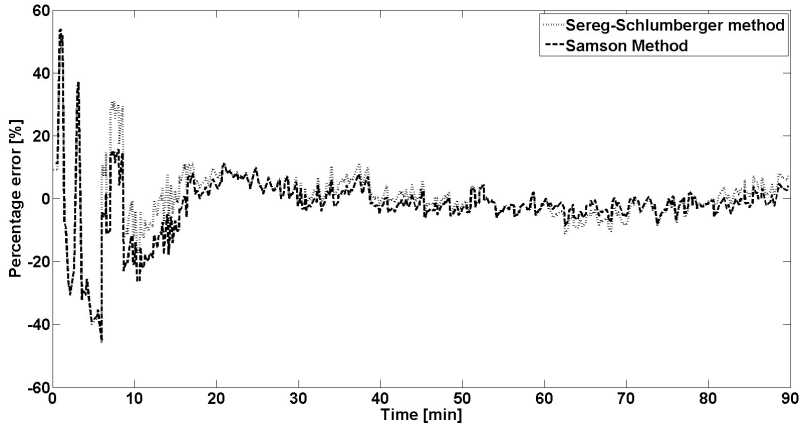

Figure 4.4: Samson and Sereg models percentage errors

represents the ideal condition where the models have null error (i.e. ideal prediction). The model predicts how the various parameters interplay (i.e. pressure drop, valve opening, temperature); while the reference data might not cover the parameter space as a whole. In Tab. 4.2, the percentage root-mean-square error (RMSE), and the mean percentage error ($e_r\%$) are assessed for both the model. However, both the models underestimate the actual flow; specifically, the Sereg-Schlumberger performs better than the Samson model.

Table 4.2: Models errors summary

Models	RMSE %	e_r %
Samson	7.50	-8.75
Sereg-Schlumberger	7.00	-4.45

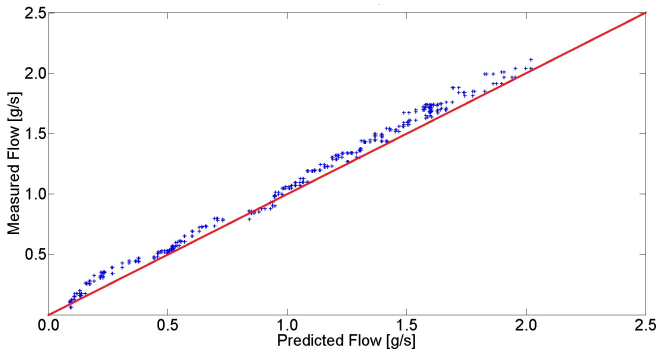

Figure 4.5: Transducer calibration function version based on Samson model

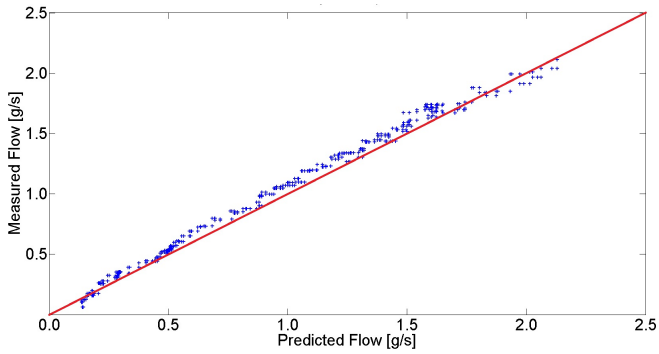

Figure 4.6: Transducer calibration function version based on Sereg-Schlumberger model

4.2 FAULT DETECTION: proof of principle

An experimental analysis has been carried out on 4 cold compressors at CERN, in order to verify the method capability of detecting faults in actual cases. Records have therefore acquired on all the compressors both in unfaulty conditions and during maintenance tests.

4.2.1 Case study

In 1998, the industrial procurement of the eight 1.9 K refrigeration units for the LHC sectors was launched and the contracts were adjudicated to Air Liquide (France) and a consortium of IHI (Japan) and Linde Kryotechnik (Switzerland) for the delivery

and installation of four units each [27].

During the first LHC run, the IHI-Linde system presented some problems in terms of reliability. In particular, the cold compressors were identified as the cause of several process interruptions. The general purpose technique described in Section 2.2.4, is devoted in this paper, to the fault detection for cold compressors installed in the IHI-Linde refrigeration unit. In this cold box, four AMB cold compressors stages are installed. A generic rotating machinery with active magnetic bearing (Fig.4.7[139]) is composed by: position sensors; a controller unit necessary to stabilize the suspense state of the rotor; power amplifiers; actuators (radial and axial bearings) responsible for rotor levitation, and, finally, the rotating machinery rotor and impeller.

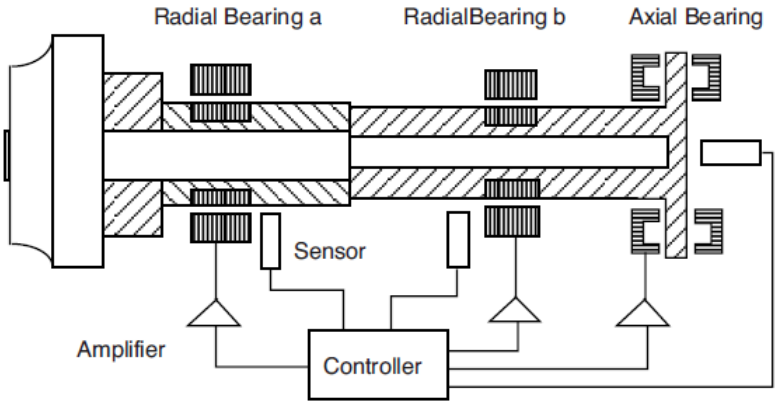

Figure 4.7: Active magnetic bearing system architecture.[139]

The four cold compressor systems under test, have two radial bearings and one axial bearing; 2 pulse sensors; 10 position sensors; 10 power amplifiers and a controller board. The power amplifiers and the controller board are included in one external module provided by MECOS [140]. To control the rotational speed, a three-phases induction motor, together with a variable frequency driver, is used. As already aforementioned, active magnetic bearings systems allow to perform several measurements without additional devices or sensors. Time-domain signals (shaft position and bearing excitation current) and frequency-domain signals (controller sensitivity and the FRF) can be acquired. In particular, for the proposed fault detection technique, the system FRF is measured.

4.2.2 Measurements setup

During the LHC Long-Shutdown 1 (LS1) some tests on the IHI-Linde cold box were performed. The necessity of these tests arise from the fact that a new hardware setup (new cables configuration, new MECOS controller unit, etc.) was settled in the framework of the radiations to electronics (R2E) project [141]. In particular, to validate the fault detection technique, FRF compressor measurements were performed for a fixed rotational speed, low helium mass flow levels and at different process temperatures: at ambient temperature (∼300 K) and at 30 K. The compressors rotational speeds during the measurements were: 15 Hz for compressor stage 1, 20 Hz for compressor stage 2, 30 Hz for compressor stage 3 and 40 Hz for compressor stage 4.

4.2.3 Fault detection results

For the fault detection experimental validation, all the four compressors in the IHI-Linde cold box were tested. First, the system identification was carried out on records acquired on the same considered compressors in unfaulty conditions. Therefore, following the steps described in Section 2.2.4, the reference noise power P_{REF} and its variance $\mathrm{Var}\{P_{REF}\}$ has been calculated. Based on engineers experience, the probability of false alarm P_{fa} has been set equal to 0.01. Then, the thresholds τ have been calculated for each compressor. They have been reported in the second column of Table 4.3.

Furthermore, the noise power has been evaluated on new records, acquired during maintenance tests. As an example, in Fig. 4.8 the reference record (*reference*), the identified track (*model*) and the record from the system under test (*SUT*) are shown for compressor stage 2. It can be observed that the parametric model allows the main features of the reference record to be captured. A small variation, probably due to the specific conditions when the record was acquired, is filtered by the model. Finally, the differences $P_{SUT} - P_{REF}$ for the four compressors have been assessed, and they

Table 4.3: Values of the threshold τ and of the distance $P_{SUT} - P_{REF}$ for each of the compressors under test.

Compressor	τ	$P_{SUT} - P_{REF}$
CCS1	0.025	44.5
CCS2	0.146	-0.24
CCS3	0.004	-0.01
CCS4	0.028	-0.04

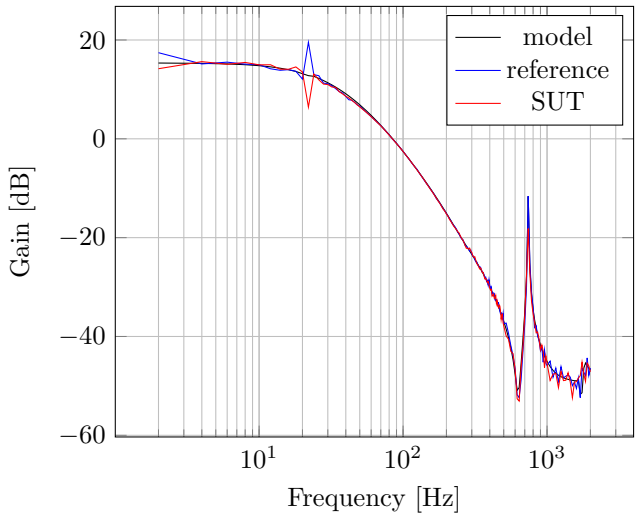

Figure 4.8: Cold compressor system 2 frequency response function in nominal conditions (*reference*), the identified records (*model*), and the frequency response of the system under test (*SUT*).

are reported in the third column of Table 4.3.

For the compressor stage 2, 3 and 4, no faults have been detected, because the difference $P_{SUT} - P_{REF}$ was under the corresponding τ. For cold compressor stage 1, instead, a faulty condition has been detected. In Fig. 4.9 and Fig. 4.10 the nominal condition identification and the comparison between the identified record (black) and the SUT record (red), for compressor stage 1, are respectively shown.

Thanks to the proposed technique, a fault was then detected, and the faulty compressor was sent back to manufacturer. The IHI-Linde company confirmed that some minor mechanical problems were found.

4.2.4 Early-stage fault isolation results

In the following, the results of the two steps of early-stage fault isolation are reported for the above case study for the cold compressor system stage 1, with the twofold aims of identifying the most influencing model parameters and evaluating their influence on the estimated noise power.

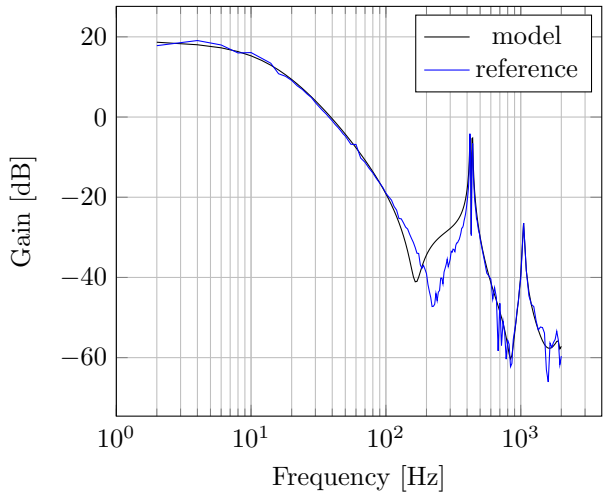

(a) Reference record (*reference*) and identified record (*model*).

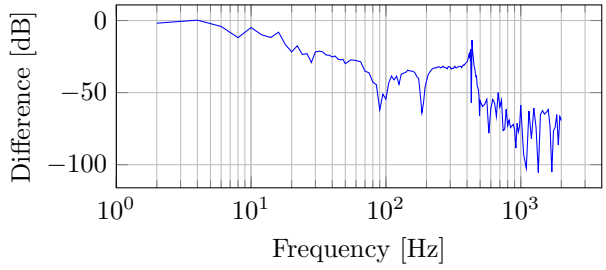

(b) Difference between reference record and identified record.

Figure 4.9: Identification of the nominal condition for compressor 1.

Parameters ranking

At this aim, a standard Taguchi plan L27 [119] has been adopted for its capability of investigating combinatorial spaces generated by up to thirteen 3-levels discrete parameters. In particular, for the *i-th* parameter, the nominal value p_i plus/minus the variability range has been chosen. This variability range has been defined based on the real system knowledge and it has been set equal to 1 % for the real poles and the damping ratio, while for the frequencies, it has been chosen equal to 20 Hz. In Tab. 4.4 the ANOVA results are reported.

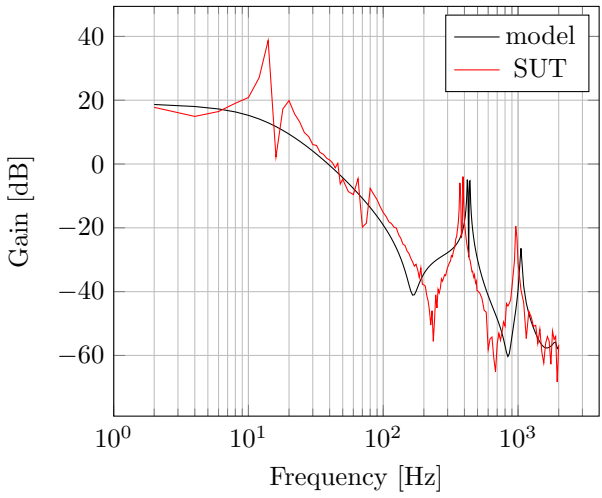

(a) Identified record (*model*) and record acquired during maintenance test (*SUT*).

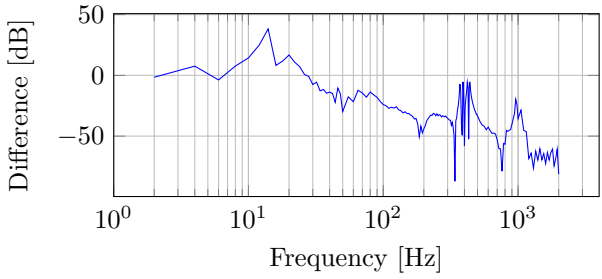

(b) Difference between the identified record and the record acquired during maintenance test.

Figure 4.10: Comparison between identified record (black) and SUT record (red) for compressor 1.

In particular, in the column **MS**, the contribution of the parameter to the overall variance, assessed as the ratio between the sum of the squares (column **SS**) and the related degrees of freedom (column **DF**), is reported. In the column F_i, the variance ratio related to the $i-th$ parameter is shown. In the last column, the so-called P-parameter, i.e. the probability, expressed in relative terms, that the variation associated with the considered parameter does not influence the corresponding performance factor, according to the traditional Fisher-Snedecor statistical test is indicated.

Table 4.4: ANOVA results.

	SS	**DF**	**MS**	F_i	**P**
$Pole1$	0.06794	2	0.03397	134.14	0.0000
$Pole2$	0.00011	2	0.00005	0.21	0.8156
$Pole3$	0.00010	2	0.00005	0.20	0.8259
$Pole4$	0.00010	2	0.00005	0.20	0.8204
$DR1$	0.00044	2	0.00022	0.88	0.4633
$DR2$	0.00054	2	0.00027	1.07	0.4019
$DR3$	0.00053	2	0.00027	1.05	0.4055
$Freq1$	0.01845	2	0.00922	36.42	0.0004
$Freq2$	0.02849	2	0.01425	56.26	0.0001
$Freq3$	0.08587	2	0.04293	169.54	0.0000
Error	0.00152	6	0.00025		

Parameter identification

Once the most influencing parameters were identified by ANOVA, the BBd method, described in 2.2.5, was performed, in order to evaluate the effects of the variation of the most influencing parameters on the figure of merit. For this test, a variability range was defined and 27 runs were performed. In particular, on the basis of historical knowledge of the actual system, the following variability ranges were chosen: 2 % for the real pole (p_1), and 10 Hz for the frequencies (p_2, p_3 and p_4). The coefficients $\beta_0, \beta_l, \beta_{ll}$, and β_{lm} in Tab. 4.5 were then identified with the least-square method. Finally, the second-order model (2.36), representing the behavior of the noise power versus the variation of the model parameters, was fitted.

In Fig. 4.11a, a plot of the fitted surface is reported when the parameter p_2 and p_3 have been varied and the parameter p_1 and p_4 have been left to their nominal values. The intersection with the plane corresponding to the threshold value for that compressor is shown, too. It is easy to see that the locus of the intersecting points is the ellipse shown in Fig. 4.11b and it is possible to note that the points of the plane inside the ellipse are below the threshold, while those outside the ellipse are above the threshold. In this way, the subspace of the model parameters that cause a faulty condition is identified.

By analyzing the deviations of the model parameters for the compressor that has been identified as faulty, displacements of -53 Hz and -51 Hz have been found for parameters p_2 and p_3, respectively. in Fig. 4.11b, the corresponding point on the

Table 4.5: Coefficient vector identification

Coefficient	Value
$\hat{\beta}_0$	0.000×10^{-5}
$\hat{\beta}_1$	-1.467×10^{-4}
$\hat{\beta}_2$	3.141×10^{-4}
$\hat{\beta}_3$	-3.292×10^{-4}
$\hat{\beta}_4$	8.915×10^{-5}
$\hat{\beta}_{11}$	7.343×10^{-3}
$\hat{\beta}_{22}$	1.435×10^{-4}
$\hat{\beta}_{33}$	1.013×10^{-4}
$\hat{\beta}_{44}$	3.594×10^{-5}
$\hat{\beta}_{12}$	2.235×10^{-4}
$\hat{\beta}_{13}$	2.165×10^{-4}
$\hat{\beta}_{14}$	1.282×10^{-4}
$\hat{\beta}_{23}$	1.473×10^{-4}
$\hat{\beta}_{24}$	5.119×10^{-5}
$\hat{\beta}_{34}$	6.015×10^{-5}

plane reporting p_2 and p_3 has been marked. It can be seen that the marked point is far outside the ellipse.

4.3 FAULT DIAGNOSIS: Diagnostics of buildings

The dMGA was validated experimentally in an application in the framework of the project MONDIEVOB [142]. Several smart transducers are installed in an edifice for monitoring and diagnosing automatically the main building systems: anti-theft/anti-intrusion, air conditioning, electrical system, elevators and lifts, fire system, and so on. In the dMGA validation, the following edifice subsystems were monitored owing to their criticalities, by installing a network of smart transducers with the corresponding diagnostic units (Fig. 4.12): *(i)* Lift and elevators (LDU), by measuring all the parameters of the related electromechanical plant, as well as what is needed for the compliance with EU safety standards (e.g., UNI-EN 81.28) and directives; *(ii)* Heating plant (HDU), a classical primary-secondary pumping system, by monitoring the thermo-fluid-dynamic quantities such as water temperature and pressure in primary (generator to the storage tank) and secondary (storage tank to users) heating circuits

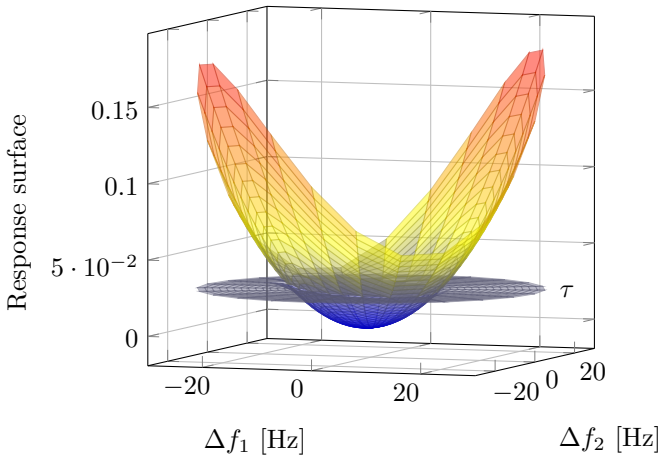

a) Response surface

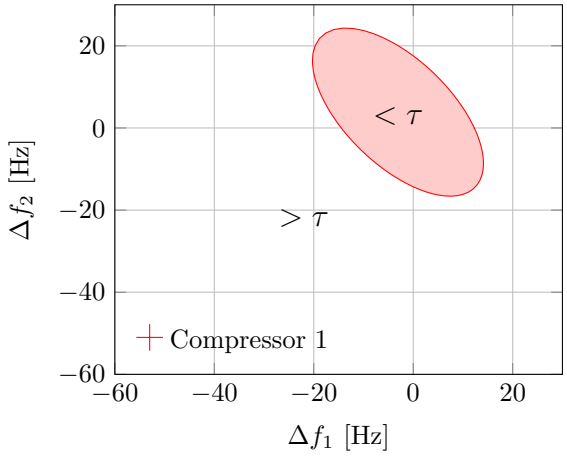

b) Intersection between the response surface and the plane at τ.

Figure 4.11: Response surface evaluated from the sensitivity analysis applied on compressor 1.

(HDU); *(iii)* Air handling (ADU), by monitoring the parameters (air temperature in the main circuit and in the heat recovery circuit) of the unit for air treatment, as well as of its humidifier and heat recovery circuit; *(iv)* Electrical/ Alarm (EDU), by monitoring all the quantities of electrical, fire, and anti-theft plants; and *(v)* (DDU) Domotic, by measuring room temperature, humidity, comfort parameters, and so on. Finally, the Remote Supervision Station (RSS) is a software-structured user interface,

for providing a remote view of all the monitored plants and the diagnostics output for data storage and maintenance.

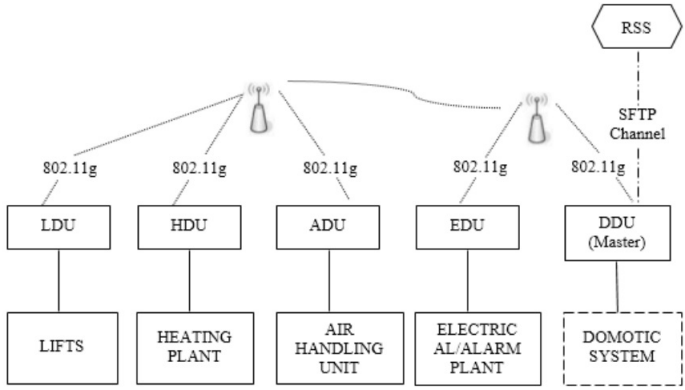

Figure 4.12: Architecture of distributed monitoring and multiple-fault diagnostics for buildings.

4.3.1 Diagnostics problem

For each of the above subsystems, main faults have to be diagnosed on the basis of the corresponding anomalies. As an example (Table 4.6): (i) for the electrical system (A1-13, F1-4), a power electrical black out, or a fault to the line transformer have to be diagnosed by starting from the detection of problems on the voltage lines R,S,T vs the neutral N, or a too low power factor $\cos(\varphi)$; (ii) for the heating plant (A14- 21, F5-14), a failure to the hydraulic separator between primary and secondary circuits is to be diagnosed when an overheating is detected on the primary circuit in summer position; (iii) for the air treatment (A22-25, F15-24), a faulty humidistat or a drift in the water temperature sensor of the secondary circuit have to be explained by starting by an apparent overheating in the heat recovery air.

4.3.2 Experimental setup

Each smart transducer includes (Fig. 4.13): (i) analog and digital output and interfaces for sensors data acquisition; (ii) ARM9/Unix OS-based single board computer platform (ARM 9, 200 MHz, 32 MB RAM); (iii) wireless peripheral for local network interface; and (iii) modem interface for remote GPRS channel communication.

In Fig. 4.14, a particular of the smart transducer hosting the Domotic Diagnos-

Table 4.6: Anomalies and faults vectors (RST: electrical phases, N: neutral, cos(φ): power factor, ATU: air treatment unit).

Anomalies		**Faults**	
Current break phase RN	A1	Electrical power black out	F1
Current break phase SN	A2	Electrical overload	F2
Current break phase TN	A3	Transformer fault	F3
High voltage phase RN	A4	Loads with power factor correction	F4
High voltage phase SN	A5	Pressure reducer fault	F5
High voltage phase TN	A6	Water losses	F6
Low voltage phase RN	A7	Air in heating circuit	F7
Low voltage phase SN	A8	Heat pump fault	F8
Low voltage phase TN	A9	Hydraulic separator failure	F9
Low cos(φ) phase RN	A10	Fault valve secondary circuit	F10
Low cos(φ) phase SN	A11	Circulation pump primary circuit failure	F11
Low cos(φ) phase TN	A12	Fault pump secondary circuit	F12
High overbalance electrical loads	A13	Dirty filters primary circuit	F13
High pressure primary circuit	A14	Dirty filters secondary circuit	F14
Low pressure primary circuit	A15	Fault thermoregulation ATU	F15
High pressure secondary circuit	A16	Faulty valve ATU	F16
Low pressure secondary circuit	A17	No water supply	F17
High temp. primary circ. - summer	A18	Pump failure humidification	F18
Low temp. primary circ. - summer	A19	Battery failure humidification	F19
High temp. primary circ. - winter	A20	Faulty humidistat	F20
Low temp. primary circ. - winter	A21	Water temp. sensor fault primary circuit	F21
High temp. air fan ATU	A22	Water temp. sensor fault secondary circuit	F22
Low temp. air fan ATU	A23	Air temperature sensor fault recovery	F23
High temp. recovery air ATU	A24	Supply air temp. sensor fault	F24
Low temp. recovery air ATU	A25		

tic Unit, with a fan-coil actuator based on a transistor ULN2003A and a connector DB25 for temperature and solar radiation sensors, is highlighted. The dMGA was implemented in language C.

The following parameters configuration was used: number of machines: 3; number of runs: 10; population size: 24; migration rate: 10; crossover probability: 0.8; mutation probability: 0.2; maximum number of generations: 50; and maximum number of micro-generations: 5.

The centralized brute force algorithm was also in this case study implemented in MATLAB and executed on a pc.

In Fig. 4.15, the finite state automaton for the monitoring unit of lifts and elevators plants is illustrated.

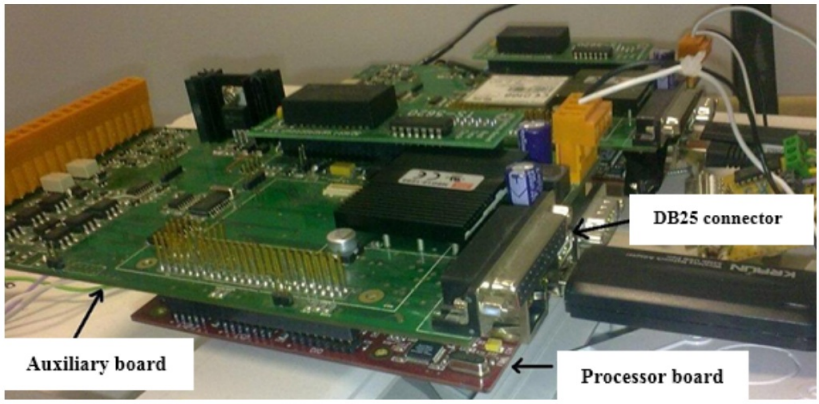

Figure 4.13: Smart transducer with embedded ARM9 TS7200, interface PC104 auxiliary board, and DB25 connector for analog and digital I/O.

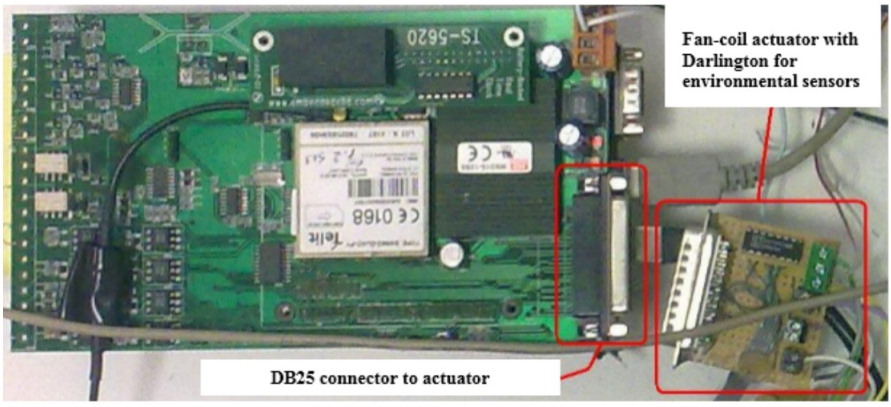

Figure 4.14: Domotic Diagnostic Unit with fan-coil actuator based on transistor ULN2003A with DB25 connector for temperature and solar radiation sensors.

4.3.3 Proof-of-principle scenario

Also in this case, the matrices for the relationships anomalies/faults C and a priori probabilities M of the possible faults P were based on engineering experience and requirements. In particular, most of the faults were focused on electrical, thermal, and air treatment units.

In Table 4.6, the considered 24 faults and the 25 anomalies are reported. The ma-

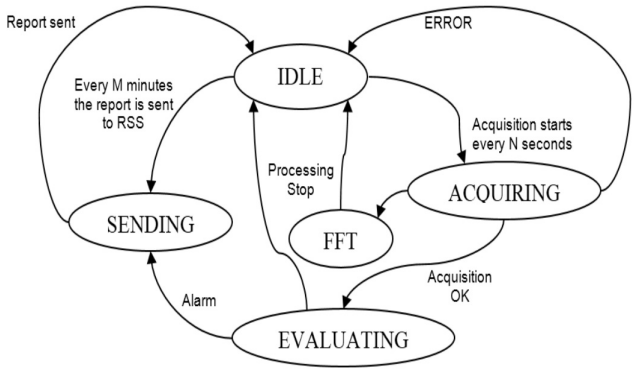

Figure 4.15: Finite state automaton for the monitoring unit of electrical, fire, and anti-theft systems.

trix C is large and sparse, with dimension $D \times M = 24 \times 25$, i.e., 2^{24} possible solutions of the diagnostic problem. An anomalous transition of a parameter triggers the start of the dMGA algorithm. The master unit (DDU) is responsible for vector transition detection, triggering the dMGA, and fault results encoding and transmission to RSS.

4.3.4 Experimental results

For a complete validation, single and multi-fault test cases were selected on different diagnostics problems of various dimensions.

As an example of single-fault diagnosis, in the test case 3 on the building electrical system (Table 4.7), the anomalies of an over-voltage line R vs neutral N with a simultaneous too low power factor $\cos(\varphi)$ (A4-A10) were detected.

The dMGA diagnosed as the solution with best likelihood (1.742×10^{-4}), a fault on the line transformer (F3), confirmed also by the brute force algorithm. As multi-fault example, in the Air Handling Unit, a too low pressure level on both the primary (A15) and the secondary circuits (A17), as well as a too low temperature level both on the fan (A23) and recovery (A25) air were detected.

The dMGA algorithm diagnosed as the fault with best likelihood (3.118×10^{-3}) the simultaneous presence of both water losses (F6) and thermoregulation (F15) faults in the Air Handling Unit. This diagnosis was also confirmed by the brute force algorithm.

As a matter of fact, for each test case, the brute force algorithm assessed the best solution in terms of fault vector and likelihood. The dMGA was run on (i) 1, 2, and

3 DUs in parallel with 100, 50, and 30 generations number; (ii) with 20 runs; and (iii) with population size 24, 15, 10, and 7. Table 4.7 reports the best dGMA result for the 5 test cases. The successful comparison between brute force and the dMGA likelihood values points out a satisfying validation.

In Table 4.8, for the above 5 test cases, the percentage of success on 20 runs is highlighted at varying the number of the involved diagnostic units, the number of generations, and the population size. The success condition is considered as the occurrence of the first run where the maximum likelihood value provided by the brute force algorithm is achieved. Results show how a decrease in the unit number up to 30 % (e.g., owing to failures of 2 smart transducers on 3) can be taken into account preventively in the design by selecting 100 generations and a population size of 24.

In fact, owing to this dMGA configuration, diagnostics success turns out to be robust to processors loss, because dMGA over-sizing counterbalances the loss. Obviously, in this extreme case, the parallelism is spent completely in redundancy, and thus only in reliability, without saving computing resources. Conversely, a decrease in the population size up to 30 % degrades drastically the performance, whatever the number of units and generations.

Table 4.7: Single and multi-fault test results.

Test	**Anomalies**	**Faults**		**Likelihood**
1	A1, A2, A3	Brute Force	F1	1.770×10^{-2}
		dMGA	F1	1.766×10^{-2}
2	A10	Brute Force	F4	2.600×10^{-3}
		dMGA	F4	2.572×10^{-3}
3	A4, A10	Brute Force	F3	1.742×10^{-4}
		dMGA	F3	1.742×10^{-4}
4	A15	Brute Force	F6	5.860×10^{-2}
		dMGA	F6	5.860×10^{-2}
5	A15, A17, A23, A25	Brute Force	F6,F15	3.100×10^{-3}
		dMGA	F6,F15	3.118×10^{-3}

Table 4.8: Success percentage at varying number of units, generations, and population size (lack of convergence in bold).

Test	No. of units	No. of generations	Population size			
			24	15	10	7
1	1	100	90	90	45	15
	2	50	95	80	60	10
	3	30	95	80	40	15
2	1	100	85	50	40	10
	2	50	85	45	40	40
	3	30	90	75	30	**10**
3	1	100	95	80	25	10
	2	50	95	80	40	25
	3	30	95	75	55	25
4	1	100	30	35	40	15
	2	50	55	45	25	15
	3	30	60	45	20	5
5	1	100	35	30	30	**20**
	2	50	35	20	15	5
	3	30	45	15	20	**5**

4.4 PREDICTIVE MAINTENANCE: Helium storage system

4.4.1 Application scenario

In this section, a case study on the liquid helium storage system installed at CERN is described and then some preliminary results of the proposed algorithm validation are presented. At this aim, the system configuration will be firstly described and then a comparison with GA will be reported, by analyzing the effectiveness (a measure of the quality solution within a given computational limit) and the efficiency (a measure of the amount of computing needed to achieve a satisfactory solution). The effectiveness is calculated as the best in run solutions, while the efficiency as the average of the iteration's number corresponding to the optimal solution.

Helium storage system

The cryogenic system of the Large Hadron Collider (LHC) under operation at CERN has a total helium inventory of 140 t [143] . Up to 50 t can be stored in gas storage tanks and the remaining inventory will be stored in a liquid helium storage system consisting of six 15 t of liquid helium tanks in 4 locations. In Fig. 4.16, the general

architecture of the system is shown.

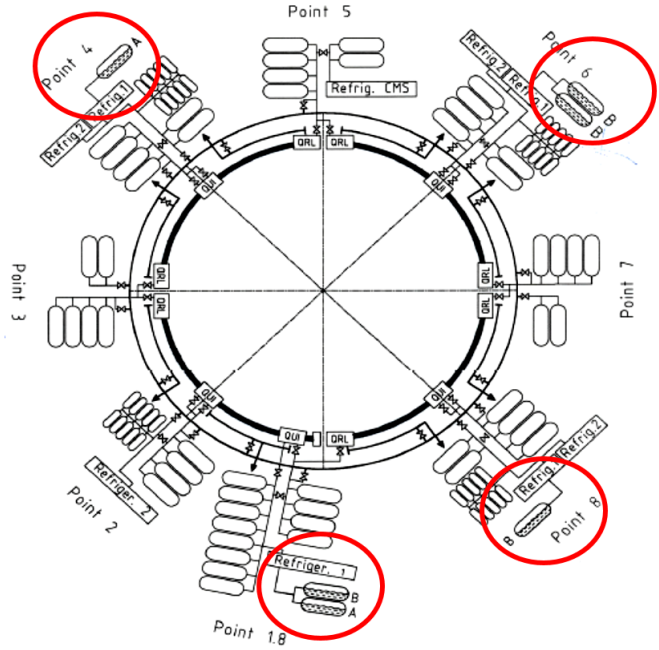

Figure 4.16: Helium storage system architecture.

The formulation proposed in this paper is aimed at solving the maintenance scheduling problem for only one of the LHC's installations, and for the sake of the simplicity, one its subset. A view of the 50 t liquid helium storage system located at LHC Point 1.8 is shown in Fig. 4.17. It is composed by (i) two tanks, combined cryogenic line, which allows the transfer from the LHC to the tanks (saturated liquid helium) and back (gaseous helium at 5 K), (ii) bayonets to transfer helium from or to mobile containers to adjust the inventory when required [143], and (iii) a liquid nitrogen tank with a semi-rigid line, used to refill the thermal shield. All the low temperature parts are vacuum insulated and thermally protected by multilayer insulation.

In Fig. 4.17, each tank is equipped with a level meter (L1-L2), a pressure sensor (P1-P2), and a temperature sensor, installed on helium outlet shield line (T1-T2); as for the helium, the nitrogen tank is equipped with a pressure sensor (P3) and a level meter (L3); the distribution box is equipped with a thermometer (T) installed in the helium gas return line and the low-pressure line is equipped with a flow-meter (F) to measure the heat consumption of the tanks. All these sensors allow to manage

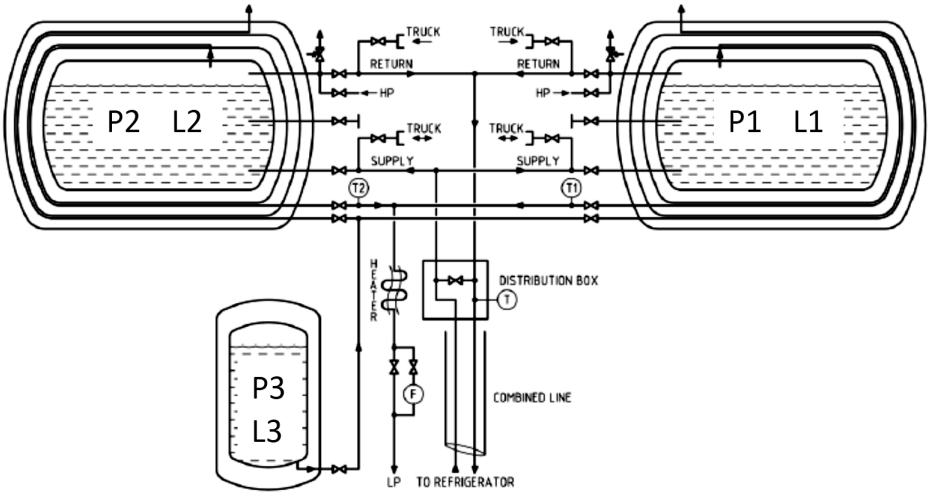

Figure 4.17: Simplified scheme of LHC's point 1.8 storage system.

the entire system and the measured values are sent to a dedicated PLC and a data acquisition system [144].

The preventive maintenance scheduling for such a system is carried out by classifying all the components in different categories and by defining a task list including the correspondent costs for all the possible actions to carry out. As an example, mechanical elements are separated from sensors and from electrical equipment; for each category, all the possible components are identified and a list of tasks (inspection, replacement, cleaning, etc.) is drafted. The maintenance time horizon for each task is defined by experience. As a consequence, the drawback of this solution is that no intelligent scheduling for preventive maintenance is performed.

In this paper, an alternative solution to the above mentioned problem is presented exploiting the GEO algorithm in order to find the optimal sequence for maintenance operations which minimizes the costs.

4.4.2 System configuration

The system used to test the proposed methodology is the liquid helium storage described in section 4.4.1 and in particular the one represented in Fig. 4.17. The components to be maintained can be classified in: control valves (CV), pneumatic valves (PV), analog sensors, digital sensors, hand valves (HV), safety valves (SV) and the breaking disks. For this case study, the GEO algorithm was implemented in Matlab

and it was compared to a standard GA. For both the algorithms, a maximum number of iterations was fixed to 10^4. In GEO algorithm, the parameter τ was set to 0.75. As for GA algorithm, the following parameters configuration was used: number of runs: 10; population size: equal to the product $M \cdot T$, crossover probability: 0.8; crossover mechanism: single point; mutation mechanism: uniform; and selection mechanism: roulette.

4.4.3 Experimental results

Scheduling problems with increasing dimensions were used to perform preliminary experimental tests in order to validate the effectiveness and the efficiency. In Table 4.9, the problem settings are presented.

Table 4.9: Problem Settings

Test n.	M	T	N	Solution length (n. of bits)
1	14	14	2	196
2	14	14	5	196
3	14	14	7	196
4	21	21	3	441
5	21	21	5	441
6	21	21	11	441
7	35	35	5	1225
8	35	35	10	1225
9	35	35	19	1225
10	42	42	5	1764
11	42	42	15	1764
12	42	42	23	1764

The proposed GEO works only on 1 individual and performs a number of evaluations as the solution length; therefore, in order to be compared with the GA, the population size of the last algorithm has been set equal to the solution length: 196 for the tests n.1-3, 441 for the test n.4-6, 1225 for the test n.7-9, and 1764 for the test n.10-12.

For a fixed number of maximum iterations, the GEO algorithm at each run converges to the same best solution cost with the same number of iterations. The same behaviour for the best solution in standard GA was observed, while a variable iterations number was noticed.

In Tabs. 4.10 and 4.11, preliminary experimental results were reported.
For a small number of resources (N) in the time horizon (T), some problems to fulfil

Table 4.10: Best solution cost

Test n.	GEO Solution	GA Solution
1	784.964	–
2	805.404	–
3	802.484	784.964
4	1683.000	–
5	1716.701	–
6	1723.202	1650.240
7	4585.503	–
8	4597.201	–
9	4606.703	4326.38
10	6442.101	–
11	6561.102	–
12	6568.604	6137.244

the constraints in GA algorithm were reported. The smallest value of N to avoid this problem, tests n.3, n.6, n.9, and n.12, is reported, but in these cases, the effectiveness (Table 4.10) achieved for GEO and GA are very different, and, in particular, GA performs better than GEO. N represents the number of available resources and, in practical applications, this value is always very limited. In Table 4.11, the efficiency expressed in terms of number of iterations is presented, and the difference between the GEO algorithm and GA is shown.

Table 4.11: Number of iterations

Test n.	GEO Iter.	GA Iter. Mean	GA St. Dev.
1	3146	–	–
2	3483	–	–
3	9286	111.44	13.06
4	2963	–	–
5	8960	–	–
6	9218	234.33	19.55
7	4077	–	–
8	9763	–	–
9	9440	642.01	25.34
10	3995	–	–
11	9182	–	–
12	9517	960.50	31.78

Conclusions

In this Thesis, advanced methods and techniques have been proposed for monitoring, fault diagnostics, and predictive maintenance of cryogenic processes and systems.

In particular, the design and the proof-of-principle demonstration of a transducer based on a virtual flow-meter for helium monitoring in cryogenic systems for particle accelerators were presented. Two alternative different models (Samson and Sereg-Schlumberger) for virtual helium flow-meter design were used. During the experimental validation for the gaseous state on the test station for superconducting magnets in the SM18 test facilities at CERN, the experiments proved that the modified Samson and Sereg-Schlumberger models (after the calibration) can be used in laminar and transient regime. The model validation under turbulent conditions is an interesting point for future investigations. Both the models underestimated the measured mass flow, the RMSE values for Samson and Sereg-Sclumberger methods are respectively 7.50 % and 7.00 %, but specifically the Sereg-Schlumberger performed better than the Samson model. From these results, the Sereg-Schlumberger method will be preferred in future applications at CERN for gaseous helium.

The next step is to analyze more comprehensively the dependence on all parameters, as well as the metrological performance by means of an uncertainty analysis. A further future step will be to optimize both the methods specifically for the liquid state. As a matter of fact, higher attention to the physical properties of helium is to be paid because, along the saturation condition, a working region where the helium shows both gas and liquid properties simultaneously is to be considered.

Furthermore, the uncertainty analysis of the proposed virtual flow-meter-based transducer for monitoring helium flow in cryogenic conditions has been presented. The analysis exploits an uncertainty model of the transducer, considering its main uncertainty sources, setting parameter, and operating conditions. The uncertainty model is based also on a state-of-the-art model of the helium, and an ad-hoc developed model at finite-elements of the valve. Both these models were validated at

CERN in the laboratory SM18 under actual cryogenic conditions. The uncertainty has been analysed by combining statistical experiment design and ANOVA to verify both the metrological design of the prototype and to point out the most influencing uncertainty sources for further improvements. This analysis has been carried out both on an overall metrological performance and on its main components of uncertainty and deterministic error.

From a computational point of view, 270 trials, each lasting 30 minutes (5.6 days), were conducted, over the 5145 trials (107 days) required in a Monte-Carlo approach. The results highlight the quality of the metrological design of the current transducer release. Better metrological performance can be achieved if the deterministic error, arising from the uncertainty associated with the flow-meter model, temperature measurement, valve opening, and helium properties, is corrected. Conversely, the uncertainty of pressure measurement turns out to be too low, thus allowing the use of cheap sensors in the next release of the virtual flow-meter-based transducer.

A fault detection and early-stage isolation technique for cold compressors based on AMB has been also proposed. The method is intended to be used during maintenance tests, where the main influence parameters, such as temperature and rotational speed of the compressor, can be controlled, thus the uncertainty of the unfaulty condition is assumed to be dominated by the noise overlapped on few FRF records. In these conditions, the technique is applicable even in the case few records of measurements, acquired in a non-faulty condition, are available.

The proposed method has been applied to 4 compressors installed in the LHC and, thanks to it, a fault has been identified in one of such compressors. A sensitivity analysis of the proposed method has been also presented on the measurement taken from one of the compressors, in order to show the influence of the model parameters on the values of the figure of merit used to detect the fault. In this way, further information about the most probable parameter determining the fault can be extracted.

Further work goes in the direction of the extension of the proposed method in order to complete the fault isolation, by providing a complete determination of the kind, size and location of the fault (isolation), thus arriving to a comprehensive fault diagnosis.

A diagnostic procedure, based on a distributed microgenetic algorithm for transducer networks monitoring complex systems, has also been proposed. The well-settled evolutionary approach of centralized multiple-faults diagnostics is extended to dis-

tributed networks.

The approach was tested at first in simulation at CERN for LHC cryogenic system diagnostics developments and then on the field for the main systems of a building. Experiments proved the following main innovations of the distributed microgenetic algorithm: (i) improved efficiency by parallel process, shorter time execution, and higher population diversity; (ii) increased reliability and easy network re-modulation in case of a faulty node; and (iii) higher effectiveness and efficiency of the dMGA in comparison with brute force algorithm.

Finally, in the present thesis, a standard Generalized Extremal Optimization (GEO) based algorithm for a predictive maintenance scheduling problem on large experimental systems has been presented. In these preliminary tests on a set of high dimension scheduling problems, an independence from N value for the GEO algorithm, compared to a standard GA, was highlighted. In particular, the proposed GEO is successful for each N value. However, by increasing N, the standard GA reaches better solutions with a lower number of iterations. Based on these results, a comparison with an evolutionary algorithm having the same feature, or new tests, implementing modified GEO algorithms, should be carried out in the future research.

References

[1] M.Girone V.Inglese M.Pezzetti F.Piccinelli L.Serio P.Arpaia, E.Blanco. Proof-of-principle demonstration of a virtual flow meter-based transducer for gaseous helium monitoring in particle accelerator cryogenics. *Journal of Review of Scientific Instruments*, 86, 2015.

[2] P Arpaia, M Girone, A Liccardo, M Pezzetti, and F Piccinelli. Metrological analysis of a virtual flowmeter-based transducer for cryogenic helium. *Review of Scientific Instruments*, 86(12):125001, 2015.

[3] M. Girone M. Pezzetti P. Arpaia, L. De Vito. Early-stage fault isolation based on frequency response fitted by small-size samples for cryogenic cold compressors with active magnetic bearings. *Review of Scientific Instruments (submitted)*, 2015.

[4] P Arpaia, P Cimmino, M Girone, G La Commara, D Maisto, C Manna, and M Pezzetti. Decentralized diagnostics based on a distributed micro-genetic algorithm for transducer networks monitoring large experimental systems. *Review of Scientific Instruments*, 85(9):095103, 2014.

[5] Pasquale Arpaia, Domenico Maisto, and Carlo Manna. A generalized extremal optimization-inspired algorithm for predictive maintenance scheduling problems. In *IJCCI (ICEC)*, pages 70–76, 2010.

[6] R. P. Reed K. D. Timmerhaus. Cryogenic engineering. *Int. Cryogenics Monograph Series*, 2007.

[7] Shao-Yun Kalia, Susheel Fu. Cryogenic processing: State of the art, advantages and applications. *Book section of Polymers at Cryogenic Temperatures*, 2013.

[8] P. Muoz-Escalona A. Shokrani, V. Dhokia and S. T. Newman. State-of-the-art cryogenic machining and processing. *Int. Journal of Computer. Integrated Manufacturing*, 26(7):616–648, 2013.

[9] F.Vandoni U.Wagner Ph. Lebrun, L.Tavian. *Cryogenics For Particle Accelerators And Detectors*. CERN LHC/2002-11, 2002.

[10] Joern Ploennigs, Ammar Ahmed, Burkhard Hensel, Paul Stack, and Karsten Menzel. Virtual sensors for estimation of energy consumption and thermal comfort in buildings with underfloor heating. *Advanced Engineering Informatics*, 25(4):688–698, 2011.

[11] Haorong Li, Daihong Yu, and James E Braun. A review of virtual sensing technology and application in building systems. *HVAC&R Research*, 17(5):619–645, 2011.

[12] Wei Zhang, Nenggen Ding, Guizhen Yu, and Wei Zhou. Virtual sensors design in vehicle sideslip angle and velocity of the centre of gravity estimation. In *Electronic Measurement & Instruments, 2009. ICEMI'09. 9th International Conference on*, pages 3–652. IEEE, 2009.

[13] Domenico Capriglione, Consolatina Liguori, Vincenzo Paciello, Antonio Pietrosanto, and Paolo Sommella. A software sensor for motorcycle suspension stroke. In *Sensors*, pages 445–448. Springer, 2015.

[14] Byung Mun Lee and Un Gu Kang. Virtual sensor for diabetes meter in u-health service. *Diabetes*, 18(21.9):1–0, 2014.

[15] Nikhil Raveendranathan, Stefano Galzarano, Vitali Loseu, Raffaele Gravina, Roberta Giannantonio, Marco Sgroi, Roozbeh Jafari, and Giancarlo Fortino. From modeling to implementation of virtual sensors in body sensor networks. *Sensors Journal, IEEE*, 12(3):583–593, 2012.

[16] Venkat Venkatasubramanian, Raghunathan Rengaswamy, Surya N Kavuri, and Kewen Yin. A review of process fault detection and diagnosis: Part iii: Process history based methods. *Computers & chemical engineering*, 27(3):327–346, 2003.

[17] Luigi Fortuna, Salvatore Graziani, Alessandro Rizzo, and Maria Gabriella Xibilia. *Soft sensors for monitoring and control of industrial processes*. Springer, 2007.

[18] Petr Kadlec, Bogdan Gabrys, and Sibylle Strandt. Data-driven soft sensors in the process industry. *Computers & Chemical Engineering*, 33(4):795–814, 2009.

[19] Bruno OS Teixeira, Walace S Castro, Alex F Teixeira, and Luis A Aguirre. Data-driven soft sensor of downhole pressure for a gas-lift oil well. *Control Engineering Practice*, 22:34–43, 2014.

[20] David Wang, Jun Liu, and Rajagopalan Srinivasan. Data-driven soft sensor approach for quality prediction in a refining process. *Industrial Informatics, IEEE Transactions on*, 6(1):11–17, 2010.

[21] Sanem Kabadayi, Adam Pridgen, and Christine Julien. Virtual sensors: Abstracting data from physical sensors. In *Proceedings of the 2006 International Symposium on on World of Wireless, Mobile and Multimedia Networks*, pages 587–592. IEEE Computer Society, 2006.

[22] Enrique Blanco. Superfluid helium cooling loop on string2. *LHC Internal Note, CERN*, 2003.

[23] Samson AG Mess- und Regeltechnik. http://www.samson.de, 2015.

[24] Schlumberger Inc. http://www.slb.com/, 2015.

[25] George EP Box and Norman R Draper. *Empirical model-building and response surfaces.* John Wiley & Sons, 1987.

[26] George EP Box, J Stuart Hunter, and William G Hunter. Statistics for experimenters: design, innovation, and discovery. *AMC*, 10:12, 2005.

[27] Philippe Lebrun. Cryogenics for the large hadron collider. *Applied Superconductivity, IEEE Transactions on*, 10(1):1500–1506, 2000.

[28] Pasquale Arpaia, Carlo Manna, Carmine Romanucci, and Antonio Zanesco. Cultural evolutionary design of adaptive wavelet filters based on lifting scheme for micro-instruments. *Measurement*, 43(7):966–974, 2010.

[29] BinQiang Chen, ZhouSuo Zhang, YanYang Zi, ZhiBo Yang, and ZhengJia He. A pseudo wavelet system-based vibration signature extracting method for rotating machinery fault detection. *Science China Technological Sciences*, 56(5):1294–1306, 2013.

[30] Ruqiang Yan, Robert X Gao, and Xuefeng Chen. Wavelets for fault diagnosis of rotary machines: A review with applications. *Signal Processing*, 96:1–15, 2014.

[31] Meng Hee Lim and MS Leong. Detection of early faults in rotating machinery based on wavelet analysis. *Advances in Mechanical Engineering*, 2013.

[32] G. Meltzer and Nguyen Phong Dien. Fault diagnosis in gears operating under non-stationary rotational speed using polar wavelet amplitude maps. *Mechanical Systems and Signal Processing*, 18(5):985–992, 2004.

[33] Changqing Shen, Dong Wang, Fanrang Kong, and W Tse Peter. Fault diagnosis of rotating machinery based on the statistical parameters of wavelet packet paving and a generic support vector regressive classifier. *Measurement*, 46(4):1551–1564, 2013.

[34] F Al-Badour, M Sunar, and L Cheded. Vibration analysis of rotating machinery using time–frequency analysis and wavelet techniques. *Mechanical Systems and Signal Processing*, 25(6):2083–2101, 2011.

[35] Jinglong Chen, Ming J Zuo, Yanyang Zi, and Zhengjia He. Construction of customized redundant multiwavelet via increasing multiplicity for fault detection of rotating machinery. *Mechanical Systems and Signal Processing*, 42(1):206–224, 2014.

[36] Konstantinos C. Gryllias and Ioannis A. Antoniadis. A support vector machine approach based on physical model training for rolling element bearing fault detection in industrial environments. *Engineering Applications of Artificial Intelligence*, 25(2):326–344, 2012.

[37] P Konar and P Chattopadhyay. Bearing fault detection of induction motor using wavelet and support vector machines (svms). *Applied Soft Computing*, 11(6):4203–4211, 2011.

[38] Nassim Laouti, Nida Sheibat-Othman, and Sami Othman. Support vector machines for fault detection in wind turbines. In *Proceedings of IFAC world congress*, volume 2, pages 7067–7072, 2011.

[39] R Gouws and G van Schoor. Real-time displacement analysis and correction system for vibration forces on rotor of rotational active magnetic bearing system. *World Journal of Engineering*, 8(4):381–394, 2011.

[40] Kazushige Obara, Keiji Kasahara, Sadaki Hori, and Yoshimitsu Okada. A densely distributed high-sensitivity seismograph network in japan: Hi-net by

national research institute for earth science and disasterprevention. *Review of scientific instruments*, 76(2):021301, 2005.

[41] RT Shelton, JH Kamperschroer, LJ Lagin, JR Nelson, and DW OBrien. Target diagnostic control system implementation for the national ignition facility (invited) a). *Review of Scientific Instruments*, 81(10):10E101, 2010.

[42] Yannick Pencolé and Marie-Odile Cordier. A formal framework for the decentralised diagnosis of large scale discrete event systems and its application to telecommunication networks. *Artificial Intelligence*, 164(1):121–170, 2005.

[43] Arun Subbiah and Douglas M Blough. Distributed diagnosis in dynamic fault environments. *Parallel and Distributed Systems, IEEE Transactions on*, 15(5):453–467, 2004.

[44] James Kurien, Xenofon Koutsoukos, and Feng Zhao. Distributed diagnosis of networked hybrid systems. In *AAAI Spring Symposium on Information Refinement and Revision for Decision Making: Modeling for Diagnostics, Prognostics, and Prediction*, pages 37–44, 2002.

[45] Anmol Sheth, Carl Hartung, and Richard Han. A decentralized fault diagnosis system for wireless sensor networks. In *Mobile Adhoc and Sensor Systems Conference, 2005. IEEE International Conference on*, pages 3–pp. IEEE, 2005.

[46] Gregory Provan. A model-based diagnosis framework for distributed systems. Technical report, DTIC Document, 2002.

[47] Nico Roos, Annette ten Teije, and Cees Witteveen. Multi-agent diagnosis with semantically distributed knowledge. In *Proceedings of the 15th Belgium-Dutch Conference on Artificial Intelligence (BNAIC-2003)*, pages 259–266, 2003.

[48] Yun Peng and James A Reggia. *Abductive inference models for diagnostic problem-solving*. Springer Science & Business Media, 2012.

[49] Marco Dorigo and Luca Maria Gambardella. Ant colony system: a cooperative learning approach to the traveling salesman problem. *Evolutionary Computation, IEEE Transactions on*, 1(1):53–66, 1997.

[50] J. Kennedy and R. Eberhart. Particle swarm optimization. In *IEEE International Conference on Neural Networks IV*, page 19421948, 1995.

[51] David E Goldberg. Sizing populations for serial and parallel genetic algorithms. In *Proceedings of the 3rd International Conference on on Evolutionary Computation*, pages 119–124, 1996.

[52] V Rao Vemuri, Danny Barash, and Ann E Orel. A genetic search in frequency space for stabilizing atoms by high-intensity laser fields. *CIT. Journal of computing and information technology*, 8(2):103–113, 2000.

[53] David L Carroll. Genetic algorithms and optimizing chemical oxygen-iodine lasers. *Developments in theoretical and applied mechanics*, 18(3):411–424, 1996.

[54] William Gropp, Ewing Lusk, Anthony Skjellum, and Rajeev Thahur. Using mpi 2nd edition: Portable parallel programming with message passing interface, 1999.

[55] Dominick Rehage, Udo B Carl, and Andreas Vahl. Redundancy management of fault tolerant aircraft system architectures–reliability synthesis and analysis of degraded system states. *Aerospace science and technology*, 9(4):337–347, 2005.

[56] Rommert Dekker, Ralph E Wildeman, and Frank A van der Duyn Schouten. A review of multi-component maintenance models with economic dependence. *Mathematical Methods of Operations Research*, 45(3):411–435, 1997.

[57] Robin P Nicolai and Rommert Dekker. *Optimal maintenance of multi-component systems: a review*. Springer, 2008.

[58] Scott Kirkpatrick, C Daniel Gelatt, Mario P Vecchi, et al. Optimization by simulated annealing. *science*, 220(4598):671–680, 1983.

[59] David E Golberg. Genetic algorithms in search, optimization, and machine learning. *Addion wesley*, 1989, 1989.

[60] James Kennedy. Particle swarm optimization. In *Encyclopedia of Machine Learning*, pages 760–766. Springer, 2010.

[61] Marco Dorigo, Vittorio Maniezzo, and Alberto Colorni. Ant system: optimization by a colony of cooperating agents. *Systems, Man, and Cybernetics, Part B: Cybernetics, IEEE Transactions on*, 26(1):29–41, 1996.

[62] Fabiano Luis De Sousa and Fernando Manuel Ramos. Function optimization using extremal dynamics. In *4th International Conference on Inverse Problems in Engineering Rio de Janeiro, Brazil*. Citeseer, 2002.

[63] Stefan Boettcher and Allon G Percus. Optimization with extremal dynamics. *complexity*, 8(2):57–62, 2002.

[64] FABIANO LUIS DE SOUSA, Valeri V Vlassov, and Fernando Manuel Ramos. Heat pipe design through generalized extremal optimization. *Heat Transfer Engineering*, 25(7):34–45, 2004.

[65] FL De Sousa, FJCP Soeiro, AJ Silva Neto, and FM Ramos. Application of the generalized extremal optimization algorithm to an inverse radiative transfer problem. *Inverse Problems in Science and Engineering*, 15(7):699–714, 2007.

[66] Piotr Switalski and Franciszek Seredynski. An effective multiprocessor scheduling with use of geo metaheuristic. *International Journal of Foundations of Computer Science*, 23(02):465–481, 2012.

[67] Dong Xie, Zhe Luo, and Fan Yu. The computing of the optimal power consumption for semi-track air-cushion vehicle using hybrid generalized extremal optimization. *Applied Mathematical Modelling*, 33(6):2831–2844, 2009.

[68] Peng Guo, Wenming Cheng, and Yi Wang. A modified generalized extremal optimization algorithm for the quay crane scheduling problem with interference constraints. *Engineering Optimization*, 46(10):1411–1429, 2014.

[69] Guglielmo Ventura and Lara Risegari. Practical, industrial and space applications of cryogenics. *In The Art of Cryogenics*, 26(7):299–306, 2008.

[70] Y. Jung-J. Kim H. Park M. Seo, S. Jeong. Improved pressurevolumetemperature method for estimation of cryogenic liquid volume. *Journal of Cryogenics*, 52(46):290–295, 2012.

[71] Neil T. Van Dresar. Pvt gauging with liquid nitrogen. *Journal of Cryogenics*, 46(23):118–125, 2006.

[72] P. Skyba M. Medeova, V. Pavlk. Simple continuous level meter for cryogenic liquids. *Journal of Cryogenics*, 38(3):289–291, 1998.

[73] K. Asamoto-Y. Nishimura S. Abe T. Numazawa K. Matsumoto, M. Sobue. Capacitive level meter for liquid hydrogen. *Journal of Cryogenics*, 51(2):114–115, 2011.

[74] E. Shibamura-M. Yamashita T. Yoshimura R. Sawada, J. Kikuchi. Capacitive level meter for liquid rare gases. *Journal of Cryogenics*, 43(8):449–450, 2003.

[75] T.Zhang S. W.Van Sciver D.Celik, D. K.Hilton. Helium ii level measurement techniques. *Journal of Cryogenics*, 41(5-6):355–366, 2001.

[76] R. Chen B. Zhang Y. Lin T. Chen, Q. Wang and K. P. Chen. Distributed liquid level sensors using self-heated optical fibers for cryogenic liquid management. *Journal of Applied Optics*, 51(26):6282–6289, 2012.

[77] R. P. Swinehart K. P. Chen T. Chen, M. Maklad. Self-heated optical fiber sensor array for cryogenic fluid level sensing. *IEEE Journal of Sensors*, 11(4):1051–1052, 2011.

[78] D. C. Malocha B. H. Fisher. Cryogenic liquid sensing using saw devices. *Proc. of IEEE Int. Frequency Control Symposium joint with the 21st European Frequency and Time Forum*, pages 505–510, 2007.

[79] K. Ohira. Development of density and mass flow rate measurement technologies for slush hydrogen. *Journal of Cryogenics*, 44(1):59–68, 2004.

[80] A. Fuchs G. Holler, D. Hrach. Application of a combined capacitive flow velocity and density sensor for the measurement of liquid hydrogen mass flow. *Proc. of IEEE Instrumentation and Measurement Technology Conference, I2MTC*, pages 1444–1448, 2009.

[81] S. Grohmann. A new method for flow measurement in cryogenic systems. *Journal of Cryogenics*, 60:9–18, 2014.

[82] R. J. Donnelly C. J. Swanson, S. C. Hall. Measurement devices for cryogenic turbulence research. *Journal of Cryogenics*, 41(5-6):341–345, 2001.

[83] A. Rivetti L. Serio T. De Jonge, T. Patten. Development of a mass flowmeter based on the coriolis acceleration for liquid, supercritical and superfluid helium. *Proc. of 19th Int. Conference on Cryogenic Engineering*, pages 647–650, 2002.

[84] F. M. Caimi S. W. Van Sciver D. M. Kocak, J. F. Justak. A cryogenic mass flow sensor. *Proc. of AIP Conference*, 823(1):281, 2006.

[85] M. Bol P. Roy L. Manceron L. Lago, C. Herbeaux. A rugged, high precision capacitance diaphragm low pressure gauge for cryogenic use. *Journal of Review of Scientific Instruments*, 85(1), 2014.

[86] J. A. Nissen J. A. Lipa Z. K. Geng, D. R. Swanson. A high-resolution superconducting pressure control system for use at low temperatures. *Proc. of Int. Forum-2000 in Space Technology and Applications*, 504(1):674–678, 2000.

[87] F. Pobell. Miscellaneous cryogenic devices and design aids. *Book section of Matter and methods at low temperature*, pages 353–390, 2007.

[88] H. Fillinger S. I. Schlachter M. Süer R. Ramalingam, D. Boguhn. Study of robust thin film pt-1000 temperature sensors for cryogenic process control applications. *Tran. of the Cryogenic Engineering Conference-CEC*, 1573(1):126–131, 2014.

[89] H. Schön M. Süer S. Grohmann, T. Bode. Precise temperature measurement at 30 k in the katrin source cryostat. *Journal of Cryogenics*, 51(8):438–445, 2011.

[90] T. Ishida T. Yotsuya, Y. Kakehi. Thin film temperature sensor for cryogenic region with small magnetoresistance. *Journal of Cryogenics*, 51(9):546–549, 2011.

[91] F. Pavese et al. V. F. Mitin, P. C. McDonald. Ge-on-gaas film resistance thermometers for cryogenic application. *Journal of Cryogenics*, 47(9-10):474–482, 2007.

[92] J. Rymaszewski M. Lebioda. Dynamic properties of cryogenic temperature sensors. *Przeglad Elektrotechniczny*, 91(2):225–227, 2015.

[93] M. A. Caponero F. Felli C. Lupi L. Ippoliti M. Ciotti, V. Nardelli. An optical system for cryogenic temperature measurements. *Journal of Smart Materials and Structures*, 16(5), 2007.

[94] M. Ogata K. Mizuno K. Nagashima S. Okumura Y. Terada H. Yamada, Y. Tanaka. Measurement and improvement of characteristics using optical fiber temperature sensors at cryogenic temperatures. *Journal of Physica C: Superconductivity*, 471(21-22):1570–1575, 2011.

[95] H. Wang Z.-S. Guo, J. Feng. *Journal of Cryogenics*, (10).

[96] B. Lee Y. W. Lee. High resolution cryogenic optical fiber sensor system using erbium-doped fiber. *Proc. of the 4th Pacific Rim Conference on Lasers and Electro-Optics CLEO/Pacific*, 1:1, 2001.

[97] A. Muzammil A. N. Riza. Cryogenic temperature measurement using silicon carbide-based wireless optical sensor. *IEE Photonics Technology Letters*, 18(24):2599–2601, 2006.

[98] V. G. Shabratov Y. P. Filippov. Measurement of helium temperatures by tvo-sensors under magnetic fields. *Journal of Cryogenics*, 42(2):127–131, 2002.

[99] L. Kuzmin. Ultra-sensitive cryogenic thermometer based on an array of the sin tunnel junctions. *Journal of Physica C: Superconductivity*, 468(3):142–146, 2008.

[100] S. S. Courts. A standardized cernox cryogenic temperature sensor for aerospace applications. *Journal of Cryogenics*, 64:248–254, 2014.

[101] L. Bottura J. C. Perez F. Borgnolutti B. Jenninger P. Ryan V. Datskov, G. Kirby. Precise thermometry for next generation lhc superconducting magnet prototypes. *IEEE Tran. on Applied Superconductivity*, 24(3):1–5, 2014.

[102] K. Flachbart J. Tejada L. Kopera E. Kovov K. Temst Y. Bruynseraede I. Vvra, J. Bydovsk. Fe/cr sensor for the millikelvin temperature range. *Journal of Sensors and Actuators A: Physical*, 91(1-2):177–179, 2001.

[103] D. Forest G. Hofmann M. Granata D. Heinert G. Cagnoli J. Degallaix, J. Komma. Measurement of the optical absorption of bulk silicon at cryogenic temperature and the implication for the einstein telescope. *Journal of Classical and Quantum Gravity*, 31(18), 2014.

[104] S. W. Van Sciver D. K. Hilton. Gravitational capillary viscometer for low-temperature liquids. *Journal of Review of scientific instruments*, 78(3), 2007.

[105] M. Penza P. Aversa M. Giordano A. Guemes A. Cusano M. Consales, A. Consales. Optical fiber probes for cryogenic detection of hydrogen. *Journal of Optical Fiber Sensors, Optical Society of America*, 2006.

[106] R. Ramalingam J. Li, H. Neumann. Design, fabrication, and testing of fiber bragg grating sensors for cryogenic long-range displacement measurement. *Journal of Cryogenics*, 68:36–43, 2015.

[107] L. Bottura G. Montenero P. Arpaia, A. Ballarino. A cryogenic sensing element for measurement current transformers. *Journal of Instrumentation*, 9(3), 2014.

[108] D. Grimaldi G. Hofmann J. Komma F. Lamonaca A. Nastro R. Nawrodt F. Picariello G. Polimeni M. Riccio C. Schwarz K. Yamamoto D. Chen, P. Daponte. Mechanical loss characterization at cryogenic temperature of a tungsten wire: An automated measurement system. *Proc. of IEEE Metrology for Aerospace (MetroAeroSpace) Workshop*, pages 479–483, 2014.

[109] Frank M White. Fluid mechanics. 4th.

[110] John Aurie Dean. Lange's handbook of chemistry. 1985.

[111] Spirax-Sarco Learning Centre. *Steam Engingeering Learning Modules: Module 6.5, Control Valve Characteristics*. Gloucestershire, United Kingdom, 2005.

[112] IEC 60534-2-1:2011. *Industrial-process control valves - Part 2-1: Flow capacity - Sizing equations for fluid flow under installed conditions.*

[113] IEC 60534-2-4:2009. *Industrial-process control valves - Part 2-4: Flow capacity - Inherent flow characteristics and rangeability.*

[114] P Arpaia, E Blanco, M Girone, V Inglese, M Pezzetti, F Piccinelli, and L Serio. Proof-of-principle demonstration of a virtual flow meter-based transducer for gaseous helium monitoring in particle accelerator cryogenics. *Review of Scientific Instruments*, 86(7):075004, 2015.

[115] Genichi Taguchi, Subir Chowdhury, and Yuin Wu. *Taguchi's quality engineering handbook. "Part III : Quality Loss Function."*. Wiley, 2005.

[116] WEKA. http://www.weka-ag.ch, 2015.

[117] Florian R Menter. Zonal two equation k-turbulence models for aerodynamic flows. *AIAA paper*, 2906:1993, 1993.

[118] P. Verboven, P. Guillaume, B. Cauberghe, S. Vanlanduit, and E. Parloo. A comparison of frequency-domain transfer function model estimator formulations for structural dynamics modelling. *Journal of sound and vibration*, 279(3):775–798, 2005.

[119] Raymond H Myers, Douglas C Montgomery, and Christine M Anderson-Cook. *Response surface methodology: process and product optimization using designed experiments*, volume 705. John Wiley & Sons, 2009.

[120] Douglas C Montgomery and George C Runger. *Applied statistics and probability for engineers*. John Wiley & Sons, 2010.

[121] Enrique Alba and Marco Tomassini. Parallelism and evolutionary algorithms. *Evolutionary Computation, IEEE Transactions on*, 6(5):443–462, 2002.

[122] Heinz Muhlenbein. Evolution in time and space-the parallel genetic algorithm. In *Foundations of genetic algorithms*. Citeseer, 1991.

[123] Rami Debouk, Stéphane Lafortune, and Demosthenis Teneketzis. Coordinated decentralized protocols for failure diagnosis of discrete event systems. *Discrete Event Dynamic Systems*, 10(1-2):33–86, 2000.

[124] Luca Console, Claudia Picardi, and Daniele Theseider Dupré. A framework for decentralized qualitative model-based diagnosis. In *IJCAI*, pages 286–291, 2007.

[125] Mitsuo Gen and Runwei Cheng. *Genetic algorithms and engineering optimization*, volume 7. John Wiley & Sons, 2000.

[126] Rudolph Frederick Stapelberg. *Handbook of reliability, availability, maintainability and safety in engineering design.* Springer Science & Business Media, 2009.

[127] E Odlund. *Virtual instrumentation: Introduction of virtual flow meters in the LHC cryogenics control system.* PhD thesis, MSc thesis, Linköpings Universitet, 2007.

[128] Norman R Draper and Harry Smith. *Applied regression analysis.* John Wiley & Sons, 2014.

[129] WIKA. http://www.wika.co.uk, 2015.

[130] Andrea Saltelli, Marco Ratto, Terry Andres, Francesca Campolongo, Jessica Cariboni, Debora Gatelli, Michaela Saisana, and Stefano Tarantola. *Global sensitivity analysis: the primer.* John Wiley & Sons, 2008.

[131] S Claudet, F Millet, B Jäger, L Tavian, P Gayet, U Wagner, and P Roussel. Specification of eight 2400 w@ 1.8 k refrigeration units for the lhc. Technical report, 2000.

[132] Rolf Isermann. *Fault-diagnosis applications: model-based condition monitoring: actuators, drives, machinery, plants, sensors, and fault-tolerant systems.* Springer Science & Business Media, 2011.

[133] Agoston E Eiben and James E Smith. *Introduction to evolutionary computing.* Springer Science & Business Media, 2003.

[134] V Benda, M Granier, Ph Lebrun, G Novellini, V Sergo, L Tavian, and B Vullierme. Cryogenic benches for superfluid helium testing of full-scale prototype superconducting magnetsfor the cern lhc project. *Cryogenics*, 34:733–736, 1994.

[135] A Calzas, S Knoops, L Serio, D Chanat, and M Sanmartí. Large cryogenic infrastructure for lhc superconducting magnet and cryogenic component tests. In *AIP Conf. Proc.*, volume 710, pages 217–224, 2004.

[136] O Pirotte, V Inglese, V Benda, B Vullierme, O Brunner, T Koettig, and P Maesen. Upgrade of the cryogenic cern rf test facility. Technical report, 2014.

[137] Brooks Instrument. http://http://www.brooksinstrument.com, 2015.

[138] Cryodata INC. *Users Guide To HEPAK.* Louisville, Colorado. Version 3.4. 1999.

[139] Hannes Bleuler, Matthew Cole, Patrick Keogh, R Larsonneur, E Maslen, Y Okada, G Schweitzer, A Traxler, Gerhard Schweitzer, Eric H Maslen, et al. *Magnetic bearings: theory, design, and application to rotating machinery.* Springer Science & Business Media, 2009.

[140] MECOS AG. http://www.mecos.com/de/, 2015.

[141] Markus Brugger, F Butin, J Christiansen, F Faccio, P Farthouat, A Ferrari, D Kramer, R Losito, AL Perrot, M Pojer, et al. Review of critical radiation areas for lhc electronics and mitigation actions. radiation monitoring and first results. In *Proc. LHC performance workshop, Chamonix*, page 170, 2010.

[142] Project MONDIEVOB. Buildings remote monitoring and evolutionary diagnostics.

[143] V Benda, JF Bel, M Fathallah, T Goiffon, C Parente, E Perez-Duenas, Ph Perret, O Pirotte, L Serio, and B Vullierme. The liquid helium storage system for the large hadron collider. Technical report, 2011.

[144] Philippe Gayet and Renaud Barillere. Unicos a framework to build industry like control systems: Principles and methodology. In *International Conference on Accelerator and Large Experimental Physics Control Systems, Genève, Suisse*, 2005.

List of Figures

List of Tables